Using Satellite imagery to investigate the spatiotemporal development of trough blowouts in coastal foredunes

MSc Thesis

Utrecht University

Niels van Kuik

July 2020

Supervisors:

Gerben Ruessink

Job de Vries

Christian Schwarz

ABSTRACT

Vegetation growth on coastal foredunes, enhanced by traditional coastal dune management, made the foredunes an artificial wall between the aeolian dynamics of the beach and the hinterland. Naturally, depressions in the foredunes, so-called trough blowouts, may connect the hinterland to the beach, beneficial for ecological diversity. To bring back aeolian dynamics in the hinterland, construction of artificial trough blowouts in foredunes is considered. However, currently there is a scarcity of decadal scale observations of the development of natural foredune blowouts. As the interest in using artificial foredune blowouts as coastal dune management strategy is growing, there is need for better understanding of the long-term development of these trough blowouts.

In this thesis, an artificial blowout system (Zuid-Kennemerland) and two natural blowout systems (Padre Island, Haurvig) were monitored using Landsat and Sentinel-2 spectral imagery. Linear Spectral Unmixing was applied on a single image basis. Endmembers were obtained from the image itself by finding representative pixels for sand, water and dune vegetation. The trough blowouts, defined as bare sand areas, were then successfully separated from the surroundings using the unmixed images. Comparison with high resolution drone imagery showed that the satellite images estimated the area of the blowout on average within 2% of their actual size.

Initiation of foredune blowouts was observed 1) after two consecutive severe storm surges and, 2) as a gradual multi-annual process probably triggered by local vegetation dying off on the foredune. For the Zuid-Kennemerland and Haurvig study sites, the aerial extent of blowouts increased during winters and decreased during summers. Growth in the winter corresponded to the relatively high energetic wind conditions at Zuid-Kennemerland, with interannual variations related to wind energy. Despite seasonal variations, it was observed that blowouts remained their size given an open connection to the beach is present. Gradual landward expansion of the depositional lobe was found for the blowouts with relatively small entrance widths compared to the full blowout length. The blowouts at Haurvig showed multi-annual growth related to occasional storm surges. Blowout closure was found at Padre Island when the blowouts transgressed further inland losing their open connection to the beach. Future research should include auxiliary data capable of measuring volumes, such LiDAR or Ground Penetrating Radar. This enables to verify whether seasonal and instantaneous increases of the sand area was a continuous expansion of the dune elevation or just a local reorganization of the sand and vegetation coverage.

Keywords:

*Trough Blowouts, Foredune notches***,** *Coastal dunes, Google Earth Engine, Sentinel-2, Landsat, Linear Spectral Unmixing, Image Endmembers*

Contents

List of Figures and Tables

1 Introduction

1.1 Reintroducing natural dynamics in foredunes

Coastal dunes can range from a single dune ridge of only a few meters in elevation (Franklin et al., 2018) till large scale dune field of several kilometers land inward and up to 100 meters in elevation (Pye and Tsoar, 2008; Vimpere et al., 2019), and make up about one-third of the world's coastal region (Luijendijk et al., 2018). The formation of coastal dune's is controlled by the sediment supply to the beach, where vegetation colonization has led to deposition and eventually development into dunes (Hesp, 2012). Variation in the vegetation cover resulting from wind- or wave erosion, climatic changes or an oversupply of sediment leads to natural, dynamic coastal dunes. In these natural systems, the beach can be connected with the back dunes through gaps in the foredunes, so-called blowouts. Blowouts may allow for the input of calcareous sand into the backdunes (Gares and Nordstrom, 1995; Hesp, 2002). In that case, the acidity of the soil decreases, which is beneficial to the endemic plant species. Also, climax vegetation, such as shrubs and tall grasses, can become buried completely by the sand input, which may open possibilities for pioneer species to establish (Schwarz et al., 2019). Thus, natural dune systems are characterized by their continuous spatiotemporal variation in extent, vegetation cover and sand supply.

The shore-parallel most seaward vegetated dune is called the foredune (Hesp, 2002). This is the first dune sufficiently developed to protect against flooding of the hinterland (Arens et al., 2013). Therefore, traditional coastal dune management has focused on reinforcement of the foredunes, making them more resilient against wave and wind erosion. As a consequence the foredunes stabilized, preventing the exchange between the beach and the backdunes (Arens et al., 2013). This stabilization of foredunes has occurred worldwide in for example North-Western Europe (Provoost et al., 2011; Arens et al., 2013; Pye and Blott, 2017), the USA (Nordstrom et al., 2000) and New Zealand (Gadgil, 2002).

The main method of stabilizing foredunes was increasing the growth of vegetation, thus decreasing their mobility (Gadgil, 2002). Vegetation growth was further enhanced by the increase in nitrogen deposition (Arens et al., 2013) and a reduction of the grazing by animals (Drees and Olff, 2001). This lack of disturbances resulted in a reduction of the biodiversity in the long-term, as climax vegetation was able to establish (Schwarz et al., 2019). Moreover, due to the vegetation holding sediment in the foredunes, the backdunes were no longer connected to their sediment source, which is required for them to grow and for example keep up with Sea Level Rise (SLR). Management measures, such as the nourishment of sand and planting of marram grass on the foredunes contributed to safety against flooding but did not increase the natural dynamics between the beach and the backdunes (Arens et al., 2013).

From the 1970s, awareness grew that dynamic and young natural coastal dune systems have a large ecological value (Arens et al., 2013). They comprise of a high biodiversity including endangered red-list species that cannot occur anywhere else. Nowadays, focus has shifted towards reintroducing ecological diversity in the hinterland by increasing natural dynamics in dunes systems (Mulder et al., 2011; Provoost et al., 2011). Coastal management changed to sustainable dune management, which target is that sand deflates from the seaward side and deposits on the landward side (Arens et al., 2013; Mulder et al., 2011). This creates more harsh circumstances in the back dunes removing climax vegetation, enabling a great diversity of pioneer species to establish (Arens et al., 2005; Provoost et al., 2011). An example of sustainable dune management is the recent excavation of five notches in the foredune in Zuid-

Kennemerland, the Netherlands. They have been constructed in the winter of 2012-2013 to facilitate aeolian sand transport from the beach into the backdunes (Arens et al., 2013) and mimic the natural process of foredune blowouts (Ruessink et al., 2018). This dune managing project focuses on stimulating aeolian dynamics, to reverse the present-day decline in dune biodiversity and restore the input of sand to the back dunes allowing them to keep up with SLR.

1.2 Relevance of this research

Blowout development might follow a cyclic course, where incipient blowouts form in small depressions in the foredune and widen due to accelerating wind-speeds. Finally, the widening of the structure decreases the accelerating 'jet-effect' of wind inside the foredune blowout, initiating the closure of the blowout (Gares and Nordstrom, 1995). More recent literature emphasizes on the importance of vegetation in this cyclic behavior of foredune blowouts. It suggested initiation is linked to abiotic processes, while closure is related to biotic processes (Schwarz et al., 2019). The cyclic model was based on multiple blowouts which were in different stages at the time of analysis, while the link to abiotic and biotic process was based on a summarization of previous literature. Nowadays, these blowouts are artificially created and used for example in the Netherlands to reintroduce coastal dynamics (Arens et al., 2013; Ruessink et al., 2018). Therefore, it is critical to understand how they develop and if artificial blowouts will stay open naturally, or human intervention is required to ensure the throughput of sand. However, due to scarcity of long-term research to foredune blowouts, it remains unclear what determines their lifetime.

This research gap is now possible to fill as an increased availability of medium-resolution satellite imagery has become freely available (Woodcock et al., 2008; ESA, 2019). These images allow for a worldwide, long-term analysis of the spatiotemporal development of multiple foredune blowout systems around the world. Although this massive amount of data is freely available, it is inaccessible for many users due to the technical and financial limitations of downloading and preprocessing this data locally. Cloud-computing solves this issue and enables easy worldwide applicability once an algorithm has been developed. Here, the cloud-computing free platform of the Google Earth Engine (GEE) has been used (Gorelick et al., 2017).

More specifically, this research will focus on the spatiotemporal development of the foredune blowouts on three study sites. To study the biotic characteristics of the blowout area, a vegetation index will serve as reference for the growth or decay of plants. Moreover, the framework developed allows studying a large variety of blowout sites. As high-resolution validation data was available for the man-made blowouts at the Kennemer Dunes (Ruessink et al., 2018), this site is used as a reference site. The development of blowouts will be monitored on a seasonal and decadal timescale. Consequently, this analysis aims to give insight into the development of multiple blowouts over various timescales. Thereby, it creates valuable knowledge on the capability of (man-made) blowouts to maintain a corridor for sediment input from the beach to the backdunes.

1.3 Brief methodology

Remote sensing offers a unique advantage of studying historical development of foredune blowouts. The spectral differences between the sandy extent of the blowout within vegetated foredunes allows the detection of the blowouts. Spectral sensors with adequate spatial resolution and free availability are the Landsat-4, -5, -7 and -8 and Sentinel-2 top-of-the-atmosphere products. Also, their temporal resolution allows for detecting of seasonal and decadal trends. The cloud-computing environment of the Google Earth Engine (GEE) permits application of the developed algorithm on three different blowout systems, namely the man-made blowouts in Zuid-Kennemerland, and natural blowout systems along the Danish and Texas (USA) coast.

Linear Spectral Unmixing (LSU) with remote sensing images (Sentinel-2 and Landsat 4,5,7,8) was utilized to determine the development of the sandy blowout area (consisting of deflation basin, erosional walls and depositional lobe) over time. This area is subtracted from the timeseries on a single image basis. Firstly, pre-processing of the imagery was applied and images with cloud cover were removed. A sequence of spatial sub-setting using the Otsu threshold on index bands for water (NDWI) and vegetation (NDVI) defined a first estimate of the spectral response of water, sand and vegetation within the Region of Interest (ROI). The spectral response of these three land cover types were used as endmembers for the LSU. LSU assumes that the spectral signal of a pixel is a linear combination of the surface the endmembers cover in that pixel (Keshava and Mustard, 2002). The fractional abundance image obtained from the LSU model was used to deduct a timeseries of blowout extents. Also, the vegetation index NDVI was used as a proxy for evaluating the growth of vegetation in and around the blowouts (Ormsby et al., 1987; Carlson and Ripley, 1997).

As a last step, the processed Sentinel-2 and Landsat scenes were tested for their accuracy. The blowout extent deducted from the satellite imagery was compared to higher spatial resolution airborne imagery. The verification dataset consisted of seven UAV images in the visible wavelength spectrum. The images were processed into georeferenced orthophotos with a resolution of 1 meter and served as ground-truth reference.

1.4 Research objectives and questions

Trough blowouts have historically been seen as a major destabilization factor of dunes, potentially increasing the risk of flooding. Nowadays, blowouts are seen vital in the process of dune building and increasing biodiversity (Ruessink et al., 2018), which remarks the interest in the development of natural blowouts. Blowouts develop over multiple decades and subsequently this is the timescale they should be studied to increase the knowledge for using trough blowouts as a management strategy (Gares and Nordstrom, 1995; Jewell et al., 2014). However, most trough blowout research has concentrated on short term development (3-15 years) (Gares and Nordstrom, 1995; Ruessink et al., 2018), while long term research is more scarce (Neal and Roberts, 2001; González-Villanueva et al., 2011; Jewell et al., 2017). Yet it can provide decisive information in the feasibility of man-made trough blowouts. Long term studies have been focusing on blowouts in different stages resulting in a blowout conceptual model (Gares and Nordstrom, 1995). Or they focussed on one or several blowouts in adjacency of each other while using local available data such as aerial imagery and Ground Penetrating Radar (González-Villanueva et al., 2011; Jewell et al., 2014).

Changes of seasonal wind, temperature and precipitation patterns are believed to strongly influence vegetation and blowout development (Byrne, 1997). Yet remote sensing imagery is only used with large spatial interval, i.e. a maximum of two images a year, eliminating the possibility to study seasonal patterns (Neal and Roberts, 2001; Jewell et al., 2017; Ruessink et al., 2018). Or on a short temporal scale, usually to deduct wind flow patterns (Hesp and Hyde, 1996; Smyth et al., 2014; Hesp and Smyth, 2016). No studies have been performed on trough blowouts on several locations around the globe with a similar dataset and methodology to deduce a framework of trough blowout development. Moreover, remote sensing imagery has not been applied to investigate the seasonal variability of trough blowouts over multiple decades. This can provide decisive information in the feasibility of the construction of man-made trough blowouts as part of a management strategy.

The free availability of remote sensing images since 1984 of the Landsat 5 mission (Woodcock et al., 2008), accompanied with major developments of (cloud) computation power (Yang, Yu et al., 2017; Gorelick et al., 2017), enabled the study of these systems on a large temporal scale. Therefore, the main objective of this study is to monitor the development of selected blowouts worldwide by means of freely available remote sensing imagery via the GEE. Trough blowouts will be tracked for multiple decades using the available spectral imagery. The first objective of this research is to create a toolbox inside the GEE enabling the analysis of blowout extent and vegetation cover over time. In combination with the ensured continued space missions of the ESA and USGS, this algorithm can then be used for years to track blowouts and dune dynamics on a temporal high resolution over decades. The algorithm is validated using high-resolution UAV imagery. The investigated evolution of the foredune trough blowouts is compared to additional remote sensing data (a vegetation index as proxy for the abundance of vegetation) and local data from wind, weather and water level measuring stations where available. Consequently, the main questions and subquestions of this MSc thesis are:

How does the spatial extent of foredune trough blowouts evolve over time and which temporal characteristics can be described?

1) How can foredune trough blowouts on medium-resolution (10-30m) satellite imagery be monitored over time?
2) At what accuracy can the extent of blowouts be examined from medium-resolution satellite imagery in comparison to high resolution (1m) aerial images for Zuid-Kennemerland?
3) What driving factors play a role for the temporal variations of the blowout extent?

1.5 Reading guide

The second chapter gives an overview of existing blowouts and the role vegetation plays in foredune dynamics. An overview of blowouts dynamic in foredunes around the globe is provided, guided by earlier developed conceptual models of natural foredune trough blowouts. Also, the shift from classic coastal dune management to the present integrated coastal management strategy is introduced. The third chapter will describe the satellite imagery details and the land cover features present in the region of interest. Also, the difficulties of detecting bare sand areas in coastal foredunes is pointed out. The fifth chapter firstly describes the three study sites. The core section of chapter five comprises the methodology including the proposed algorithm to track trough blowouts in foredunes over time from satellite imagery. Also, the explanation of the accuracy assessment using the UAV-imagery is given. The sixth chapter describes the results and the seventh chapter examines the outcomes in the discussion section. The last chapter presents the conclusions and proposes recommendations for the construction of man-made trough blowouts.

2 Foredune blowouts

This chapter discusses the current knowledge foredune blowouts. Firstly, a general description of the types of blowouts and the location they have been observed is given. The second section suggests a conceptual model of the initiation, development and closure of foredune trough blowouts, the type of blowout further discussed in this research. Thirdly, a discussion on the role of vegetation within these blowouts is given. Lastly, the link between the natural phenomenon of foredune blowouts to current management strategies is presented.

2.1 Types and dimensions of blowouts

A blowout is a depression or hollow in unconsolidated sand dunes, initiated by a large range of factors disturbing the existing vegetation cover. The blowout is a wind induced erosional feature, characterized by steep walls on the side ending in an adjoining depositional section. Blowouts are common features in coastal foredunes around the world (Hesp et al., 2017), but are also found in the backdunes (Anderson and Walker, 2006; Jungerius, 1984). Moreover, they have been found along large lakes (Dech et al., 2005), in inland dunes of arid areas (Barchyn and Hugenholtz, 2013; Yang, Guan et al., 2017) and in colder environments (Käyhkö, 2007).

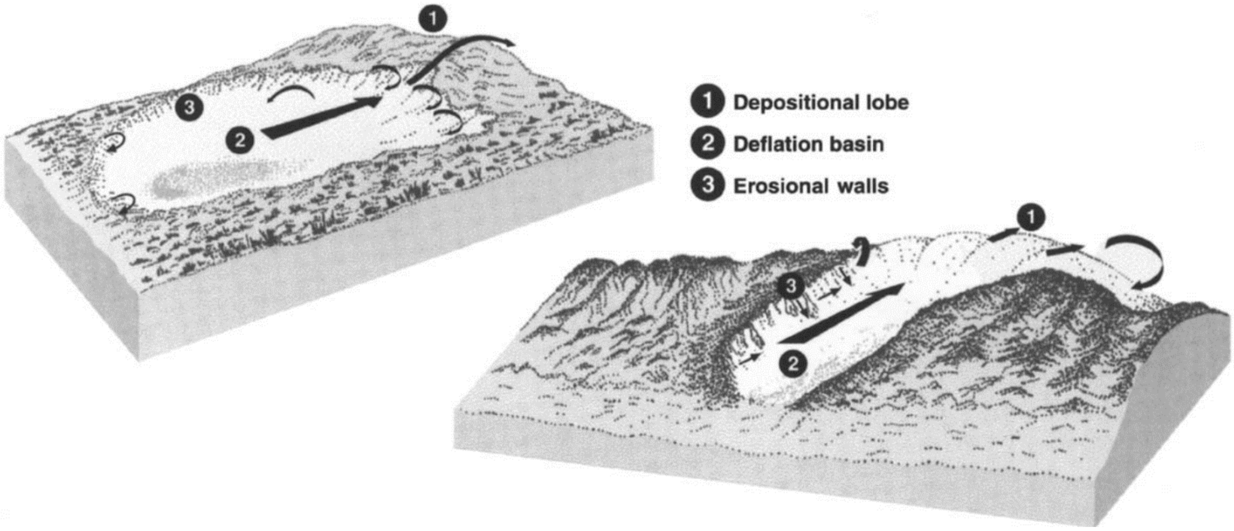

Figure 2-1: Schematic overview of a saucer (left) and trough (right) blowout. The black arrows represent typical wind flow patterns. Figure from Hesp (2002).

Blowouts are generally divided into two primary types; saucer- and trough blowouts (Figure 2-1; Hesp, 2002). A third type of blowout, a slot and cauldron blowout, has only recently been mentioned (Figure 2-2; Hesp et al., 2017) and is possibly the solution for the mixed trough-saucer shaped blowouts mentioned in earlier works (Mir-Gual et al., 2013; Smyth et al., 2013). Saucer blowouts are semi-circular or circular shaped features (Hesp, 2002). Trough blowouts are usually elongated in the dominant wind direction and generally confined between a vegetated dune ridge (Smyth and Hesp, 2016; Hesp et al., 2016). Slot and cauldron blowouts are trough shaped at the entrance from the beach and saucer shaped further inland (Hesp et al., 2017).

Figure 2-2; Slot and Cauldron Blowout found in Mason Bay (New Zealand) as indicated in Hesp et al. (2017).

The morphology of a trough and saucer blowout is schematically presented in Figure 2-1. Within both types of blowouts, the major morphological units recognized are typically the 1) depositional lobe, 2) deflation basin and, 3) erosional walls (Carter et al., 1990; Hesp and Hyde, 1996). The deflation basin is the depression in the foredune which erodes up to a more resistant base level such as the groundwater table, calcrete layer or aeolian non-erosional surface (e.g. pebble, shells) (Carter et al., 1990). On both sides of the deflation basin the blowout consists of erosional walls, which are generally steep and sparsely vegetated (Hesp, 2002) . The blowout widens by slumping of these walls due to oversteepening or removal of vegetation, after which the slumped sediment is transported downwind from the deflation basin into the depositional lobe. Usually, transport is land inward as onshore winds dominates, but the morphology is mirrored when offshore winds dominate (Hesp, 2002). In the blowout, the wind flow is turbulent and concentrated between the erosional walls. Beyond the confined walls the wind spreads laterally and thereby decelerates quickly (Hesp, 2002). Therefore, the sediment settles and creates the depositional lobe downwind (Carter et al., 1990; Byrne, 1997; Hesp, 2002).

The dimensions of blowouts can be measured in terms of 1) the length of the deflation basin and depositional lobe, 2) the width of the deflation basin, perpendicular to the blowout axis and, 3) the depth of the throat compared to the foredune crest (Schwarz et al., 2019). Trough blowouts differentiate clearly from saucer blowouts by their relative smaller deflation basin width compared to their depositional lobe length (Hesp, 2002). Previously research has indicated very small blowouts to be shorter than 20 meters (Hesp, 2002) and small blowouts to be 80 m long, 8m deep and 20-30m wide (Hesp, 1996). In Padre Island National Seashore, 8 out 18 blowouts are considered to be large with an average throat width of 60 m and length of 430 m (Jewell et al., 2014). Large blowouts are also found along the coast of Denmark with a width of 70 m and length of 450 m (Schwarz et al., 2019).

2.2 Conceptual model for trough blowout development

A process-based, cyclic model for the evolution of a trough blowout was divided into four different stages (Carter et al., 1990; Gares, 1992; Gares and Nordstrom, 1995). The cyclic evolution included the stages 1) notching, 2) incipient blowout, 3) full blowout and 4) closure (Gares and Nordstrom, 1995; Hesp, 2002). While this cyclic model focusses on the physical (i.e. abiotic) processes of wind flow which may either initiate and close the blowouts, more recently the interaction between physical (abiotic) and ecological (biotic) processes was added (Schwarz et al., 2019).

2.2.1 Notching

The initiation of a trough blowout in foredunes therefore depends on two major factors: 1) accelerating winds due to local topographic steering and concentration of wind energy and 2) locally exposed sand vulnerable to wind erosion due to the absence of vegetation. Predicting these processes is challenging because they are natural yet randomly initiating the formation of blowouts. Simultaneously, humans exert a growing pressure on coastal dune systems in an intended and unintended way. Therefore, destabilization of foredunes is usually localized (e.g. walking paths) and can trigger the formation of trough blowouts by both topographically accelerating winds and exposing unconsolidated sand to wind erosion. On the other hand, human contribute to stabilization of the foredunes mainly because of flood protection measures.

Local depressions in foredunes allow for the acceleration of winds as wind flow contracts. This results in further erosion of the foredune and the initiation of blowouts (Hesp, 1988). An example are the scarps in foredunes formed by discontinuous wave erosion, such as were found at Truc Vert Beach in France after a severe storm in 2014/2015 (Giles and McCann, 1997; De Winter et al., 2015). Washover of a foredune during storm surges can also result in local depressions, initiating the formation of a foredune blowout (Carter and Wilson, 1990; Hesp, 1996; Giles and McCann, 1997). Episodic events such as hurricanes increase the wave height and water level, inducing blowout initiation by wave erosion and overwash (Hesp, 2002; Jewell et al., 2017). On a regional scale, wind can be stirred and accelerated along confined curved beaches. For example, in Fiona beach (Australia) a curved beach is present between high cliffs. Along this confined shoreline, blowouts are found in the foredunes, while they are not found on nearby linear coastal stretches (Hesp and Hyde, 1996). As the climatic condition do not differ significantly, it was suggested that these curved beaches favor the initiation of blowouts by topographic wind acceleration.

On the elevated dune crests, vegetation growth may be hindered by wave erosion, animal grazing, soil degradation and climatic variations (Hesp, 2002). There, continuous longshore wave erosion also has the potential to remove vegetation. Eventually, this results in the dieback of more evolved shrubs on established foredunes (Hesp and Hyde, 1996), which is a commonly a process for initiating blowouts on steep-sloped reflective beaches with foredunes less than 10 m high (Short and Hesp, 1982). Animals have reported to be an important factor in the removal of vegetation and subsequent destabilization of coastal dunes that increases the potential for blowout formation (Ritchie, 1972; Martini, 1981; De Stoppelaire et al., 2004). Soil degradation on dune slopes have been reported for overland flow, formation of gullies after heavy rainfall and fires (Tinley, 1985; Jungerius and van der Meulen, 1989; Hesp, 2002). Decadal scale climatic variations such as droughts may destabilize dune fields by gradual vegetation impoverishment (Hesp, 2002; Barbosa and Dominguez, 2004; González-Villanueva et al., 2013).

Furthermore, relatively high aridity, salt spray and wind acceleration limit vegetation establishment on the foredunes and thereby increase the potential for blowout initiation (Arens et al., 1995).

Humans exert a growing pressure on coastal systems. Wide, high-energetic, dissipative beaches are popular recreational destinations, for example for surfing and holidays (e.g. Aquitanian Coast, France; Holland Coast, The Netherlands). Subsequently, the recreation of humans along beaches has led to the initiation of foredune blowouts, for example by trails through foredunes towards the beach (Pye, 1990; Bate and Ferguson, 1996; Yokota et al., 2018), 4-wheel-driving on the beach (Houser et al., 2013) and construction of houses near the shoreline (Nordstrom and McCluskey, 1985). Furthermore, intended destabilization of the foredunes as part of management strategies may lead to blowout formation.

2.2.2 Incipient blowout

Once vegetation is removed and a small erosional notch forms in the foredune, wind acceleration in the notch stimulates aeolian erosion. With a sufficiently high wind speed the deflation basin (throat) will grow downwind and facilitate the downward migration of the depositional lobe (Gares and Nordstrom, 1995). An incipient blowout can develop fast (2-5 years) to a full blowout if a well-developed hollow channelizes the wind in early stages, dense vegetation lacks and foredune width is small (Gares and Nordstrom, 1995). Observed erosion rates around 20 cm per month in the deflation basin of incipient blowouts are explained by local steering and acceleration of winds (Gares, 1992). Not much work refers to wind flow dynamics in incipient trough blowouts, as most wind flow studies are carried out on a relatively small temporal scale, during the well-developed ‘full blowout’ stage (Hesp and Hyde, 1996; Smyth et al., 2014; Hesp and Smyth, 2016). Accordingly, wind flow dynamics in trough blowouts will be discussed in the following full blowout stage.

2.2.3 Full blowout and flow dynamics

The major processes for a trough blowout to develop from stage 2 to stage 3 of the conceptual model includes erosion of the lateral walls and the deflation basin. This results in lengthening and widening of the blowout. The lateral walls erode due to undercutting and slumping (Hesp and Hyde, 1996; Ruessink et al., 2018). The deflation basin erodes up to the beach level or aeolian non-erosive layer, such as the groundwater table or a layer of shells or pebbles (Carter et al., 1990; Hesp, 2002; Barchyn and Hugenholtz, 2013). Simultaneously, the depositional lobe grows in length and height and the rim of the blowout shifts further downwind (Gares and Nordstrom, 1995; Arens et al., 2013; Schwarz et al., 2019).

The main cause that incipient blowouts grow into full blowouts relates to a positive feedback: the increment of the size of the blowout throat raises the potential of sediment transport by the increase wind acceleration (Gares and Nordstrom, 1995; Schwarz et al., 2019). When wind flow patterns inside a trough blowout are parallel to the blowout axis, five notable wind flow patterns occur: 1) acceleration in the throat, 2) flow expansion and deceleration, 3) acceleration over the lobe crest, 4) flow separation over the lobe crest and 5) vertices over the lateral walls (Figure 2-3; Hesp and Hyde, 1996).

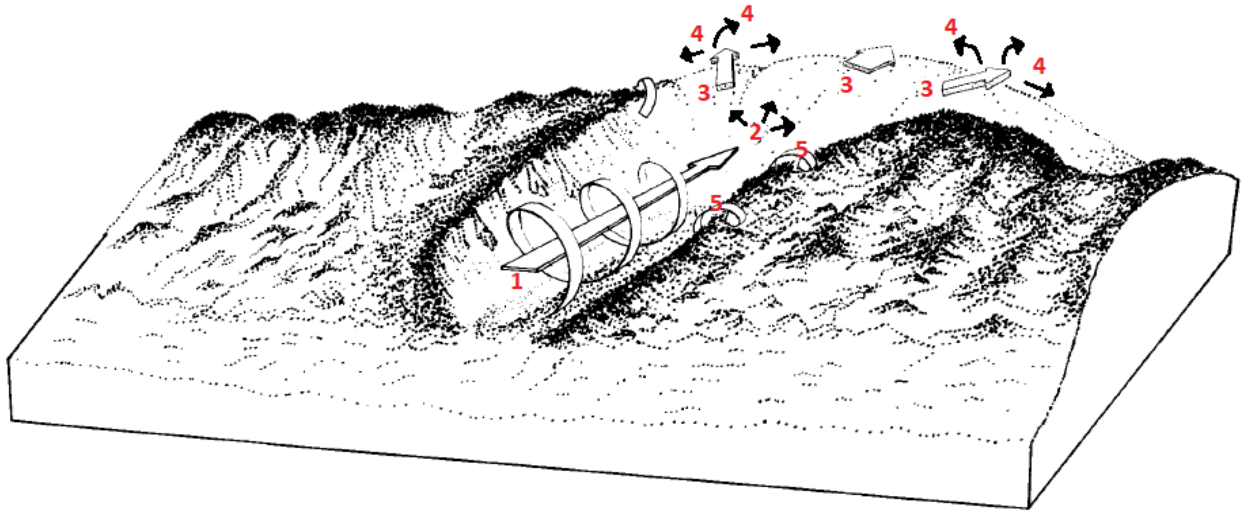

Figure 2-3; Wind flow patterns in a full blowout when wind flow is parallel to the blowout axis. The umbers refer to: 1) acceleration in the throat, 2) flow expansion and deceleration, 3) acceleration over the lobe crest, 4) flow separation over the lobe crest and 5) vertices over the lateral walls. See further description in the text. Adapted from Hesp and Hyde (1996).

(1) Inside the deflation basin and along the lateral walls, wind flow is parallel to the blowout axis (Hesp and Hyde, 1996). The steep lateral walls are important in the accelerating of the wind and the creation of jet flows, where at times turbulent corkscrew motions may occur (Carter et al., 1990). Inside the deflation basin, wind speeds may be accelerated by 20 to 30% compared to on the beach and therefore blowouts act as an effective corridor for sediment moving inland (Gares and Pease, 2015). (2) Where the deflation basin merges into the depositional lobe, the wind flow spreads and decelerates (Hesp and Hyde, 1996). (3) Towards the crest of the depositional lobe, the topography is rising. As such, wind flow compresses, accelerates and can form local jets (Hesp and Hyde, 1996). As long as wind is blowing in line with the deflation basin, maximum wind flow and sand transport is in the center (Hesp and Hyde, 1996). (4) At the leeside of the depositional lobe, flow separates and thus decelerates, causing the deposition of the blown material. Due to gravity, avalanching and grainfall sand is deposited on the leeside with the angle of repose. The finest grains may be transported by wind several meters further downwind (Hesp and Hyde, 1996). (5) At the top of the lateral walls, flow may leave the throat. These so-called roller vortices laterally transport sand outside the deflation basin (Hesp and Hyde, 1996). This process results in further deepening of the deflation basin and the formation of ridges along the lateral walls, called rim dunes (Carter et al., 1990).

On the other hands, it is common that wind is not flowing perfectly parallel to the mid-blowout axis, referred here as oblique winds. Oblique winds up to 50 degrees are stirred towards the blowout axis along uniform foredune ridges (Bennett and Hails, 1981; Hesp and Hyde, 1996). The jet-effect inside the throat then increases the sediment transport potential (Hesp and Hyde, 1996; Gares and Pease, 2015). Stronger deflections up to 100 degrees have been observed, though more oblique winds than 50 degrees reduce the net wind speed (Hesp and Pringle, 2001). Then, sediment is deposited in the throat and thus steering and re-alignment of the wind towards the blowout axis is presumably limited to about 50 degrees (Pease and Gares, 2013). Although wind directions up to 50 degrees are steered towards the blowout axis, the flow collides with the upwind erosional wall and the major flow bends to a curved or ‘s-shaped’ pattern

(Hesp and Hyde, 1996; Smyth and Hesp, 2016). Along the downwind lateral wall, a zone without acceleration develops and overall the acceleration inside the throat is less than with straight incoming winds (Gares and Pease, 2015). An increment of the incoming wind angle increases the turbulence but decreases the net wind speed of the flow inside the throat of the blowout (Hesp and Hyde, 1996; Gares and Pease, 2015).

A skewed orientation of the deflation basin is regularly seen on coasts with prevailing oblique winds, where one lateral wall is considerably more exposed to erosion than the other (Hesp and Hyde, 1996; Byrne, 1997). A trough blowout orientates its blowout axis slowly in line with the prevailing wind, while the entrance from the beach remains in place (Green et al., 2004). Moreover, the depositional lobe builds out skewed, as wind leaves the throat preferentially from one side (Carter et al., 1990). In areas with strong seasonal climate differences, erosion and deposition in trough blowouts can be variable throughout the seasons (Byrne, 1997). In the colder fall and winter, erosion may dominate, while in the warmer spring and summer seasons this accounts for deposition.

2.2.4 Blowout closure

The transition from a full blowout towards closing is rather a gradual than an abrupt process. In previous research, a full blowout cycle was estimated to take around two decades, in which the process of closure took 5-10 years (Gares and Nordstrom, 1995). Moreover, the cyclic model of trough blowout development includes that a blowout can return from a full blowout to closure, back to a full blowout and eventually back to an incipient blowout (Gares and Nordstrom, 1995; Hesp, 2002; Jewell et al., 2017; Schwarz et al., 2019). The effectiveness of a trough blowout to transport sediment from the beach land inward is a major natural cause for the closure of a blowout. Blowouts close in three ways: 1) increase in size of the blowout (Schwarz et al., 2019), 2) development into a parabolic dune (Byrne, 1997), and 3) growth of incipient foredunes in front of the blowout (Jewell et al., 2017).

Firstly, the increment of the size of the blowout may be the widening of the throat, such that the blowout building acceleration of wind flow is diminished (Gares and Nordstrom, 1995; Jewell et al., 2017). The lateral walls will slump and settle in the throat, creating gentle sloping walls and a decrease in wind velocity. Moreover, the closure of a blowout is supported by the increase of the distance between the deflation basin relative to the lateral walls (Hesp, 2002). If the deflation basin lengthens, wind speed reduces downwind and sand can settle. When pioneer vegetation is able to establish inside the blowout, the closure of the blowout is marked (Schwarz et al., 2019). The topography of the foredune then becomes gradually alongshore uniform again (Gares and Nordstrom, 1995; Hesp, 2002). Secondly, continuous sediment supply towards the depositional lobe can result in the development towards a parabolic dune (Carter et al., 1990; Byrne, 1997; Hesp, 2002; Arens et al., 2013). Grainfall transports sand up to the upper part of the lee slope of the depositional lobe, resulting in oversteepening and avalanching in downwind direction (Hansen et al., 2009). Lastly, blowout closure may be initiated by the growth of incipient foredunes in front of the blowout, reducing the wind speed and sediment transport (Jewell et al., 2017). Once the incipient foredunes in front of the blowout throat become vegetated, the closure of the blowout is marked (Schwarz et al., 2019).

2.3 The role of vegetation

Plant species found in coastal dunes have adapted genetically, morphologically and physiologically to cope with sand burial (Maun, 1998). In coastal dune habitats, sand accretion and erosion are common processes. Therefore, sand burial and erosion are physical restrictions for the vegetation covering the dunes. Vice versa, vegetation restricts erosion (Maun, 1998). Unless restricted sand burial, vegetation is still able to establish and grow in dynamic dune environments. Vegetation in coastal dunes has two major impacts on the morphology: 1) increase in surface roughness and thereby increasing the resistance against erosion, and 2) vegetation halts saltation of grains and stabilizes dunes by their root system (Maun, 1998; Barchyn and Hugenholtz, 2013). The erosional features of the blowout (deflation basin and erosional walls) exert the opposite stress on vegetation establishment as at the depositional lobe (Maun, M. A., 2009; Schwarz et al., 2019).

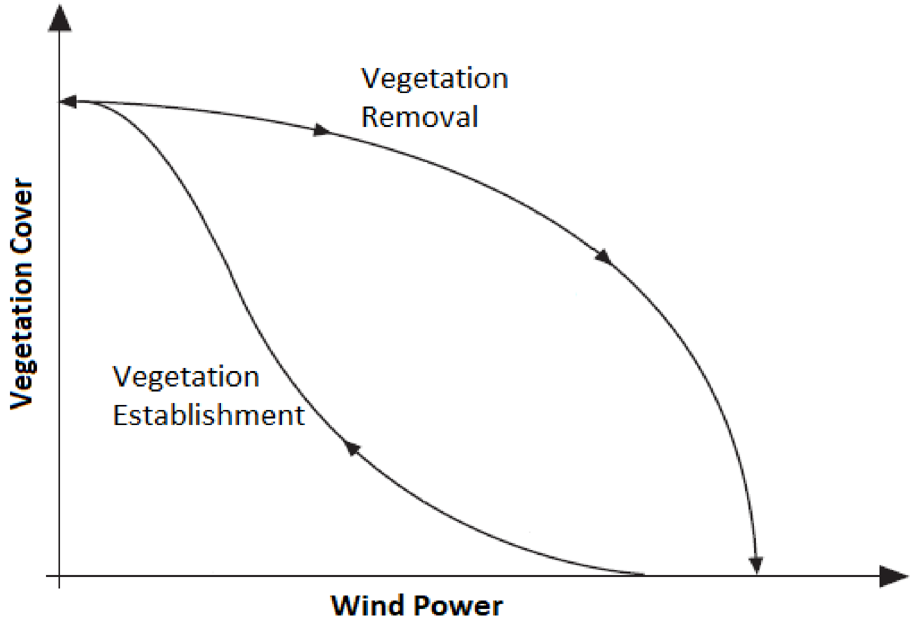

Figure 2-4; Hysteresis effect for coastal vegetation, combining relative wind speed to relative vegetation cover (adapted from Tsoar, 2005).

At the depositional lobe where sand deposition is dominant, vegetation is hindered by continuous burial (Maun, 1998). In coastal foredune blowouts, the burial may be gradual (Ruessink et al., 2018), seasonal (Byrne, 1997) or episodic (Hesp, 2002; Jewell et al., 2017). At the deflation basin and erosional walls, the interaction between vegetation and wind depends on the blowout development stage. Blowout initiation and the development into a full blowout is facilitated by vegetation removal. On the other hand, closure is enhanced by vegetation establishment. Closure is affected by the hysteresis between vegetation cover and wind power (Tsoar, 2005; Barchyn and Hugenholtz, 2013). Namely, the wind energy required to remove vegetation is higher than under which vegetation can establish (Figure 2-4). Consequently, once wind flow is reduced and vegetation can settle in the deflation basin or along the lateral walls, closure of the blowout is advantaged. Seasonal or episodic moments of favored vegetation establishment can thus be crucial for trough blowouts.

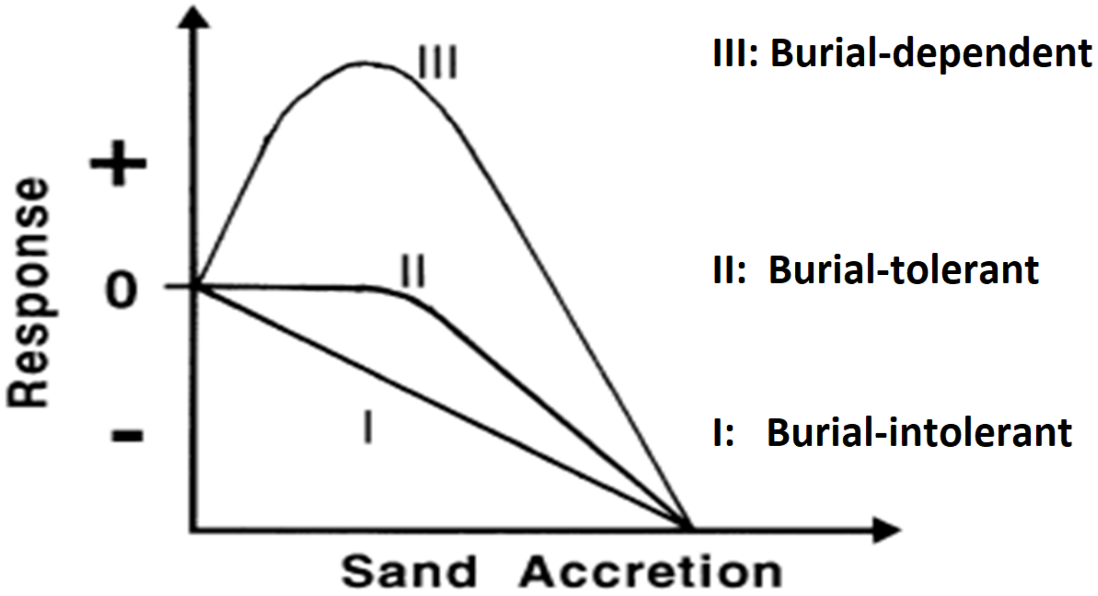

Figure 2-5; Model to show the response of three types of plant species to burial by sand (Maun, 1998).

The resistance of plant species against burial by sand is the most important environmental factor in coastal dunes (Bagnold, 1954). Sand burial affects the zonation (spatial sequence) and succession (temporal sequence) of vegetation in coastal dunes (Maun, 1998). Singular plant species were divided into three classes based on the adaptation to sand burial: 1) non-tolerant to burial, restricted to the inland, 2) sand tolerant, found both inland as on the dunes and 3) sand dependent, found in sandy, active aeolian regions (Maun, 1998; Schwarz et al., 2019; Figure 2-5). In the first place, species that are blown into or washed up onto the shoreline and/or dunes may not be adapted to the vegetation stresses on the beach and coastal dunes. These plants cannot survive in the dynamic beach-dune environment and die soon after germinating due to burial. Secondly, burial tolerant species are initially not affected in their development by sand burial. However, when the vital elements for photosynthesis become buried they die of quite rapidly (Schwarz et al., 2019). Thirdly, plants exist which are dependent on burial. Generally, these plants are especially adapted to live under coastal circumstances and their growth is stimulated by the increase of burial (Maun, 1998). Nevertheless, even burial-dependent plant species die off above a certain limit of sand burial (Maun, 1998).

In an active blowout, the burial rate in the depositional lobe may even exceeds the deposition tolerance of burial-dependent plant species (Barchyn and Hugenholtz, 2013). Subsequently, lowering of the rate of the sand transport towards the depositional lobe can enable this type of vegetation to establish on the depositional lobe (Schwarz et al., 2019). After burial-dependent species can settle, an ecological succession from burial-dependent (III) to burial-tolerant (II) and burial-intolerant takes place, as burial-dependent species operate the least competitive strength (Schwarz et al., 2019). Thus, a decrease in burial rate at the depositional lobe may promote establishment of vegetation, ultimately leading to closure of the blowout.

2.4 Dune management

The primary focus of coastal management has always been the protection against flooding (Arens et al., 2013). Major target was to protect the dunes from erosion, which was typically achieved by the construction of seawalls, groins and dykes, planting of vegetation or the addition of sediment onto the beach or nearshore (nourishments). The addition of concrete structures to protect against flooding is referred to as hard-engineering and is most common in areas where sand availability is the major problem (Yokota et al., 2018). On high-energetic, dissipative beaches where sand supply to the dunes is relatively large and dunes are typically high (Short and Hesp, 1982), planting vegetation on foredunes was common (Hilton et al., 2006; Provoost et al., 2011). The purpose of planting the foredunes was to make them more resilient against wave and wind erosion, which significantly decreased the amount of bare soil and therefore mobile dune area (Arens et al., 2013). These measures stabilized the coastal dunes; sand exchange between the beach and backdunes halts and vegetation fixates the position of dunes. The stability of the foredunes increased and made them an artificial wall between the dynamics of the beach and the dunes (Arens et al., 2013; Muñoz-Vallés and Cambrollé, 2015). This was mentioned for among others Western Europe (Provoost et al., 2011), the USA (Nordstrom et al., 2000), South-Africa (Avis, 1989) and New Zealand (Gadgil, 2002) up to at least the 1990s.

Besides coastal dune management, natural and anthropogenic factors have decreased the natural dynamics in coastal dunes. The stabilization and fixation of coastal dunes were grouped into six major causes (Provoost et al., 2011). (1) Less agricultural activities, such as harvesting of marram grass, wood gathering and cattle grazing is observed in coastal dunes in Western Europe. These changes in land use thus decreased the destruction of vegetation. (2) The large-scale mortality of rabbits due to diseases is linked to an increase in vegetation growth in coastal dunes (Drees and Olff, 2001). (3) Landscape fixation by 'natural and anthropogenic factors' such as the fragmentation of the landscape which hinder large scale geomorphological processes (Provoost et al., 2011). This decreases the dynamic aeolian transport of dunes and increases the potential for succession of vegetation. (4) Eutrophication has increased primarily grass encroachment in coastal dunes (Arens et al., 2013), caused by the doubling of atmospheric nitrogen deposition compared to pre-industrial times (Provoost et al., 2011). (5) Climate change differs worldwide, but most probable has led to an increase in the growing season, rainfall and temperature and CO_2 concentrations, resulting in an increment of biomass (Arens et al., 2013). (6) Classical coastal dune management, such as planting of marram grass to stabilize dunes, has increased the stability of especially the foredune (Gadgil, 2002; Arens et al., 2013).

The natural and anthropogenic processes stabilizing dunes have had a large impact on the ecological value of coastal dunes (Provoost et al., 2011; Arens et al., 2013). Although stabilization can be a positive mechanism for the protection against dune erosion and flooding (Gadgil, 2002), stabilization or, more extremely 'overstabilization', decreases the biodiversity and ecological value (Provoost et al., 2011; Arens et al., 2013). A decrease of biodiversity is marked as the shift from pioneer vegetation to climax vegetation, indicated by one or several plant species outcompeting all lower stage vegetation. Traditional coastal management strategy focused primarily on the resilience against erosion and decreased the biodiversity. From the 1970s, awareness has grown that dynamic and young natural systems have a large ecological value and should be brought back into coastal dunes (Van Boxel et al., 1997; Van Koningsveld and Mulder, 2004; Mulder et al., 2011). For example, the Dutch government adapted the "Dynamic Preservation" policy in the year 1990, introducing country scale sand nourishments to preserve the coastline while recognizing the ecological value of the coastal environment (Van Koningsveld and Mulder, 2004). On a continental scale, the European Union recognized that coastal dunes in Europe are in threat and developed the Natura 2000 areas to protect natural areas (Houston, 2008). The Australian coast was losing ecological value as coastal management was only concentrating on hazard protection and human recreation (James, 2000). Therefore, the focus of coastal dune management around the globe has shifted towards reintroducing ecological diversity and increasing natural dynamics in dunes systems (Arens et al., 2005; Provoost et al., 2011; Kelly, 2016). The 'Eurosion' project in Europe recommends to restore the sediment balance in coastal areas by giving space to natural processes and creating 'strategic sediment reservoirs' (Salman et al., 2004). The latter should provide sediment to act as a buffer zone during sea hazards and to adjust to Sea Level Rise (SLR). The ecological value of the grey dunes, just landward of the foredune, was highest as the plant species diversity was largest (Peyrat and Fichtner, 2011).

From a management point of view, it is desired that after reintroducing natural dynamics in dunes, minimal to no effort is needed to continue the destabilization (Arens et al., 2013). This can be referred to as the 'self-maintaining' capability of a project (Ruessink et al., 2018). Previous projects along the Dutch coast failed to be self-maintaining (Arens et al., 2004; Kooijman et al., 2005). After vegetation removal to reactivate aeolian dynamics in the back dunes, the areas stabilized within a decade as 1) they were relatively small, 2) their shape was not well elongated, decreasing the fetch of the wind and, 3) their location was over 500 m inland, sheltered from the dynamics of the beach (Kooijman et al., 2005). Large scale nourishment project failed to increase aeolian dynamics. The nourished sand was from deeper-sea origin, contained larger grains and more shell fragments, and therefore created an armor layer decreasing aeolian deflation (Hoonhout and de Vries, 2017).

One of the most promising measures is the excavation artificial trough blowouts in the foredune. As previous measures in the backdunes were not self-maintaining, it was hoped that the more severe wind dynamics on the beach would lead to less vegetation establishment (Arens et al., 2013; Riksen et al., 2016). Notches in the foredune were constructed to facilitate aeolian sand transport from the beach into the backdunes (Riksen et al., 2016; Ruessink et al., 2018). Foredune blowouts allow for the input of calcareous sand into the backdunes, decreasing the acidity of the soil, beneficial to the endemic plant species. Also, climax vegetation, such as shrubs and tall grasses, can become buried completely by the sand, opening possibilities for pioneer species. Thus, this dune managing project focuses on stimulating aeolian dynamics to stop, or preferably, reverse the present-day decline in dune biodiversity. The excavation of the foredune notches is hoped to be self-maintaining, as the aeolian dynamics on the beach are more severe than in the backdunes, remaining roots are removed from the soil and salt spray diminishes possibilities for vegetation close to the shoreline. Trough blowouts also serve as a pathway to the beach. Major drawback is that it can only be constructed up to the extreme storm surge height or where flooding is tolerated. This type of dune management hopes to combine human recreation, an increase of biodiversity and possibilities to keep up with SLR.

In Ameland, a barrier Island in the North of the Netherlands, artificial blowouts where excavated in the foredune as a current management strategy (Riksen et al., 2016). There was a supply of fine-grained sediment into the backdunes and an effect on the vegetation in the white dune habitat, though the changes were limited to a maximum of 65 m from the foredune crest (Riksen et al., 2016). The authors claimed that the limited supply was linked to relatively small size of two of the three artificial blowouts

(16 and 21 m) and recommend that a larger width of the blowout throat may enhance the input of sediment. Fortunately, limited maintenance was required in the first five years after construction of the notches. Another project was done in Kennemerland, along the western coast of the Netherlands. Five notches were excavated in stabilized foredunes to reintroduce the connection between the beach and dune system. They resemble natural trough blowouts and focus on bringing back beach sand into the backdunes by aeolian processes (Ruessink et al., 2018). These notches were, when excavated, V-shaped (looking onshore), between 50 and 100 m width and 9 to 12.5 m deep (Ruessink et al., 2018). Although over just the first three years of observation, these relatively large artificial blowouts show a significant increase of the sand in the backdunes, require little to no maintenance and return aeolian dynamics into the backdunes (Ruessink et al., 2018). This suggest the idea that artificial foredune blowouts can be a very effective coastal dune management strategy. It may increase the backdune biodiversity by reintroducing the aeolian dynamics and naturally add volume to the dunes by the throughput of sediment from the beach. Though these features are yet dug into the foredunes, decadal scale observations of natural foredune blowouts are only scarcely present. This emphasizes the need for knowledge on the decadal scale development of natural foredune blowouts.

3 Satellite Imagery: a tool to study dunes

In this research, foredune blowouts will be analyzed using satellite imagery. Accordingly, this chapter introduces the application of satellite imagery to study coastal areas. The first section gives a general overview of the cloud-computing platform in which the analysis is performed. Secondly, spectral remote sensing will be presented by means of four types of resolutions. Thirdly, the challenges for detecting trough blowouts in foredunes from spectral satellite imagery will be described. The last section presents the data sources used throughout the research.

3.1 Cloud-computing

The objective of this research is to provide insight in natural, long-term development of foredune blowouts at three different sites worldwide. Accordingly, the data requires 1) a global availability, 2) sufficient temporal availability, and 3) a spatial and spectral resolution satisfactory to capture the blowouts. The research was restricted to freely available datasets. Fortunately, freely available data have become abundant in recent years: the European Space Agency (ESA) gave free their COPERNICUS missions (ESA, 2019), while variable datasets including the Landsat archive and Moderate Resolution Imaging Spectroradiometer (MODIS) are released by NASA, U.S. Geological Survey and NOAA (Woodcock et al., 2008; Loveland and Dwyer, 2012).

Geospatial analysts need to deal with four major information technology challenges: 1) data intensity, 2) computing intensity, 3) concurrent intensity, and 4) spatiotemporal intensity (Yang et al., 2011). Firstly, the storage, processing and expansion of geospatial datasets is enormous, and global datasets requires large-scale datacenters to be stored (Cui et al., 2010). Secondly, computation of algorithms and models on geospatial datasets are often complex and the execution of the process is time consuming, which is not possible to run locally on single computers. Moreover, the number of end users simultaneously accessing geospatial datasets is increasing (Goodchild, 2007). Lastly, the advancement of technology has enabled us to measure both spatially as temporally more accurate, increasing the intensity of geospatial datasets (Goodchild, 2007).

Therefore, geospatial research is favored when conducted on external computer resources, which in a more popular term is called cloud computing (Gorelick et al., 2017). It is an upcoming manner to process geospatial data for any kind of users, as generally only a simple computer and an internet connection is required (Yang et al., 2017). A large variety of these cloud computing tools has developed over the past two decades to support the large scale analysis of geospatial data, examples including TerraLib (Camara et al., 2000), Hadoop (Whitman et al., 2014), GeoSpark (Yu et al., 2015), GeoMesa (Hughes et al., 2015) and Google Earth Engine (Gorelick et al., 2017).

In this research, the Google Earth Engine (GEE) platform was chosen as processing software. Because of the large availability of global satellite imagery and the easy-access to the web-based program. Moreover, users without a high level of remote sensing experience get easily started through the internet-based application programming interface (API) and interactive development environment (IDE) (Gorelick et al., 2017). The bulk of the available geospatial dataset in the GEE consist of the Landsat and MODIS archive provided via the U.S. Government and the Sentinel-1 and Sentinel-2 missions by the ESA, as well as a variety of climate, land cover and socio-economic datasets (Gorelick et al., 2017). Although other data sources and private data can be uploaded to the GEE, that still requires data to be processed and stored locally. The GEE provides fast visualizations in their web-based IDE, which enables easy testing and validation of produced results. Moreover, it is very well-suited for time-series analysis of stacks of images (Gorelick et al., 2017). Tools available in the GEE are based on ‘standard’ remote sensing techniques but used in a different (software) environment. Where possible, the literature background of the remote sensing techniques is added, although the library of functionality in the GEE usually lacks clearly defined background literature.

3.2 Resolutions in Remote Sensing

In earth observation, the objective is to measure radiations of the earth's surface and atmosphere. This radiation can either be emitted by the source itself (passive) or reflected by the source when artificial radiation is emitted (active). Passive remote sensing consists of sensors that capture radiation naturally reflected or emitted by the earth’s surface and atmosphere. In can be split into the solar-reflective spectral range (from 0.4 µm to about 3 µm) and the self-emitted thermal radiation (generally above 5 µm) (Schowengerdt, 2006). Both are defined as the spectral range where their energy dominates. On the other hand, active remote sensing is the technique where an artificial source of energy, normally emitted from the satellite itself, scatters back to the sensor and characterizes the earth's surface or atmosphere (Schowengerdt, 2006). An example of passive remote sensing is radar, which transmits electromagnetic waves in the radio of microwave area and detects the backscattering radiation to determine an object’s location and speed. Here, passive remote sensing is considered as no active remote sensing platform yet has decadal scale temporal coverage within the GEE.

Besides the type of the radiation detected, earth observation data can be characterized by four types of resolutions: spatial, spectral, radiometric and temporal (Klemas, 2010). Spatial resolution is no more than the ground area detected by each single rectangle element in the image, which is referred to as the pixel size. The pixel size is generally a measure of the distance of a side of the rectangle element. When the pixel is a square, which is the case in current satellite missions such as Landsat-7 and Landsat-8 and Sentinel-2, the spatial resolution is given as a single distance (e.g. 10 m, 1 km, etc.), describing only the side-length of a square pixel.

The spectral resolution indicates the specific wavelength interval at which a sensor records radiation (Klemas, 2010). In a normal color photograph, usually only the visible part of the electromagnetic spectrum, ranging from 0.38 µm till 0.74 µm (Starr et al., 2010), is recorded. In more advanced digital sensors, the infrared (IR) part of the spectrum is also recorded, which can be divided into near-, shortwave-, mid- and thermal-IR (Figure 3-1). The effectiveness of a satellite sensor to capture data of the Earth’s surface is strongly related to the spectral wavelength which penetrates through the atmosphere (Casey et al., 2012). The spectral range of light penetrating the atmosphere is described as an atmospheric window (Figure 3-1). In digital imagery, the spectral information is given as the number and location of wavelength intervals with a range of sensitivity at which is recorded (Jensen, 2009). Each wavelength interval is referred to as a ‘band’ and is generally given a standardized, human readable name, such as ‘green’ or ‘Near-Infra-Red’ (NIR). As an example for spectral resolution, multispectral sensors capture the electromagnetic spectral usually in 4 to 12 singular bands with intervals of about 30 till 400 nm (Woodcock et al., 2008; ESA, 2015a), while hyperspectral sensors cover the electromagnetic spectrum over 200 bands with intervals as close as 10nm (Green et al., 1998).

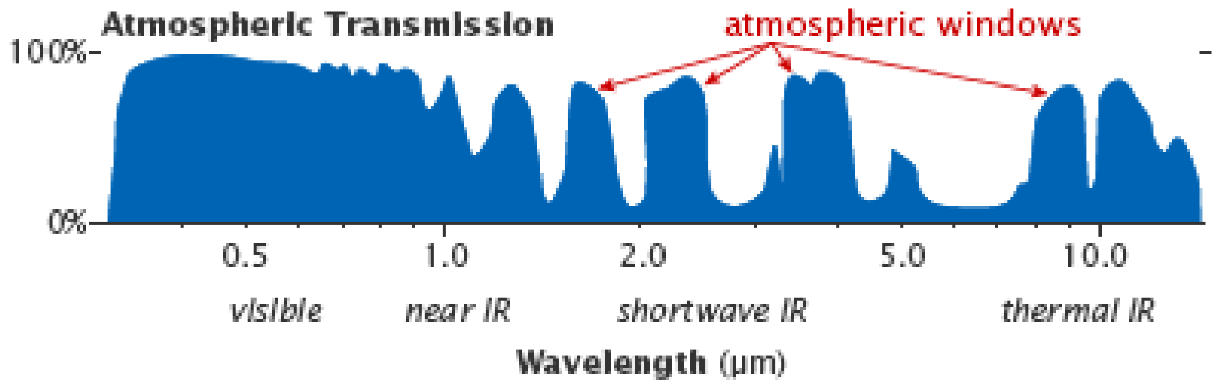

Figure 3-1 Schematic overview of the electromagnetic spectrum which percentage of light penetrates through the atmosphere. Regions where much light penetrates are called atmospheric windows and allow satellites to view the Earth's surface. Figure adapted from Casey et al. (2012).

The radiometric resolution is a measure of the sensor to discriminate between two objects with similar reflectance. Thus, the radiometric resolution is the capability of a sensor to segregate subtle spectral differences between pixels. The radiometric resolution has evolved over time, as it is basically a measure of the sensors quality and the ability to store data into higher levels of bits. As an example, the raw data of the Landsat Thematic Mapper (TM) and Enhanced Thematic Mapper (ETM+) launched before 2000 are collected using 8-bit (i.e. 256 different levels of reflectance) (USGS, 2018a), while the Landsat Operational Land Imager (OLI) sensor launched in 2013 collects visible and IR bands at 12-bit (i.e. 4096 different levels of reflectance) (USGS, 2019a).

The temporal resolution indicates how often a specific region is sampled by the sensor. It thus described the resolution of a stack of images over time. Satellites sensors used in this analysis are polar-orbiting satellites, which pass (nearly) above both poles of a planet or moon. As the earth is rotation, the satellites pass each circulation at another longitude. The altitude and speed are chosen in such a way that the satellite passes each consecutive orbit at the same local time of the day. As an example of temporal resolution, the MODIS satellites revisit every location on earth in one to two days, while the Landsat 7 and 8 satellites revisit every location every 16 days.

3.3 Land Cover features in foredune blowouts

At the pixels size of medium-resolution satellite imagery (10-30 m), individual pixels are inherently made up of a mixture of features. Their reflectance then mixes into the spectral information of a single pixel, which causes a so-called 'mixed pixels' (Hugenholtz et al., 2012). Mixed pixels consisting of two distinctive land cover features may be present at the border of both features. Also, mixed pixels exist by mixing of two features within a pixel, if the features are smaller than the pixel size.

3.3.1 Define the objects to classify

In chapter 0, a blowout was characterized by three main features, namely the erosional walls, the deflation basin and the depositional lobe. These three features are typically characterized by their non-vegetated nature. Strong winds inside the throat unable vegetation to establish, while deposition on the lobe generally buries vegetation on the landward side of the blowout. Consequently, the analysis of satellite imagery will focus on separating the blowout from the surrounding landscape. Spectrally, there can be three main land cover types distinguished. This is represented by the UAV orthophoto shown in

Figure 3-2a. Firstly, water can be separated from the land, as indicated in blue. This can either be the sea or a large lake surrounded by sandy dunes (e.g. Dech et al., 2015) and inland lakes or dune ponds (Figure 3-2a). Secondly, (dune) vegetation can visually be separated as the green part on the right side of Figure 3-2a. Lastly, the bright surfaces are the bare sand areas. These are presented by 1) the beach and unvegetated embryo dunes (yellow), and 2) the foredune blowouts and backdune unvegetated areas (red), denoted with respectively an N and a U plus a consecutive number from south to north. Summarizing, three major land cover classes could be defined from the spectral imagery in the study area around trough blowouts: 1) sand, 2) vegetation and 3) water. A more comprehensive classification was required to subtract only the area of the trough blowouts from the sand-classified area.

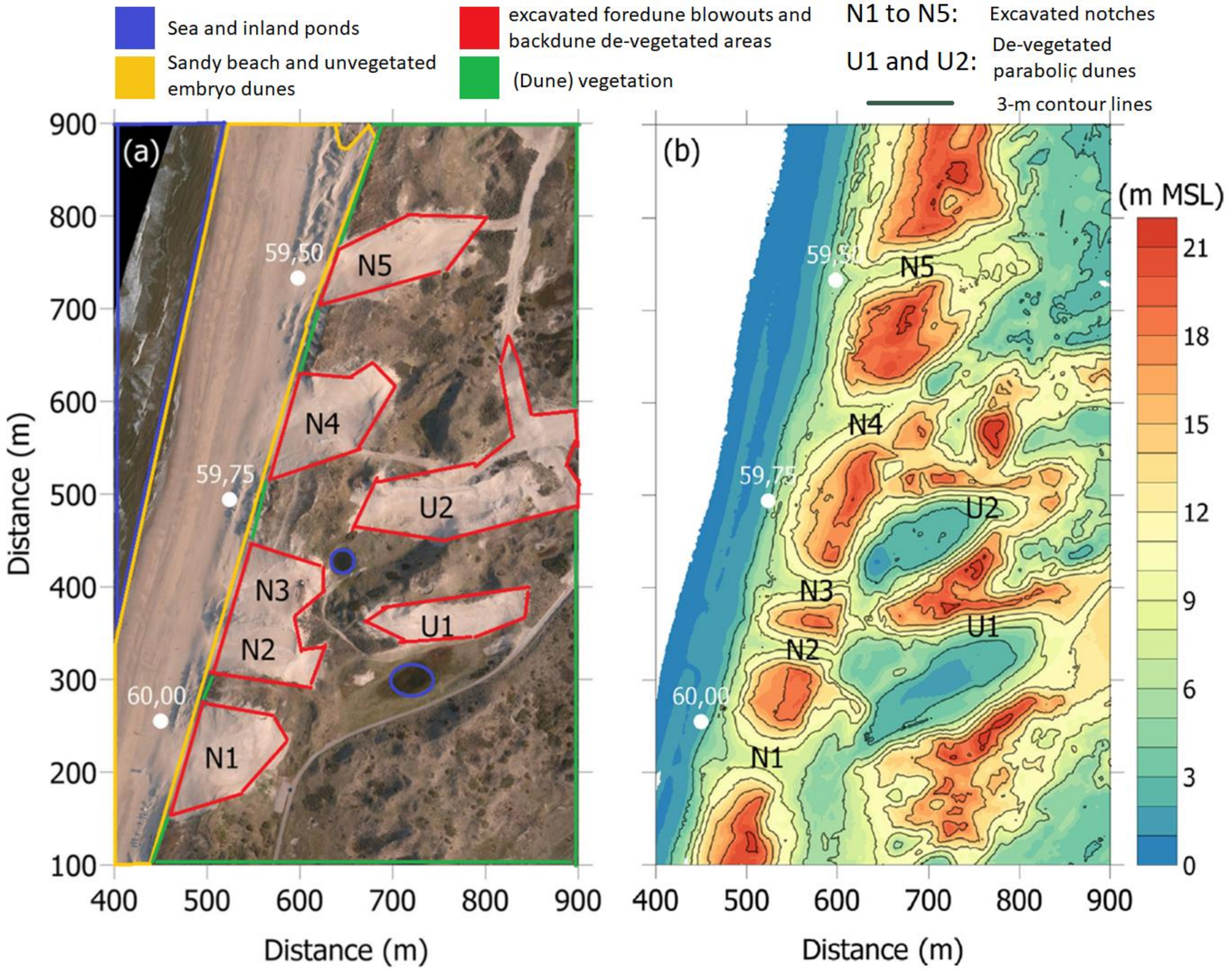

Figure 3-2; Overview of the five excavated foredune notches (blowouts) in Zuid-Kennemerland, with (a) an orthophoto of high-resolution UAV images, obtained on 1 May 2013. (b) Elevation based on a Digital Terrain Model (DTM) from the UAV images with respect to the mean sea level (Ruessink et al., 2018). For a more detailed overview of this data collection, the reader is referred to Ruessink et al. (2018).

3.3.2 Spectral signature foredunes

The spectral signal is usually described as a reflectance value, a ratio between the reflected and incident radiation (Provoost et al., 2005). As light observed by a satellite's sensor passes the atmosphere, the reflectance of a ground feature is given as a mixture of the atmosphere and earth's surface constitution. As the atmosphere changes the actual spectral signal of ground features, the pure spectral signal of land cover features is measured at the earth's surface (using e.g. a field spectrometer), and is referred to as an endmember (Provoost et al., 2005).

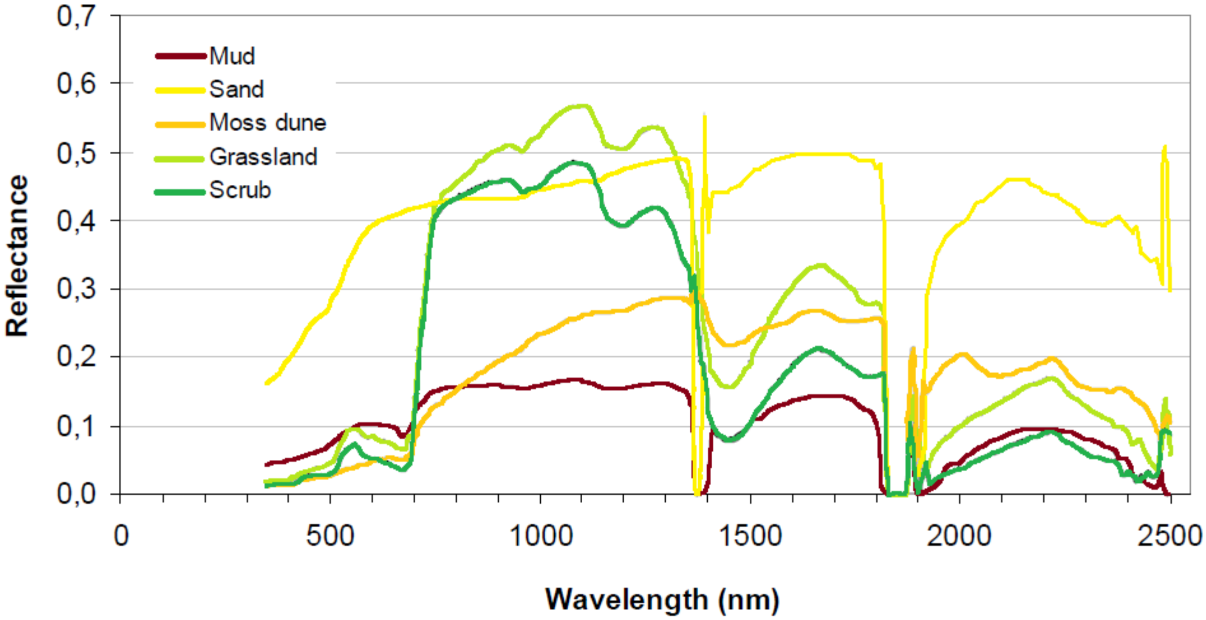

Figure 3-3; Spectral endmembers from some characteristic coastal habitats along the Dutch and Belgium coast. Figure for visibility purpose coloured from Provoost et al. (2005).

A good overview of the reflectance curves of typical endmembers found in the Dutch and Belgium dunes is found in Figure 3-3. Three types of vegetation (grassland, moss dune and scrub), sand and mud were measured using a field spectrometer. It should be noted that at the time of measurement, the moss dune (*Tortula ruralis ssp. ruraliformis*) was dried out, explaining the non-vegetation behavior in the Near-Infrared (NIR) wavelengths in Figure 3-3 (Provoost et al., 2005). Important for the observation of trough blowouts is the remarkable difference between bare sand and vegetation. Whereas vegetation is low in the visible wavelength (with a relative peak in the green light), sand is relatively high in the visible wavelengths. This makes it relatively simple to discriminate between healthy (green) vegetation and bare sand (Provoost et al., 2005), while that is less straightforward for the dried out (i.e. non-photosynthetic vegetation) moss dune. Within the shortwave infrared wavelength (±1400–3000 nm), however, the spectral signal of dried out vegetation can be separated from that of bare soil (Hugenholtz, 2010). Thus, for a complete analysis of the vegetation and bare sand, the spectral resolution of the satellite data preferably covers the visible and near-infrared wavelengths to distinguish between bare soil and healthy vegetation, and additionally the shortwave infrared part of the spectrum to separate bare soils from non-photosynthetic vegetation. Furthermore, the water content of an area is usually absorbed in the shortwave infrared wavelengths at about 1400 and 1850 nm. This results in low reflectance at these parts of the spectrum, similar to the depressions between atmospheric windows (Figure 3-3).

Contradictory, there is no clear spectral difference between the beach, the backdune de-vegetated areas and the foredune blowouts (Figure 3-2a). Therefore, separation of the beach with the trough blowout was done differently, explained in the methodology (section 0). Furthermore, visually there is no clear difference between trough N2 and trough N3, though the elevation model shows that there is a clear separation between the second and third throat (Figure 3-2; Ruessink et al., 2018). Consequently, single throats cannot be distinguished singularly from the satellite images if 1) there is no spectral difference between the throats, or 2) the spatial resolution of the imagery is not adequate.

3.3.3 Challenges in coastal sand dunes detection

Challenges in the classification of land cover types in sand dunes are present (Hugenholtz, 2010). Four major difficulties are encountered in the analysis of coastal dunes using satellite remote sensing data (Hugenholtz, 2010): 1) 'mixed pixels'; 2) the effect of topographic variations; 3) seasonal variability and, 4) transferring remote sensing to evolutionary models.

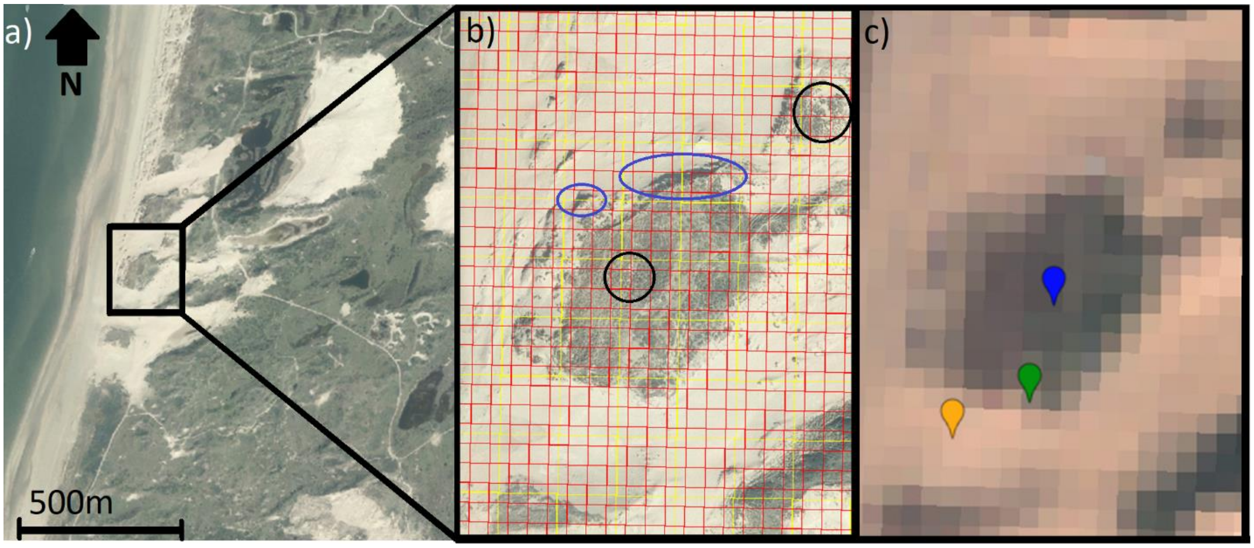

Figure 3-4; a) 25 cm orthophoto of the Kennemer Dunes taken in the summer of 2018 (provided by the Dutch government), with b) a close-up of the black box. In b), the red grid represents the outline of Sentinel-2 (10 m) pixels, while the yellow grid represents the Landsat-8 (30 m) pixels. c) RGB presentation of a Sentinel-2 scene on 6 May 2018 of the black boxed area. See further explanation in the text.

An example of the 'mixed pixels' problem is presented in Figure 3-4. Mixed pixels result in a mixed spectral response of the classes within the pixel (Figure 3-5). Obviously, it is shown that the spectral response of the mixed pixel (green) is a mixture of the vegetated (blue) and sandy (orange) pixels. Mixed pixels are inherently present for dune vegetation for satellite imagery. On nadir-looking images, vegetation is sparse so that sand can be seen through the vegetation (black circles in Figure 3-4b), as a result of the typical nature of dune vegetation such as marram and beach grasses (Maun, 1998; Hugenholtz et al., 2012). Subsequently, on the spatial resolution on for example Landsat-8 or Sentinel-2 imagery (respectively 30 m and 10 m), even a pixel on a completely vegetated foredune will contain a spectral mixture of both sand and vegetation.

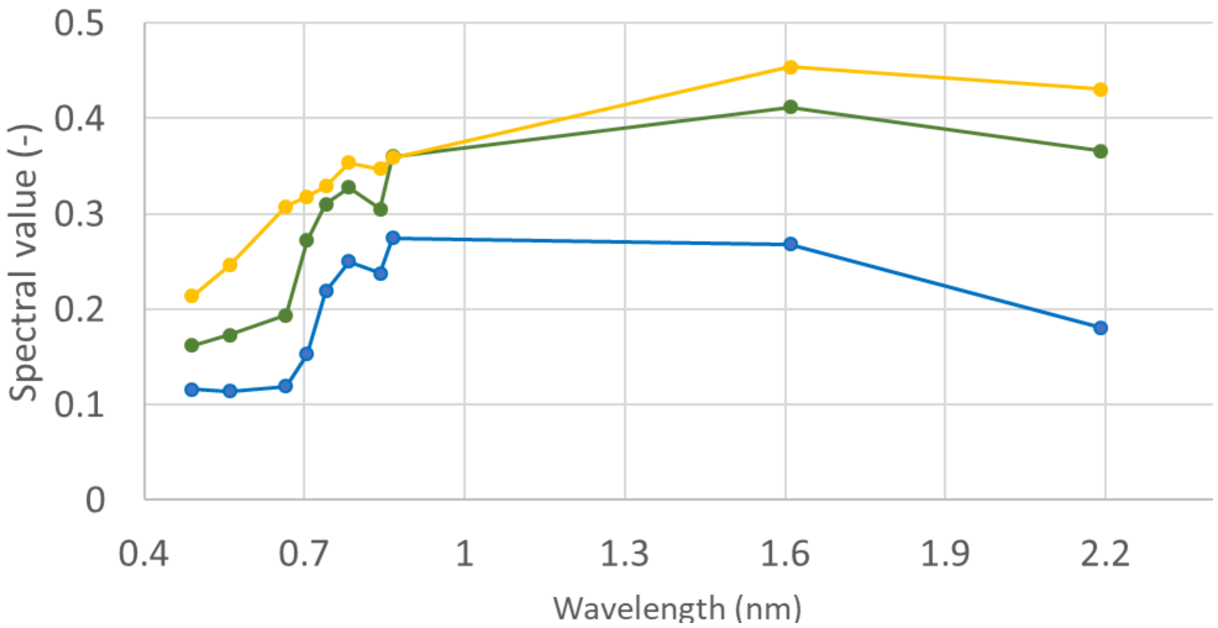

Figure 3-5; Spectral reflectance curve of three sample points of a Sentinel-2 scene at 6 May 2018, where the colours correspond to the markers in Figure 3-4c.

A second difficulty is caused by the irregular topography of sand dunes, yielding to solar illumination differences. The reflectance detected by the sensor differs at varying facing slopes due to the different scattering of the sun's radiation (Richter, 1997). Moreover, identical land cover features will reflect a different signal if one is covered (partly) by shade (blue circles Figure 3-4b). This is a common process at the higher latitudes during the winter months, when the solar inclination angle is highest. Thirdly, vegetation growth in coastal dunes is commonly a seasonal process, resulting in a varying spectral signal of vegetation throughout the year (Hugenholtz, 2010). Subsequently, different reflectance curves for a similar plot of vegetation are present throughout the year. A main objective of this research is to find seasonal patterns of blowout development. Accordingly, an adequate temporal resolution of the timeseries is required to verify in what way the spectral signal is affected by seasonal growth and decay of dune vegetation. Fourthly, it is difficult to translate data derived from satellite imagery to a process-based development of dunes. Ground-truth measurements, for example wind flow velocities, then have to be included in remotely observed satellite data. These ground-truth validation data are typically derived at different temporal and spatial scales, and therefore difficult to implement in process-based models.

3.4 Data sources

In this research the passive remote sensing data from the Landsat (TM, ETM+ and OLI) and Sentinel-2 missions are considered. These satellite platforms fulfill the spatial, spectral and temporal resolutions required to monitor the foredune blowouts. The Landsat and Sentinel-2 missions are made in such a way that they build upon each other to sustain long-term, comparable remote sensing data. Nevertheless, the inter-satellite differences in resolutions require an independent description.

3.4.1 Landsat missions

Landsat mission used in this analysis are the multispectral images with a 30 m spatial resolution. The Landsat 4 and Landsat 5 satellites, comprising the Thematic Mapper (TM) sensor, were launched in 1982 and 1984. In 1999, the Enhanced Thematic Mapper Plus (ETM+) sensor, on board the Landsat 7 satellite was launched. The Operational Land Imager (OLI) on board the Landsat 8 was added in 2013. Landsat satellites are polar orbiting satellites and each sensor returns at the same location above the earth after 16 days. The Landsat scene swath width is approximately 185 km, while the north to south length is generally 170 km, and consecutive rows have an overlap of several to 10 kilometers. As an example of the image availability over time, an overview of the Landsat images present per satellite per year for the study area Haurvig is given in Figure 3-7. Less imagery was present for the early days of the Landat-4 and Landsat-5 missions due to selective archiving of the data provider.

Landsat products are placed into two collections, where all scenes in the Tier 1 collection satisfy the image-to-image tolerance of <12 m radial root-mean-squared-error (RMSE), while that was not matched or could not be determined for Tier 2 products (USGS, 2018b). The Tier 2 collection does contain useable images, because of its geometric insecurity of accuracy (Young et al., 2017). Therefore, the Landsat image collection was limited to only the Tier 1 collection.

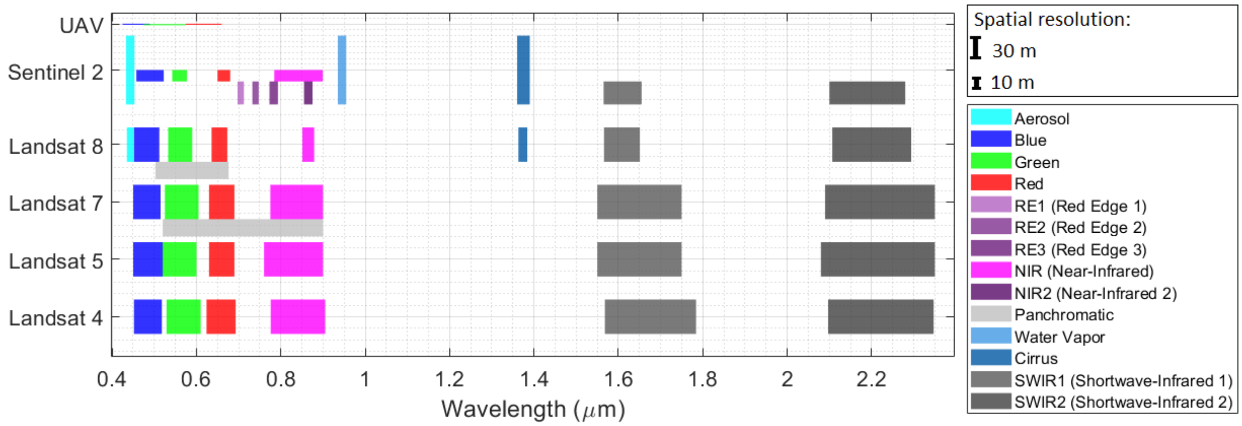

Figure 3-6; The spectral and spatial resolution of the bands across the five satellites and the UAV imagery. The spectral resolution is given as the horizontal length of the rectangles, while the vertical length depicts the spatial resolution. The spatial resolution of the UAV images is 1 m. Data obtained from: (USGS, 1984; USGS, 2001; Chander et al., 2004; Bongiorno et al., 2013; ESA, 2015b; USGS, 2019a). The names and abbreviations for the bands are chosen as they are generally named and subsequently used throughout this research.

Landsat satellites capture the electromagnetic spectrum in both the solar-reflective spectral range as the self-emitted thermal radiation. In this research, only the solar reflective spectrum is used as the spatial resolution of the Thermal-Infrared (TIR) bands of the Landsat satellites have a too low spatial resolution

(90-120 m) to be valuable for detecting coastal trough blowouts. Figure 3-6 shows the visible and Near- and Shortwave-Infrared bands (abbreviated further as NIR and SWIR) used in this study for the five different satellites. Over the years, the spectral resolutions of the satellites increased, for example the bandwidth of the red band narrowed over time, increasing the difference between the signal of the bands. Aside from the differences in spectral resolution, there was an increase in radiometric resolution. The earlier Landsat missions (4, 5 and 7) were captured in 8-bit, while the Landsat 8 data was captured in 12-bit (stored as 16-bit), representing respectively 256 and 4096 levels of precision (Chander et al., 2009). By the increase in spectral resolution, minor inter-pixel differences are more likely captured. Also, band saturation greatly reduced on the 12-bit Landsat-8 platform (Roy et al., 2016).

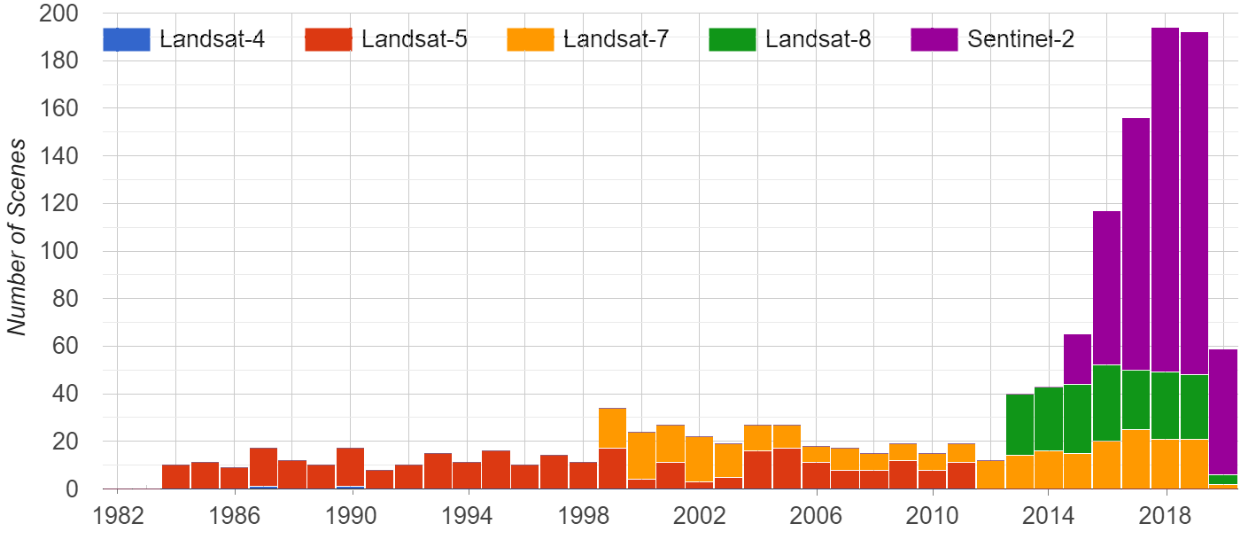

Figure 3-7; Daily Landsat (4, 5, 7 and 8) and Sentinel-2 scenes available in the GEE up to 12 May 2020 for Haurvig, Denmark. The Landsat scenes only include the Tier 1 collection. See for code: B-1

As from May 31 2003, the scan-line-corrector (SLC) of the Landsat 7 ETM+ sensor failed, resulting in missing stripes of pixels within each image, increasing in width from the scene center passing location (Figure 3-8). These images could still be used in the process, though missing pixels required to be filled (Scaramuzza and Barsi, 2005; Khattab and Merkel, 2014; Hossain et al., 2015). The SLC failure reduced the total number of pixels to 78 percent of their original, while the cover is decreasing towards the edges of the scene.

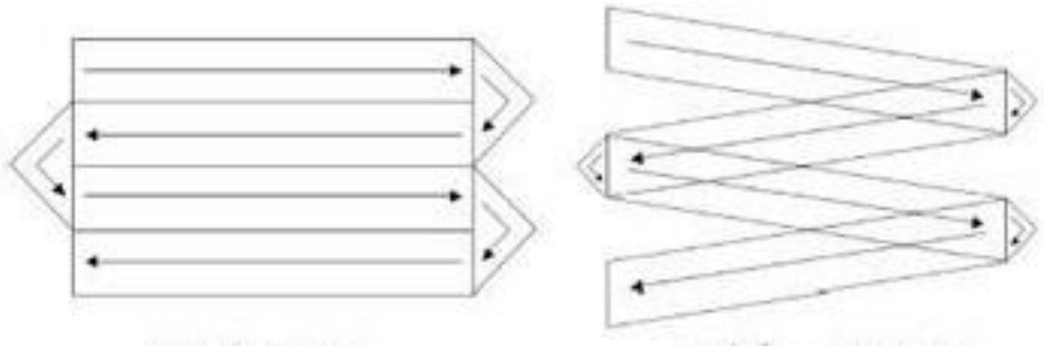

Figure 3-8; Schematic overview of the Landsat 7 ETM+ sensor capturing data with (left) and without (right) the Scan-Line-Corrector (SLC) (USGS, 2019b).

3.4.2 Sentinel-2

The second Sentinel mission of the ESA is the Multi-Spectral Instrument (MSI) on board the Sentinel-2A and -2B, launched on respectively 23 June 2015 and 7 March 2017. These polar orbiting satellites fly sun-synchronously on an altitude of 786 km with a return period of ten days, while together they deliver data with a five-day return period above all continents and European islands (Martimort et al., 2007; ESA, 2015b). Consequently, there was a clear increase of the temporal resolution when the Sensitnel-2B was launched in March 2017 (Figure 3-7). As the constellation of the MSI on board both satellites are similar, this section will describe the Sentinel-2A and -2B satellites further just as the Sentinel-2 dataset.

The Sentinel-2 satellites capture the earth's surface with a swath width of about 290 km. The imagery is collected in long, continuous observations, which is referred to as a single datatake (ESA, 2015b). However, the Sentinel-2 L1C data used in this analysis are delivered by ESA in user-ready granules of approximately 100x100 km in UTM-based Military Grid Reference System (MGRS) (ESA, 2015b). These granules usually have a small overlap of 9780 m (Claverie et al., 2018). In contrast to the Landsat satellites, the spatial resolution of the bands within the solar reflective spectrum is adapted to the application of the spectral wavelength of the bands: 10 m for the visible and broad NIR band, 20 m for the red edge, narrow NIR and SWIR bands and 60 m for the atmospheric bands (named aerosol, water vapor and cirrus) (Figure 3-6). The addition of the red edge bands was to segregate vegetation better and has shown to be effective (Immitzer et al., 2016; Forkuor et al., 2018) and was added as an additional data source compared to the Landsat dataset. The radiometric resolution of the MSI is 12-bit (4096 levels) and has an accuracy of less than 5% (ESA, 2015b).

3.4.3 Atmospheric Correction

Spaceborne spectral satellite data is generally delivered in four levels of products: 0) Raw data, 1) Top of the Atmosphere (TOA), 2) Bottom of the Atmosphere (BOA) or Surface Reflectance (SR), and 3) applications-ready products. For the Sentinel-2 and Landsat data, level 0 refers to uncalibrated, raw data obtained from directly from the satellite. Level 1 data refers to radiometric and geometric corrected data, including spatial registration and orthorectification using terrain models. For Sentinel-2, this is the lowest data made available to the public. The level 2 products are corrected for the atmospheric radiation and includes processing using the Sen2Cor algorithm (Sentinel-2), LEDAPS algorithm (Landsat 4, 5 and 7) and LaSRC algorithm (Landsat 8) (ESA, 2015b; Foga et al., 2017). Level 3 products is user-ready data, such as the water area extent, burned area information or snow cover area (USGS, 2019c).

In spaceborne spectral imagery, atmospheric correction algorithms exist to obtain level-2 products as the detection of ground features suffers from the interference of radiation by the atmosphere and the background (Vermote and Kotchenova, 2008; Hagolle et al., 2015). Molecules in the atmosphere interfere with the ground signal to detect, while at the earth's surface materials with different spectral properties are measured within one pixel. For example, the detection of a maize crop with a pixel size of 30 meter will be interfered by the underlying soil, which can either be wet or dry, resulting in a different spectral background value. Consequently, single band signals are dependent on the image-specific atmospheric conditions and variation of the background features. Especially the visible and NIR part of the electromagnetic spectrum are susceptible for atmospheric radiation (Donchyts et al., 2016). Therefore, level-2 atmospheric products are produced, which aims at producing images where all pixel spectra represent data of nearly the same albedo. As such, each pixel spectra can directly be compared with each other (Van der Meer and De Jong, 2011).

However, the process of atmospheric calibration involves the inclusion of lower spatial resolution bands then the actual resolution of visible, NIR and SWIR bands (Donchyts et al., 2016). For Landsat 4, 5 and 7, the atmospheric correction includes the use of the 90-120 m resolution thermal bands to correct for the 30 m resolution used in this analysis. Moreover, atmospheric correction for the Sentinel-2 satellites includes the 60 m cirrus, water vapor and aerosol bands to correct the 10 and 20 m visible, NIR and SWIR bands. The coarser resolution products may introduce local errors, even though the overall spectral signal of the image increases. Additionally, one of the known issues of the Landsat atmospheric correction algorithms is that the effectivity of surface reflectance data is reduced in coastal areas, regions with low sun angle and arid or snow-covered regions (USGS, 2018a; GEE, 2019; USGS, 2019d). Although atmospheric correction may result in an overall better spectral signal of a satellite scene, for single image-based classification the correction for the atmospheric variations may not be necessary (Song et al., 2001). Namely, single scene analysis examines differences in pixels with similar atmospheric conditions. Consequently, this research focusses on the Top of the Atmosphere (TOA) satellite imagery of Sentinel-2 and Landsat 4-8. The methodology will motivate that the use of TOA images is adequate, as exclusively differences between two bands were used to accommodate for inter-image differences.

3.4.4 High-resolution UAV imagery

Additional high-resolution data was obtained between 2014 and 2017 using an Unmanned Aerial Vehicle (UAV). This is an airborne imagery technique generally providing high spatial resolution data, although the temporal resolution is variable due to the need of intensive human labor. The high-resolution UAV was used to validate the moderate resolution Landsat and Sentinel satellite imagery. This section provides a short overview of the used UAV imagery.

Table 3-1; Overview of the UAV images used within the analysis. The number of pixels is the number of valid pixels within the 500x800 m maximum extent of the processed UAV images. GCPs stand for Ground Control Points.

Date	**Number of Pixels**	**Number of Images**	**Number of GCPs**
2014 – 04 - 10	325.532	955	28
2014 – 10 - 28	323.079	679	32
2015 – 04 - 21	391.734	1391	39
2016 – 04 - 01	336.164	1236	33
2016 – 11 - 03	306.824	unknown	unknown
2017 – 03 - 15	344.555	unknown	unknown

Firstly, the UAV-imagery was present for only the Zuid-Kennemerland study area. Spatially, the images were present for a limited maximum extent of 500x800 m (Figure 3-9A; Figure A-1). This area only comprised of part of the beach and the excavated blowouts. A small inland dune slack was filled with water but diminished in size over time (Figure A-1). Moreover, not everywhere within the image extent the UAV had taken images (Figure 3-9B; Table 3-1). Temporally, there were six UAV images available between 2014 and 2017 (Table 3-1). The UAV used was a fixed-wing Easystar I, supplied with a 12.1 Megapixel Canon Powershot D10. The imagery was gathered in the three bands of the visible spectrum: red, green and blue light (Figure 3-6). For each of the UAV surveys, 700 to 1400 single images were taken. These images were aggregated together in the SfM-MvS workflow contained in AgiSoft Photoscan®Professional Edition. Using ground-control points, the UAV images were georeferenced. The images were processed to a spatial resolution of 1 m and referenced to the RD coordinate system (EPSG:28992) within ArcMap 10.6. Thereafter, images were uploaded to the Google Earth Engine. For a more detailed description of the UAV data, the reader is referred to Ruessink et al. (2018).

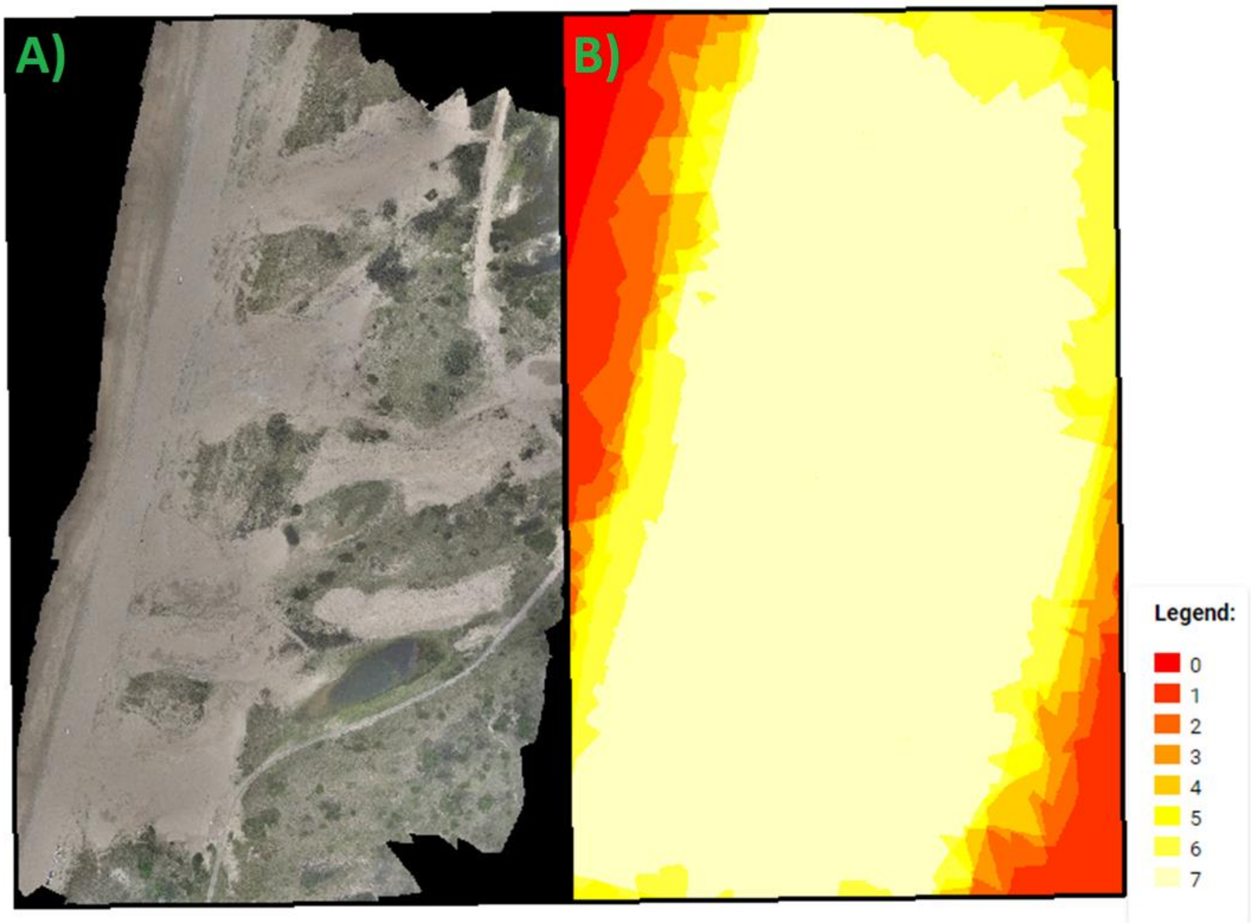

Figure 3-9; A) UAV image taken at 10th of April, 2014) and B) a heatmap of available pixels for the UAV imagery. The numbers indicate the number of valid pixel observation (0 is no observation, 7 means all UAV images covered the area). Figure A-1 in Appendix G shows the other 6 UAV images.

4 Study sites and Methodology

A major problem of classification of remote sensing images in coastal dunes is that pixels may consist of both dune vegetation and sand (Foody et al., 2005; Hugenholtz et al., 2012). Subsequently, binary classification of pixels will result in under or overestimation of either sand or vegetation. A popular method to decompose a spectral signal into sub-pixel fractional cover is Linear Spectral Unmixing (LSU). LSU assumes that every pixel is a linear combination of the spectral signature of all objects within that pixel, weighted by their spatial abundance (Keshava and Mustard, 2002). The distinct objects contribute both to the spectral signal which can be decomposed based on their individual spectral signature, or so-called *endmember*. The fraction within the pixel they appear is called *fractional abundance* (Keshava and Mustard, 2002). The two required steps for LSU involve the determination of endmembers and the inversion of the mixed pixels into the fractional abundance (Van Der Meer, 1999; Keshava and Mustard, 2002). Extraction of the endmembers was done on image-based spectral properties of a set of pixels best representing pure single features (Keshava and Mustard, 2002).

In this chapter, the first section describes the study sites and the Region of Interest (ROI) in which the endmembers were defined. Secondly, the pre-processing of the satellite imagery and filtering of images with presumed cloud cover is discussed. The following three section consecutively describe the subtraction of the endmembers by delimiting the ROI using 1) spectral indices, 2) local thresholding and edge detection and, 3) local maxima of an image histogram. Then, application of the LSU model is explained. Accordingly, the blowouts are subtracted by the pixels representing fractional cover of sand. Within the blowouts, a proxy for the vegetation cover is estimated using the Normalized Difference Vegetation Index (NDVI). Lastly, the classification of the reference UAV images is described and the comparison with the satellite imagery is explained. A flowchart of the process with the corresponding section numbers is presented in Figure 4-1.

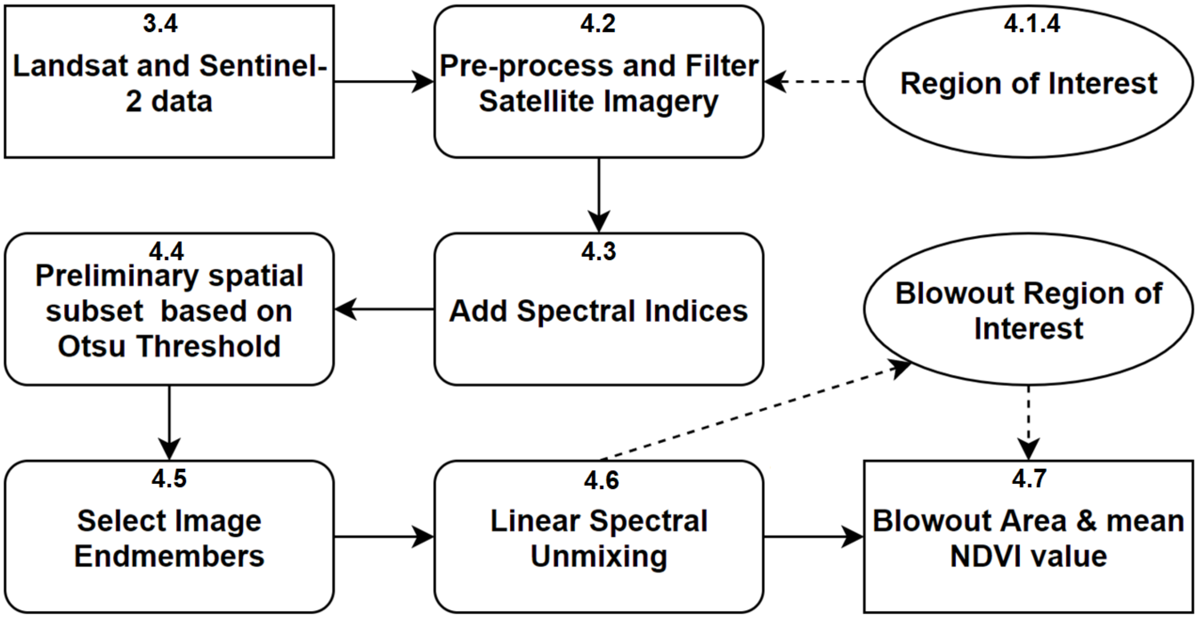

Figure 4-1; Simplified flowchart of the methodology to extract the blowout area and mean NDVI value from the Landsat and Sentinel-2 imagery. Numbers in the top of the boxes refer to the section where the process is described.

4.1 Study Sites

In this research, three blowout systems will be analyzed for their multi-decadal development. The excavated foredune notches in Zuid-Kennemerland (Netherlands) will be used as validation since there are multiple high-resolution UAV images available. Besides, blowouts at Padre Island (USA) and near the village Haurvig (Denmark) will be monitored. The study sites are presented in Figure 4-2. The description of each study sites focusses on the natural processes and development of the area. Lastly, the definition of the Region of Interest (ROI) is given.

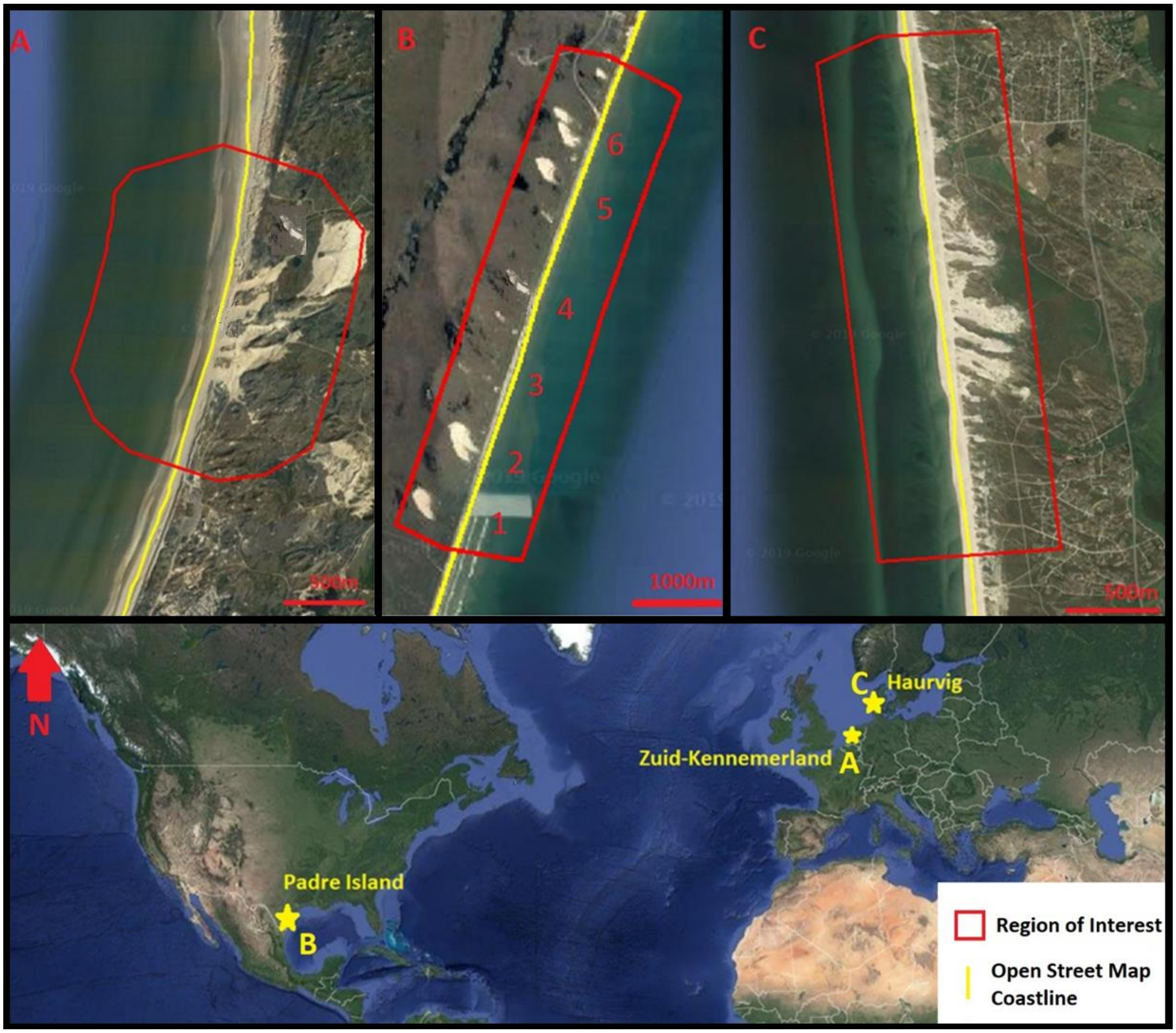

Figure 4-2; Study areas and their corresponding locations with A) Zuid-Kennemerland, B) Padre Island, and C) Haurvig. The blowouts at Zuid-Kennemerland and Haurvig are studied as one system, while at Padre Island the spacing between the single blowouts allowed for independent study and thus numbering of the blowouts.

4.1.1 Zuid-Kennemerland (Netherlands)

In Zuid-Kennemerland, five foredune notches were excavated in the winter of 2012–2013 in the foredune and resemble trough blowouts. The notches were excavated as part of a proposed management strategy to bring back aeolian dynamics to the backdunes and import sand to keep up with sea level rise. The excavation was performed on an 850 m alongshore stretch in foredunes of 20 m high. Each individual notch had a width of 50-100 m, a cross-shore length of 100-200 m and depth of 9-12.5 m (Kuipers, 2014; Ruessink et al., 2018). Moreover, two parabolic dunes were re-activated land inward of the excavated notches by removing the vegetation and they connected within two years with the excavated notches. Minor interventions where conducted to increase the potential aeolian transport, such as removing marram grass from the entrance near the beach and removing concrete blocks that came above surface due to erosion (Arens et al., 2015). The foredune blowouts were excavated in such a manner that overwash by storm surges was not expected. An overview of the area before, shortly after and 5 years after excavation can be found in Figure 4-2.

Figure 4-3; Development of the Zuid-Kennemerland study site from the begin of 2013 to mid-2017. Imagery from Google Earth.

Prior to the excavation, the foredune at Zuid-Kennemerland was overgrown with the European marram grass (*Ammophila arenaria*) and, due to coastal dune management concentrating on the stabilization and fixation of the foredune, resembled an alongshore uniform sand dyke (de Ruig and Hillen, 1997; Ruessink et al., 2018). In the pre-excavation situation, the foredune was characterized by gradual progradation, as sand deposited at the seaward side of the foredune with an average rate of about 27 m^3/m/year (Ruessink et al., 2018). The interesting development of the area from an established, stabilized foredune to an active aeolian coastal dune area, combined with the available high-resolution UAV data makes this area a perfect reference study site for the proposed methodology (Figure 4-3).

Oblique winds from the south-west between 45 and 75° relative to the shoreline are the most frequent and strongest and can exceed 12 m/s (Ruessink et al., 2018). Winds from the northwest can also be strong (> 12 m/s) and are related to stormy conditions along the Dutch coast, with high (>5 m) waves and dune scarping as a result (De Winter et al., 2015). The wind rose in Figure 4-4 shows the pattern for the typical wind regime at the Zuid-Kennemerland study site, which was measured at the entrance of the port of IJmuiden, 4 km north of the study site. Generally, wind speeds are higher from November till March, while the summer months are characterized by lower wind speeds and less frequent stormy conditions (Figure A-9).

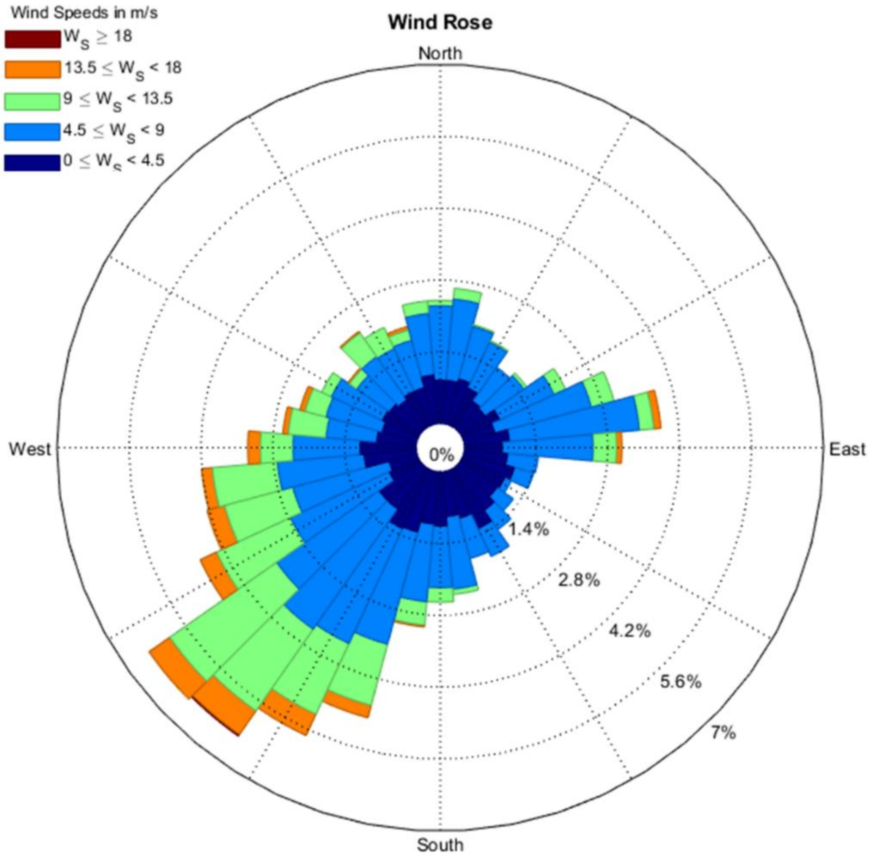

Figure 4-4; Windrose from 1 January 2013 till 2 October 2019 using daily mean wind direction and speed from the IJmuiden weather station located 4 km north of the study area. The large fraction of easterly winds is believed to be a local phenomenon on due to the east-west orientated Noordzeekanaal located landward of the wind station(Ruessink et al., 2018). Data obtained from the KNMI.

4.1.2 Padre Island (USA, Texas)

Padre Island is a barrier Island along the USA coast on the western side of the coast of the Gulf of Mexico. The seaward side of the island is characterized by a dissipative shoreface regime, having multiple bars and a wide and low angle beach profile (Wright and Short, 1984; Houser and Mathew, 2011). The Gulf of Mexico typically has a micro-tidal regime, with a diurnal tidal range of about 0.5 m and is wave-dominated with a significant wave height of about 1 m (Taylor et al., 2015; Ojeda et al., 2017). Measurements of maximum wave heights going up to 27 m during hurricane Ivan highlight the importance of extreme wave events (Wang and Briggs, 2015). Along the Padre Island, foredune are on average 3.4 m (±0.6 m) high, consist of two to three ridges and are mostly densely vegetated with grass (Taylor et al., 2015). Along the coast, multiple blowouts are found with a throat width from the beach between 25 and 60 m. The more inland parts of the blowouts have widths up to 200 m. The cross-shore length of the blowout was found between 140 and 430 m (Jewell et al., 2014). The blowouts migrated land inward (northwest) at a rate of 45 m y^{-1} to 150 m y^{-1} (Jewell et al., 2014).

The climate in along the Texas coast is characterized by hot (over 30 degrees Celsius) summers and it is arid almost year-round (Figure A-11). Only during fall (September and October), the rainfall on average exceeds 100 mm per month (Figure A-11). Furthermore, rainfall in May is typically higher due to heavy rainfall event of less than a few days (Kocurek et al., 1992). Easterly winds are the most common winds blowing inland form the Gulf of Mexico in this region, while the strongest winds tend to come from the south east to south (Figure 4-5). Wind speeds show a seasonal pattern with higher, south easterly dominated winds during the spring and summer, while calmer winds come from the east during the fall and winter (Kocurek et al., 1992). The hurricane season is generally assigned to June till November. Washovers of the dunes may occur during extreme storms and hurricanes. Hurricanes hitting this part of the coast were for example in 1970 (Celia), 1980 (Allen), 1983 (Alicia and Barry), 1999 (Bret) and 2008 (Ike and Dolly) (Jewell et al., 2014; Taylor et al., 2015).

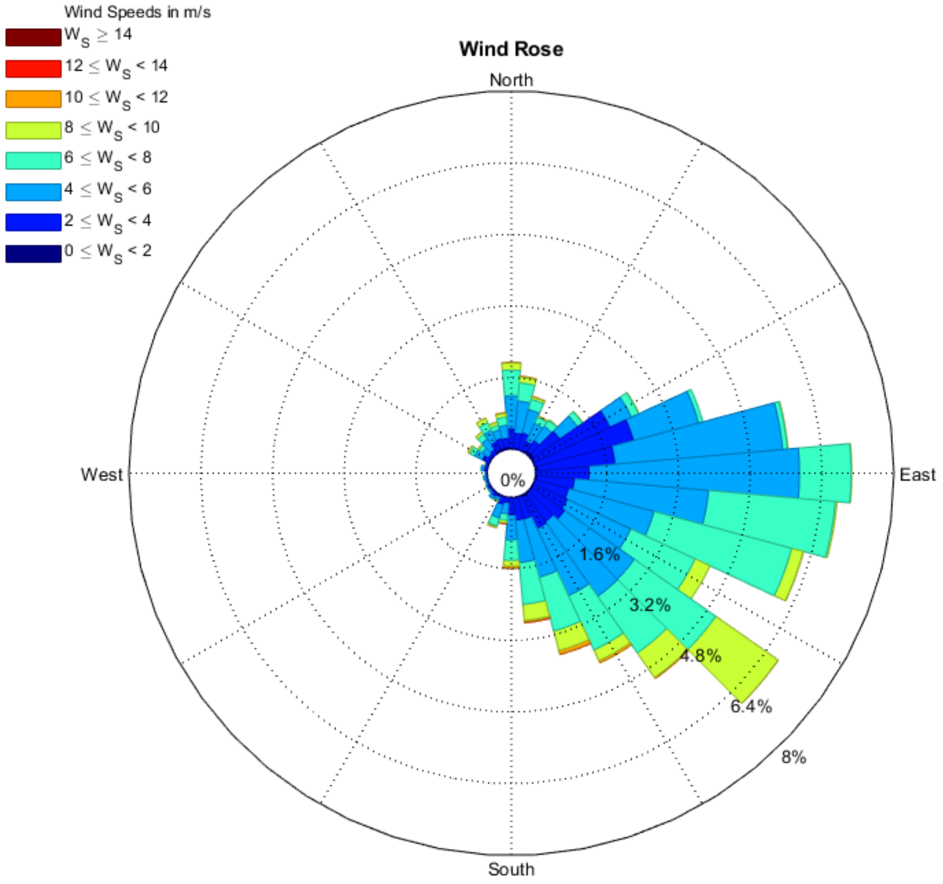

Figure 4-5; Wind Rose for the wind data at Corpus Cristi of data from the Corpus Cristi N.A.S. Airport weather station. Major data gaps were present in 1998-2000 and 2002-2006.The dominant fraction of wind from the east and southeast is a result from the onshore dominant winds from the Gulf of Mexico. See for the timeseries of wind speed Figure A-10.

Up to 1968, the island was used for cattle grazing. In the first decades after 1968, vegetation growth increased and the dunes stabilized. Later, driving on the beach reverted that process and the dune significantly destabilized near the access road in the north of the study site (Houser and Mathew, 2011;

Jewell et al., 2014). Currently, it is a protected area named Padre Island National Seashore (Weise and White, 1980; Jewell et al., 2017). Visual inspection of the available Landsat imagery between 1984 and 2020 revealed that 6 blowouts qualified for this analysis. Two blowouts were assessed in more detail (namely, number 1 and 4, Figure 4-2), of which the northern one is still active and the southern one is stabilized (Jewell et al., 2017). In combination with the other four blowouts, this study area could provide valuable insights for the development of blowouts on longer timescales as the blowouts 1) could be tracked on a single basis due to sufficient spatial distance between each other and 2) were shown to both initiate and close within the temporal range of available satellite imagery time (Jewell et al., 2014).

4.1.3 Haurvig (Denmark)

Between the little vacation resorts Haurvig and Skodbjerge, along the narrow spit Holmsland Tange on the western coast of Denmark sit a series of consecutive blowouts (Figure 4-2). The coastline is almost north-south orientated, with a cross-shore angle of about 264° degrees. The beach has an average width of 150 m and a gentle slope of 0.006° (Brinkkemper et al., 2017). The foredunes have a steep seaward slope and are between 12 and 18 m high. A relative small tidal range off less than 1 m make the region a wave-dominated environment (Earnshaw et al., 2014). The significant yearly wave height is 1.4 m with a mean wave period of 4-5 s (Brinkkemper et al., 2017). South to north westerly wind are dominant (Cappelen and Jørgensen, 1999). Northwesterly winds are dominant in the summer period from May to September, while wind directions are more variable during the winter.

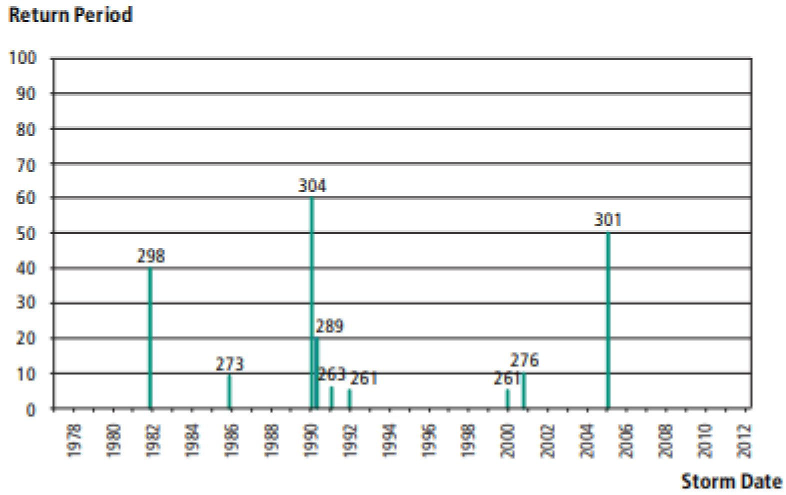

Figure 4-6; High water levels with a return period of over 5 years observed at the port of Hvide Sande (Earnshaw et al., 2014).

During storms with strong westerly winds, wind speeds maximizes up to 34 m/s. With a 100-year return period, storm surges of 3.19 m and the maximum significant wave height waves of up to 7.5 m are observed (Earnshaw et al., 2014). These storms scarp the dune foot and cause an annual coast line retreat up to 8 m, although this is managed by local beach and shoreface nourishments (Earnshaw et al., 2014). In the port of Hvide Sande, 9 km north of the Haurvig blowout study area study, water level measurements were obtained from 1977 till 2012 by the Danish government (Earnshaw and Madsen, 2013). Storms with a return period of higher than 5 years were identified and presented with their according high-water level (Figure 4-6). Major storms are related to erosion of the foredune, which characterize the North Sea Danish coast (Figure 4-7), although their impact vary enormously on a local scale from 0 up to 50 meters of dune erosion (Earnshaw and Madsen, 2013).

Figure 4-7; Major dunefront erosion and a local breach is observed after a storm in the winter of 2006-2007. Photo taken at Skodbjerge at January 7 2007 (Thomsen et al., 2018).

At the western Danish coast between Lodbjerg and Nymindegab, coastal dune management is deployed since 1982 (Rivero et al., 2018). Here, the dune management in and surrounding the Haurvig study area will be discussed. At Haruvig, there is a natural retreat of the coastline of ±2 m/year, while the maximum allowable retreat is aimed at 1 m/year (Thomsen et al., 2018). In this area, four types of measures are applied and denoted chronologically (Thomsen et al., 2018). From 1986 till 1994, dune enhancement was applied. This comprised of increasing the backdune strength by nourishing sediment land inward of the foredune 1 km south of the blowouts. This caused leeward side of the dunes to develop into a plateau. From 1989 till 2001, beach scraping occurred, which was aimed at distributing sediment at the berm more evenly alongshore using heavy machinery. In 1996, 2000 and 2001, these measures were partly deployed in front of the trough blowouts. Nourishments were done on the beach just south of the area in 1992 and 1994, while in 1999 the nourishment span alongshore in front of the trough blowouts. This beach nourishment had a volume of 69 m^3/m and was finished on 28th of July 1999. In 2010, a large shoreface nourishment was applied with sediment from north of the Hvide Sande port till 12 km south, with a volume representing 57 m^3/m. In 2011, another shoreface nourishment supplied sand 2 km south of the area.

4.1.4 Definition of the Region of Interest

The blowouts studies are in the first dune ridge, for which is was likely that the study areas consist of dune vegetation, sand and water. For the deduced methodology, it was important that the Region of Interest (ROI) included a similar size of the land and water, while excluded most of the background features (such as roads and human settlements or backdune successive vegetation species). Accordingly, the region required for this analysis would preferably a linear stretch along the coastline. The coastline was obtained from the OpenStreetMap Coastline (OSMC) (OpenStreetMap®). This vector data represented the coastline was downloaded as present in May 2019 and uploaded as shapefile in WGS84 projection to the Google Earth Engine. The advantages of this dataset were that it was free to use, shown to be accurate (Donchyts et al., 2016) and split up into multiple line segments such that it was fast an easy in use. An inadequacy of this method was that if the waterline showed significant changes over the period of interest, application of the OSMC method became unfeasible. Visual inspection did not reveal large changes in the waterline over the 10 to 40-year study period that the OSMC of 2019 was unfeasible to use.

The ROI was defined semi-manually as a linear rectangle around the coastline. The ROI was constructed with an alongshore length (m) and a cross-shore length (m) for each study site. The cross-shore length was the distance at either side of the OSMC and should comprise sufficient parts of the foredune blowouts and the surrounding vegetation to subtract relevant endmember spectra for the dune vegetation and blowout sand. Accordingly, the cross-shore length was defined as 750 m (Zuid-Kennemerland and Padre Island) and 500 m (Haurvig). The alongshore length was the distance along the OSMC in front of the blowouts, defined as 1000 m (Zuid-Kennemerland), 1500 m (Haurvig) and 3000 m (Padre Island). The ROI are presented in Figure 4-2.

4.2 Pre-processing the satellite imagery

Depending on the location multiple observations per day might be available when the ROI is located in the overlap between consecutive rows (Landsat) or granules (Sentinel-2). Observations from the same date and platform were mosaiced together using a mean composite. These composites will be referred to as images. To reduce computation time, scenes with an estimated cloud cover above 90 percent were removed. The scene-wide cloud cover assessment was provided by the data providers, which was aggregated using the mean if multiple images were mosaicked. Also, if the images did not cover the complete ROI, they were removed from the analysis. Then, images with presumed cloud or cloud shadow contamination were removed. Lastly, Landsat-7 images obtained with the failed Scan-Line-Corrector after May 2003 were filled using the timeseries. A flowchart of the pre-processing of the satellite imagery is presented in Figure 4-8.

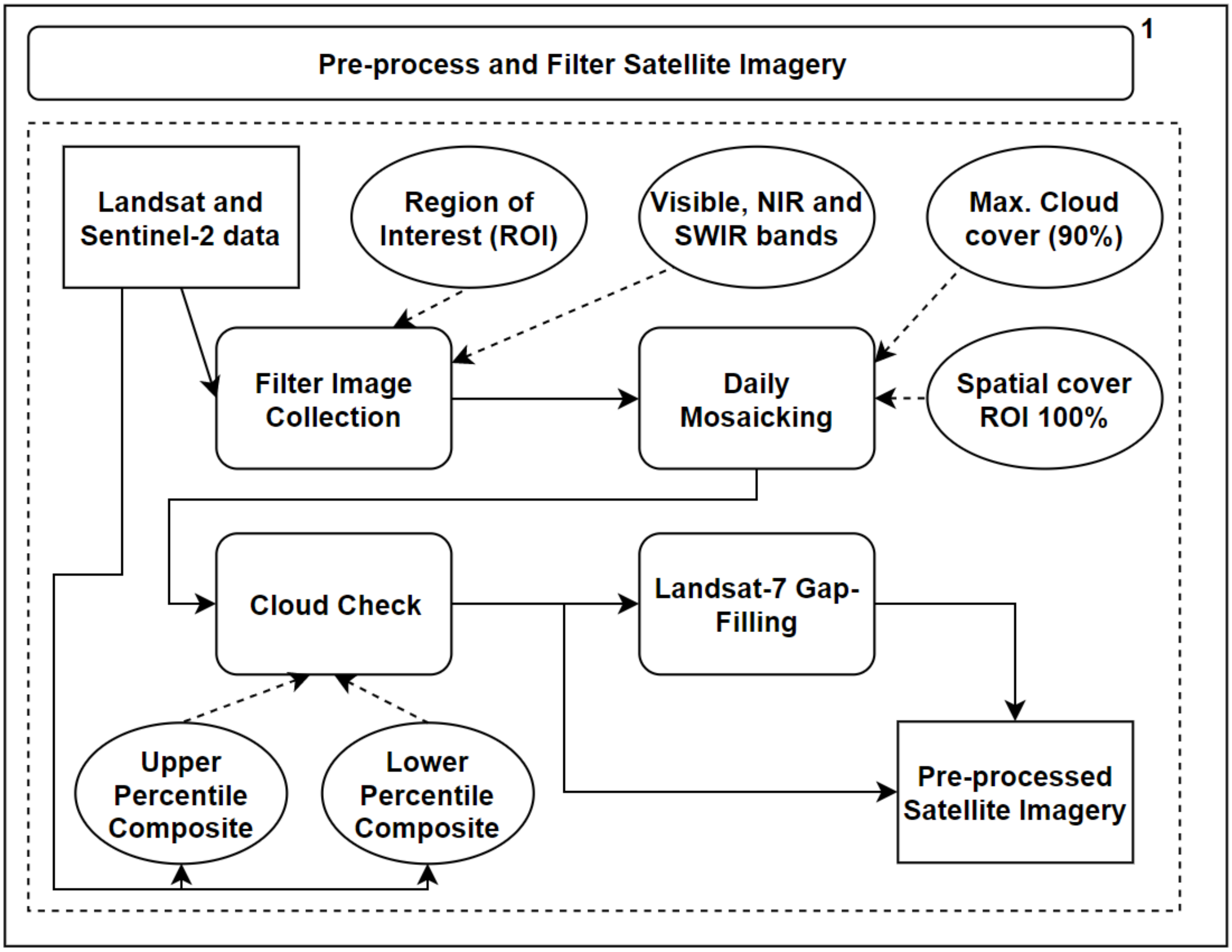

Figure 4-8; Flowchart of the pre-processing of the Landsat and Sentinel-2 datasets. Note that this flowchart zooms in on box 4.2 "Pre-process and Filter Satellite Imagery" of Figure 4-1.

4.2.1 Filter image collection

In spaceborne spectral satellite imagery, clouds and cloud shadows are the major disturbance of the spectral signal detected by the sensor (Van der Meer and De Jong, 2011; Donchyts et al., 2016). Therefore, cloud cover assessment and masking are a major discussed topic in the processing of satellite imagery.

For this analysis, cloud or cloud shadow containing images required to be removed from the analysis a priori. Firstly, a simple filter of the collection based on the metadata was done. Then, a pixel-based timeseries analysis was performed to remove images which were likely to contain clouds or cloud shadows within the ROI.

Generally, there are two common approaches of dealing with clouds: 1) per pixel cloud likelihood algorithms, and 2) use a timeseries to select only cloud-free pixels. Firstly, per pixel cloud detectors use either the spectral properties of clouds and cloud shadows, or use machine learning algorithms using supervised classifications techniques with accompanying training data (Zhu, 2017). Moreover, cloud cover algorithms such as CFMask label pixels in each scene using statistics of the whole scene, while in this research the ROI is much smaller (about 3x1 km) than the actual size of a single scene. Although there is a large amount of cloud detection algorithms developed, no satisfactory algorithm has been made to detect clouds and cloud shadows at pixel level (Zhu, 2017). Secondly, noise by clouds and cloud shadows can be removed by reducing a timeseries of images to a per pixel statistically chosen value, such as the median, medoid or Best-Available-Pixel composites (Potapov et al., 2012; Flood, 2013; Griffiths et al., 2013; White et al., 2014; Hermosilla et al., 2015). Although these methods are very effective in the removal of cloud and shadow noise, it drastically reduces the temporal resolution. Namely, these so-called composite images result in a single pixel observation over a user-defined period.

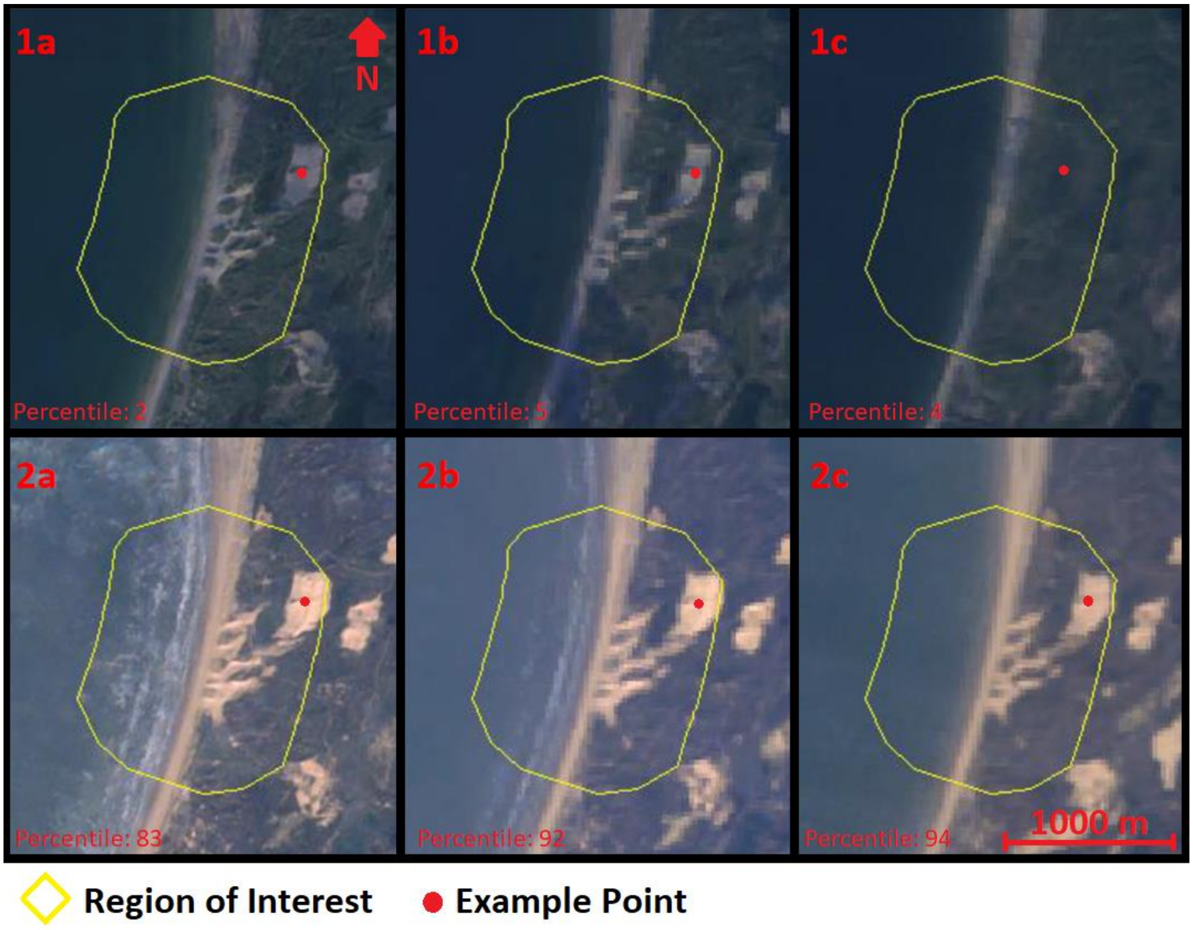

Figure 4-9; True colour composite images of the 1) lower and 2) upper percentile for the a) Sentinel-2 collection, b) the Landsat 8 collection and c) the Landsat 5 and 7 collections used for the Zuid-Kennemerland study site. The percentile values used are indicated in the lower left corner. See for the Padre Island and Haurvig study Figure A-2 and Figure A-3.

The previous two common ways of dealing with clouds in satellite imagery did not stratify for this research. Accordingly, a different cloud and cloud shadow removal approach was developed. It was built upon the idea that the reflectance of the earth's surface fluctuates naturally, which allows local distortion of clouds and cloud shadows to be distinguished. The natural reflectance value from the earth's surface was obtained by reducing the image collection to a pixel-wise lower- or upper percentile value. These values were chosen based on the visual interpretation, such that it was the lowest (highest) value before cloud shadows (clouds) became present within the ROI (Figure 4-9). The image collections for the percentile reducers were made of the images with an estimated cloud cover lower than 20%. These collections were created for each study area and per spectrally similar satellite, namely 1) Landsat 4, 5 and 7, 2) Landsat 8 and, 3) Sentinel-2. The first three satellites can safely be aggregated together (Teillet et al., 2001): their visible, NIR and SWIR bands have similar spectral resolution (Figure 3-6) and the imagery temporally overlaps (Figure 3-7).

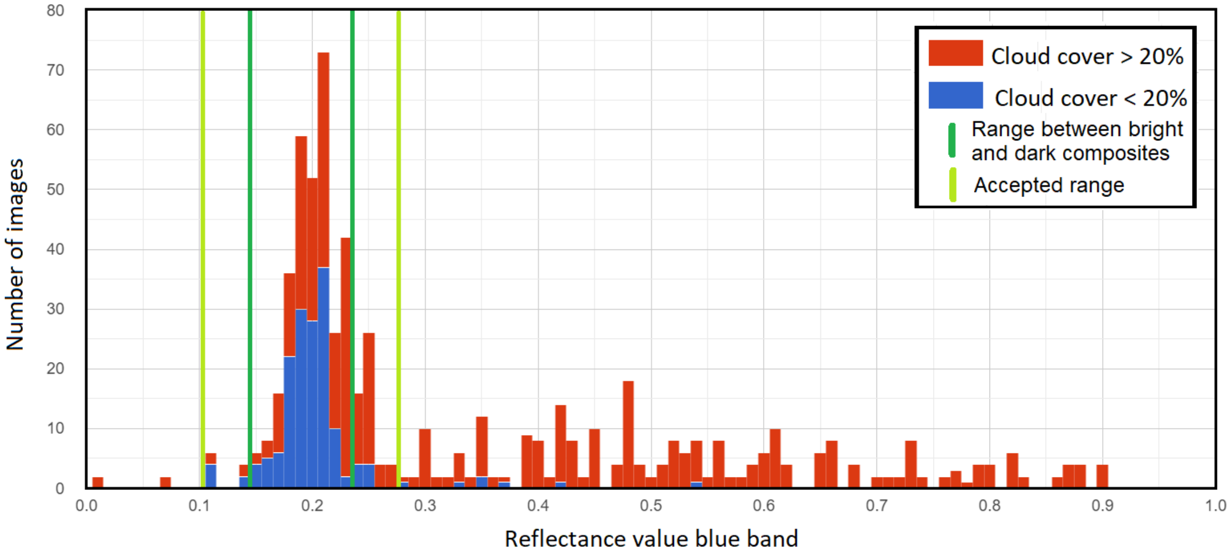

Figure 4-10; Histogram of the blue band values over the Sentinel-2 image collection at Zuid-Kennemerland for a single pixel in a sandy area (red dot Figure 4-9). The collection was split up into images with an estimated scene cloud cover of lower than 20% (blue) and higher than 20% (red). The dark green line indicates the lower (3) and upper (83) percentile values from the reduced collection of images. The light green lines indicate the range of accepted reflectance values. See for code: B-2.

The brightest and darkest composite images were made for the visible (blue, green and red), NIR and SWIR (swir1 and swir2) bands using standard percentile reducer functionality available in the GEE. The corresponding reflectance values, with an accepted range of half the difference between the upper and lower value, of the composite images were used as indication for the natural fluctuations of the earth's surface. For each band and all pixels within the ROI, the image reflectance was compared against the values of the accepted range (Figure 4-10). Then, the images were selected when their pixels were within the accepted range of reflectance values. Table 4-1 gives an overview of the number of scenes passing the cloud cover check.

Table 4-1; Overview of Landsat and Sentinel-2 scenes included in the research. The column 'section' refers to the sections where the explanation for the filter can be found. See for code: B-3

	Zuid-Kennemerland		**Padre Island**		**Haurvig**		**Section**
	images	**percentage**	**images**	**percentage**	**images**	**percentage**	
Total Images	787	100	1,098	100	1,339	100	3.4
Clouds < 90%	688	87	1,027	94	1,158	86	4.2
Cloud Check	327	42	712	65	576	43	4.2.1
Canny Edges	317	40	711	65	564	42	4.4.4
Final Size	315	40	707	64	560	42	-

4.2.2 Landsat-7 gap-filling

The Scan-Line-Corrector (SLC) of the Landsat 7 ETM+ sensor failed on May 31 2003, resulting in missing stripes of pixels increasing in width away from the scene center passing location (Figure 3-8). Unfortunately, none of the study areas was located exactly in the center line of a Landsat 7 scene, thus the SLC failure affected the cover of the study area by Landsat 7 imagery after May 2003. The cover reduced to 75% (Zuid-Kennemerland), 79% (Haurvig) and 88% (Padre Island). The differences can be related to the distance from the scene center line. The Landsat 7 collection was the only imagery between the decommission of Landsat 5 and the launch of Landsat 8 satellites and thus it was an essential part of the dataset.

Spectrally similar imagery from another date is required to fill the missing pixels of Landsat 7 scenes (Yin et al., 2017). Fortunately, the Landsat 7 SLC produced gaps in the imagery at different spatial location each time it passed the same orbit. Moreover, the Landsat 5 TM sensor produced spectrally similar data (Figure 3-6; Teillet et al., 2001) thus was used additionally to fill missing pixels (Yin et al., 2017). Missing pixels could simply be filled with the closest valid observation (i.e. this step was done after the cloud (shadow) image validation). An example of a gap-filled scene is illustrated in Figure 4-11.

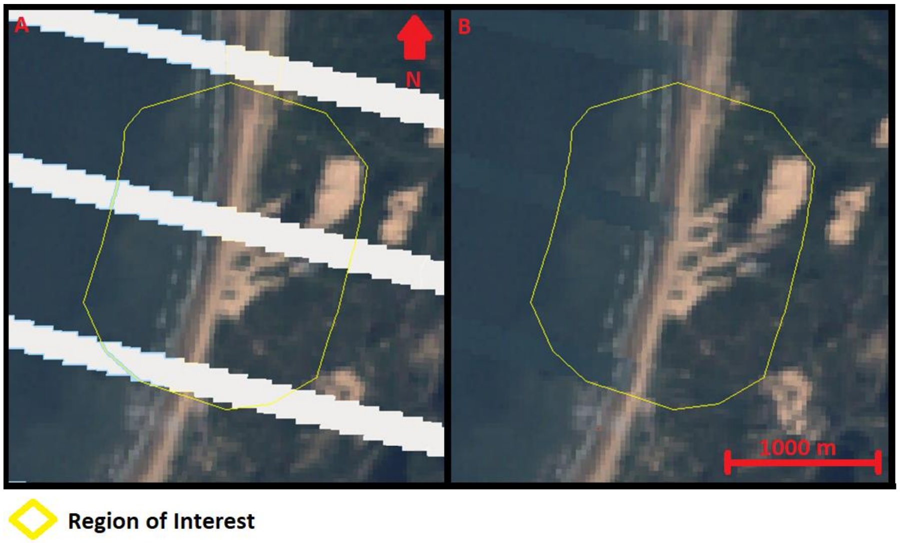

Figure 4-11; Landsat 7 scene acquired for the Zuid-Kennemerland study site at 3 June 2016, with A) the original scene in true colour, and B) the gap-filled image with the temporal closest image of Landsat 7 taken at 12 June 2016 in true colour. See for code: B-4

4.3 Spectral indices

In remote sensing, the detection of ground features suffers from the interference of radiation by the atmosphere and the background. For example, if a turbid river flows into a lake, the spectral signal becomes a mixture of water and turbidity varying over the lake, while it represents the same land cover feature ‘water’. Moreover, molecules in the atmosphere interfere with the ground signal to detect. Consequently, single band signals are dependent on the image-specific atmospheric conditions and region-specific variation of the background features.

To overcome this, the ratio or difference between two wavelengths can be used. With this approach, the radiation at one wavelength is normalized by the radiation in another wavelength. Consequently, when the difference between two wavelengths is taken, any noise or background feature can be eliminated (Rouse Jr et al., 1973; Demetriades-Shah et al., 1990). As such, the use of the non-atmospheric corrected imagery is acceptable. This ratio is often referred to as a normalized difference index (McFeeters, 1996; Gao, 1996; Elmore et al., 2000). In this report, the ratio between two bands will be referred to as an ‘index band’.

4.3.1 Water index

Spectrally, there is a significant difference between the reflectance from land and clear water pixels, especially in the infrared region (Fisher et al., 2016). In the past, a substantial amount of indices has been developed for remote sensing imagery (Ji et al., 2009; Fisher et al., 2016). For example, the Normalized Difference Water Index (NDWI) and the Modified Normalized Difference Water Index use the normalized difference between green and infrared bands (McFeeters, 1996; Xu, 2006). Other water indices use a larger mixture of bands, such as the Tasseled Cap Wetness (Crist, 1985), Water Index 2006 (Danaher and Collett, 2006) or Water Index 2015 (Fisher et al., 2016). The latter three water indices include several constant multiplication values and thus apply to only a selected dataset, geographic location and a certain processing level of the satellite imagery.

A major difficulty in the detection of water can be related to water mixing with suspended sediments (Ryu et al., 2002; Ji et al., 2009), which may be solved using regional local thresholds (Donchyts et al., 2016). However, suspended sediment concentrations in the study sites considered were found too low to consider the method by Donchyts et al. (2016) for an estimate of the coastline. Despite all efforts in developing new water indices, earlier studies on the use of a different water indices did not find any index to perform significantly better than another (Ji et al., 2009; Fisher et al., 2016). Accordingly, the common NDWI was used throughout this research. The NDWI is defined as

$$NDWI = \frac{(green - NIR)}{(green + NIR)} \tag{1}$$

where *green* and *NIR* refer to the bands that detects green or Near-Infrared light (McFeeters, 1996), depicted for the Sentinel-2 and Landsat sensors in Figure 3-6. This index band results in a value ranging from -1 to 1, where soil and terrestrial vegetation features usually have zero or negative values, as NIR is typically higher than green light. Water features generally have positive values (McFeeters, 1996).

4.3.2 Vegetation index

The detection of vegetation from spectral satellite imagery is generally based on that vegetation comprises of chlorophyll, which is the green pigment found in plants and essential for photosynthesis. The spectral signature of chlorophyll is characterized by the strong absorption at about 0.69 µm, while the absorption in the adjacent near-infrared region at about 0.85 µm is generally missing in healthy 'green' vegetation (Myneni et al., 1995). The result is a strong contrast between the signal captured at those two wavelengths, which can be used to construct an index for vegetation. Subsequently, the most common vegetation index is the Normalized Difference Vegetation Index (NDVI) (Myneni et al., 1995; Leprieur et al., 2000; Pettorelli et al., 2005; Robin et al., 2011) defined as

$$NDVI = \frac{(NIR - red)}{(NIR + red)} \tag{2}$$

where *NIR* represents reflectance in the visible wavelength (~0.6 µm) and *red* in the near-infrared wavelength (~0.8 µm) (Myneni et al., 1995; Carlson and Ripley, 1997). The NDVI should not be treated as a physical property of vegetation, although it is correlated to for example the fractional vegetation cover, vegetation condition and biomass (Carlson and Ripley, 1997). As such, changes in the NDVI value from remote sensing over time or space depicts the changes in the in the vegetation proportional to the change in the photosynthetically active radiation (Sellers, 1985; Chen et al., 2004). The NDVI is also applicable in the detection of bare soil from vegetation, as the reflectance in the *red* and *NIR* wavelengths for bare soil is approximately equal, resulting in lower NDVI values than the NDVI from vegetation (Huete, 1988). Moreover, the NDVI has shown to be effective in coastal dunes (Levin et al., 2006; Hugenholtz et al., 2012; Nolet et al., 2018) and is applicable to each satellite mission used without sensor or region specific calibration values.

4.4 Preliminary spatial subset of water, vegetation and sand

An estimate of the potential location of sand, water and foredune relevant vegetation was made to obtain Image Endmembers (IE). Firstly, the index bands were used two discriminate classes using a dynamic threshold. This was then used to estimate the land and water area. Thereafter, the land area was spatially delimited to include only a relevant subset of pixels around the estimated vegetation-sand border. Lastly, the preliminary spatial subset of unvegetated (sand) and vegetated area within the defined land area was assessed. A flowchart of this process is presented in Figure 4-12.

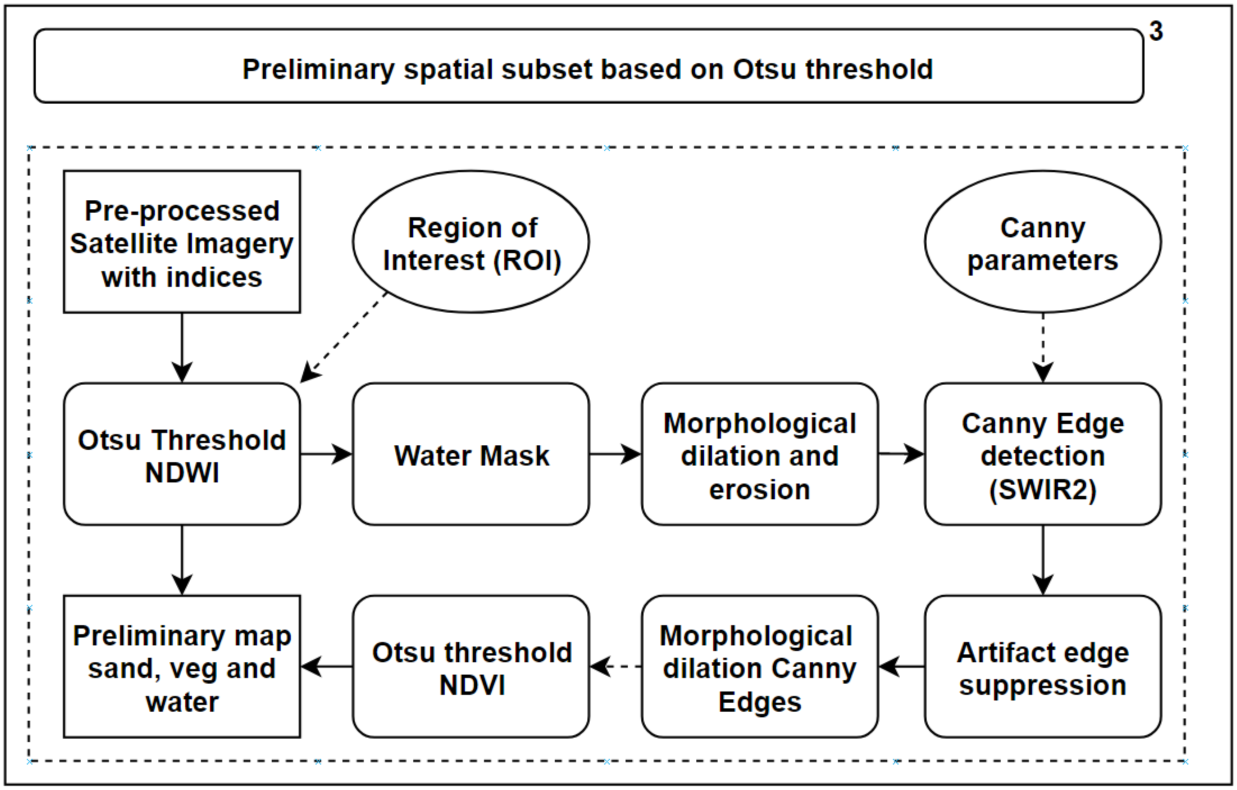

Figure 4-12; Flowchart for the process of converting the pre-processed satellite imagery into a binary map with a first indication for the spatial location of the three features, which is used to obtain the image specific endmembers. Note that this flowchart zooms in on box 4.4 "Preliminary spatial subset based on Otsu threshold" of Figure 4-1.

4.4.1 Otsu thresholding

The index bands NDWI and NDVI were used to classify an area in water or terrestrial, and sequentially the terrestrial in vegetated or non-vegetated. These indices normally have floating values between -1 and 1 (Tuxen et al., 2008; Ji et al., 2009; Torres-Sánchez et al., 2015; Donchyts et al., 2016), which are separated into two classes with a threshold. The threshold needed to be found dynamically considering the global application of the model. Consequently, a dynamic Otsu threshold was preferred over a global constant value (Ji et al., 2009; Donchyts et al., 2016). This threshold is based on a histogram and finds whatever partition of the data that maximizes inter-class variance. The Otsu method is optimal to find a per-image unsupervised and nonparametric threshold and above all is a fast-performing equation (Donchyts et al., 2016; Clinton, 2017). The threshold selection implied searching a value within the -1 to 1 range such that all values greater than the threshold were labelled class 1, while all the values below the threshold were labelled class 2 (Weszka, 1978). If there are two clear distinguishable objects in the index image, the histogram of the pixels will be bimodal (Kapur et al., 1985). In that case, a threshold can be defined at the bottom of the valley between the two peaks.

The Otsu threshold was successfully used to separate water bodies from background features (Li et al., 2013), although did not perform well separating small river streams (<6 pixels width) from the background (Yang et al., 2014). For a good performing Otsu threshold a similar number of samples for both classes is desired (Kapur et al., 1985; Donchyts et al., 2016; Clinton, 2017). In other words, successfully applying the Otsu threshold to segment two classes on a single band image required a near bimodal deviation of the dataset (Tobias and Seara, 2002). In nature, it is common that a selected area is overrepresented by a certain land feature compared to another. Then, the threshold value is shifted towards the larger lobe of the data (Tobias and Seara, 2002; Yang et al., 2014; Donchyts et al., 2016). A possible solution is to delimit the area of interest such that both classes are represented in near equal proportions. This potentially results in a better threshold value compared to a global one, as the input data is directed only to the most likely boundary between the two features of interest (Tobias and Seara, 2002; Yang et al., 2014; Donchyts et al., 2016).

4.4.2 Water and land masking

The Otsu threshold was calculated successfully for the ROI for the NDWI to get a first indication of the land and water area, as the ROI was defined such that water was theoretically present in near equal proportions as land features. The Otsu thresholding method was based on the fact that soil and terrestrial vegetation features usually have zero or negative values, as NIR is typically higher than green light, and water features generally have positive values (McFeeters, 1996). A frequency distribution of all pixel values in the ROI, further referred to as histogram, resulted in two distinct domains of pixel frequencies (Figure 4-13C and Figure A-4C). Water was represented by positive NDWI values, while land by negative NDWI values. The histogram had a flexible number of input pixels, as it depended on the size of the study area and the spatial resolution of the sensor. The standard application within the GEE of determining the number and size of the buckets of a histogram was unsatisfactory and not well documented. Consequently, the number of buckets was adapted based on the number of input pixels, which is described in appendix 0.

Generally, the Otsu threshold was sufficient to isolate the land features. Nevertheless, successful isolation of the land features was hindered by 1) relief-based shadows, 2) wave foam, and 3) the wet, intertidal beach. Shadows were detected as water due to its dark appearance. Wave foam was sometimes erroneously detected as land due to its bright nature, which is unlikely for water. The wet intertidal beach had a significant different spectral signature than the dry, sandy blowouts. Therefore, it was undesired in the further process to obtain relevant pixel spectra for the foredune blowouts. Consequently, the standalone Otsu threshold did not suffice for the complete collection as a standalone water mask. Accordingly, morphological dilation (30 m) was applied on the water mask by the Otsu threshold to remove the small patches of erroneously detected relief-based shadows. Sequentially, a morphological erosion was applied on the water mask to remove the possibly present intertidal beach and wave foam. The size of the erosional buffer was dependent on the approximate width of the beach. The buffer was set at 150 m for Zuid-Kennemerland, 60 m for Padre Island and 90 m for Haurvig. As such, the wet beach was excluded from the land classification (Figure 4-13E and Figure A-4DE). Figure A-5 illustrates an example where relief-based shadows were included and wave foam was excluded from the land classification using consecutive morphological dilation and erosion.

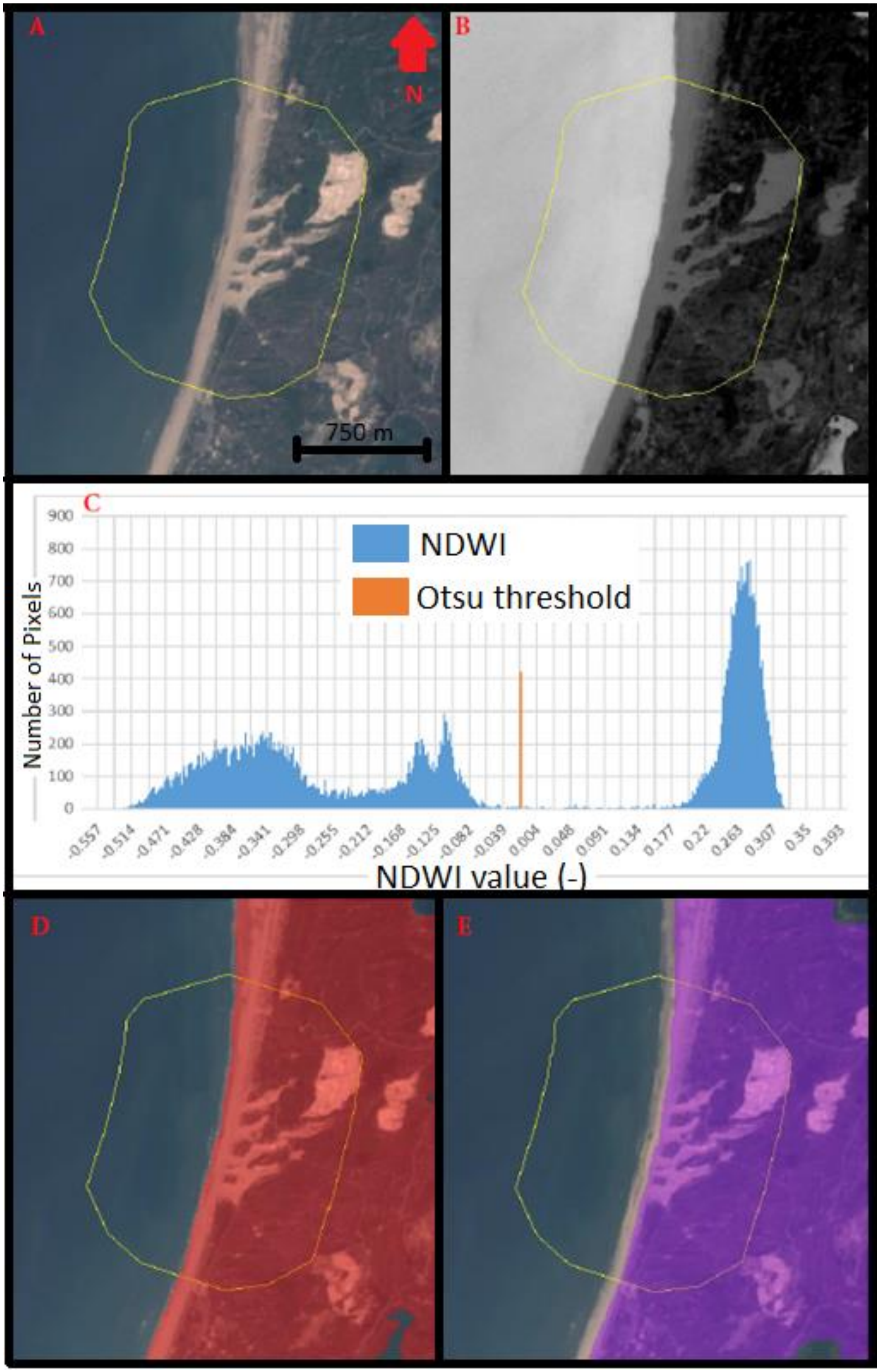

Figure 4-13; A) Sentinel-2A image at July 5 2017 in true colour, B) the calculated NDWI according to equation 1, C) a frequency distribution of the NDWI values and the corresponding Otsu threshold (-0.017), D) water mask based on the Otsu threshold and E) final water mask using the morphological dilation and erosion. The ROI is indicated by the thin yellow line. See code: B-8.

4.4.3 Vegetation and sand masking

The ROI was defined such that near equal proportions of water and land were present. This permitted the Otsu threshold to be implemented correctly on a bimodal deviation of two classes. On the other hand, the area of the blowouts and beach (sand area) in comparison to the dune vegetation was a priori not known, and, as it was the object of study, expected to be variable over time. Moreover, a clear spatial succession of vegetation on the foredunes is generally found. Thus, including all pixels of the ROI could include an uneven distribution of pixels representing sand or vegetation. Also, more types of vegetation than those which are representative for the vegetation along the boundary of the blowouts and vegetated foredunes might be included. Therefore, the land area within the ROI had to be spatially delimited to the transition between the blowouts and the vegetation. This was done following the edge detection method of Donchyts (2018).

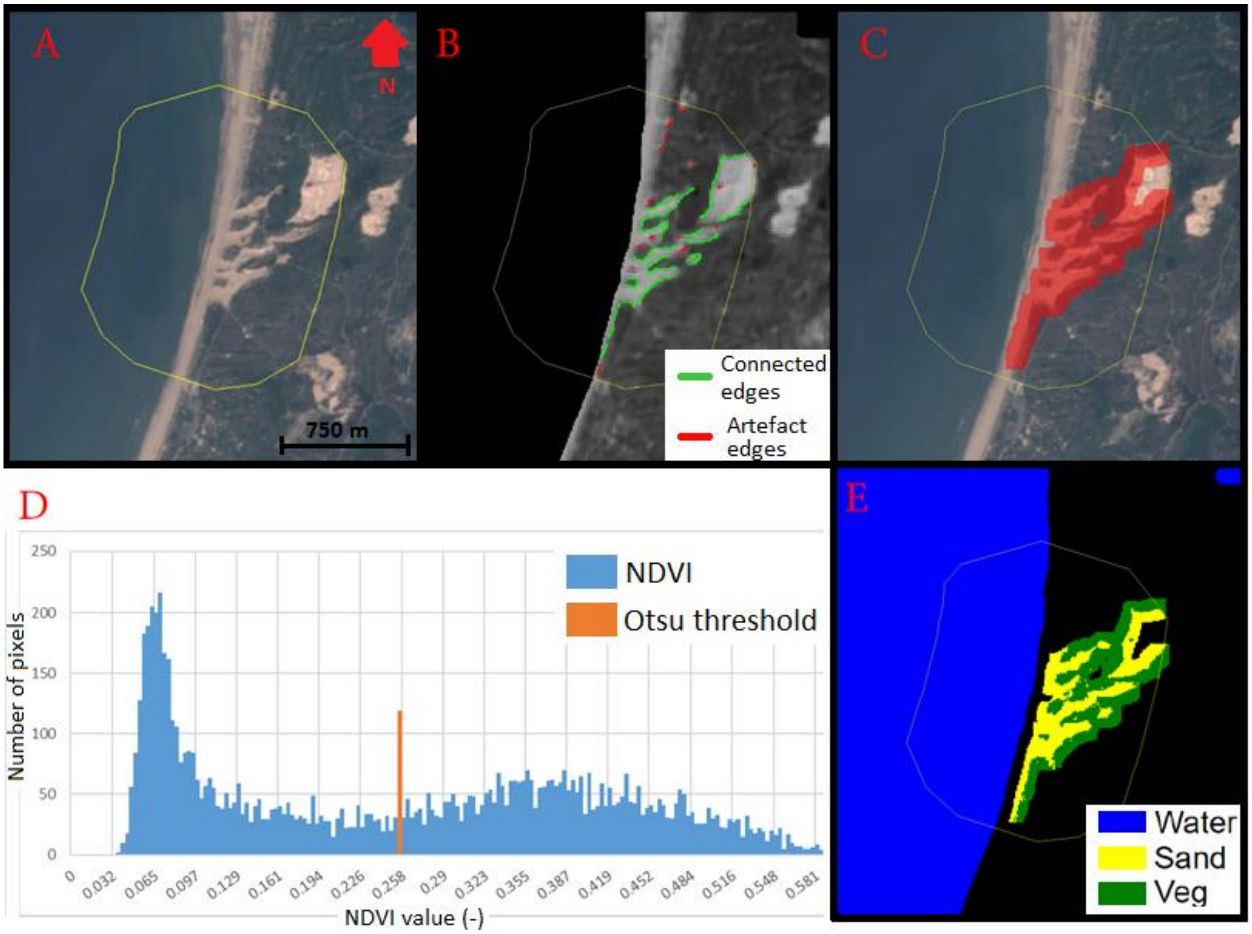

Figure 4-14; A) Sentinel-2A image at July 5 2017 in true colour, B) grey-scale SWIR2 image with connected Canny edges (>10 pixels) and artefact edges (<10 pixels), C) true colour image with morphological dilation of 60 m around the connected segments of edges in shaded red, D) histogram of NDVI values with the Otsu threshold (0.255), E) preliminary binary map based on the NDVI and NDWI Otsu threshold. The ROI is indicated by the thin yellow line. See code: B-9.

Edge detection methods can be used to indicate the area where a change in spectral signal is observed (Maini and Aggarwal, 2008). A popular method to detect edges in images is the Canny edge detection. The Canny edge method allows for edge detection with a low error rate and suppresses image noise to be detected as an edge (Canny, 1986; Maini and Aggarwal, 2008; Donchyts, 2018). Canny edge detection is performed using 1) a single band image, 2) a sigma value and 3) a threshold value. On the one hand, the adjustable sigma and threshold parameters are the strength of the Canny edge detection method to operate in all kind of imagery (Canny, 1986; Maini and Aggarwal, 2008), though these parameters generally have to be found empirically (Canny, 1986; Donchyts, 2018).

Firstly, the single band image is any single band image on which there are relevant spectral changes are expected. This can be a band directly observed by the sensor or any index band calculated from a combination of bands. The transition between sandy and vegetated areas was characterized by a change in spectral signature, as it was expected that pixels with vegetation reflected a different spectral signature than pixels representing sand (Figure 3-3). The Canny edge detection was applied using the Short-Wave-Infrared band (2.1-2.3 µm). This band has generally been found to represent the largest spectral difference between vegetation and sand (Provoost et al., 2005; Radoux et al., 2016) and also is less affected atmospheric scatter (Donchyts, 2018). The latter reduces the impact of hazy atmospheric conditions. Secondly, the sigma value of the Gaussian filter indicates the standard deviation of the Gaussian filter and the size of the kernel used in the Gaussian filter (Maini and Aggarwal, 2008). The larger this value, the more an image is smoothed. The advantage is that high-frequency noise is smoothened out, though sharp and local edges can be eliminated. The fact that the size of the pixels (20-30 m for respectively the SWIR bands of Sentinel-2 and Landsat) is large compared to the blowouts (50-300 m), strong smoothing of the image using the Gaussian filter of the Canny edge detection would eliminate the edges of interest. Subsequently, a relatively low sigma value of 0.5 was chosen to eliminate high-frequency noise, while remaining sharp edges in the imagery. Thirdly, the threshold value is the actual value used to detect transitions in the band values, which determines the sensitivity of the edge detector. Since the application of the Canny edge detection focused on the general location of the edge, rather than resolving every small detail of the vegetation edge, a relatively large threshold sufficed. Subsequently, a threshold of 0.25 was found empirically to represent the absolute spectral signature between these land types correctly.

In line with Donchyts et al. (2018), only edges detected by the Canny algorithm with sufficient length were considered to represent true boundaries between sand and vegetation. Here, a minimum length of 10 connected pixels was considered as a true edge (Figure 4-14B and Figure A-6B). Segments of less than ten connected edges were suppressed from further analysis and referred to as artefact edges. If there were no edge pixels detected or they were of insufficient length, the image was excluded from the analysis. This might be related to poor illumination during acquisition (Figure A-8).

As a last step, a buffer around the detected edges was applied to define a spatial subset of interest (Figure 4-14C and Figure A-6C). It was assumed that the land covers of vegetation and sand were abundant in even proportions as the morphological dilation was applied on the detected edges. In the spatial subset, an Otsu threshold could then be safely determined from the NDVI values (Figure 4-14D and Figure A-6D). Vegetation was indicated by NDVI values above the Otsu threshold, while sparse and unvegetated area were represented by low NDVI values. Again, the number of histogram buckets was adapted based on the number of input values (see appendix B). In summary, a preliminary map of the three land features of interest (water, vegetation and sand) was determined based on the indices NDWI and NDVI and the Otsu threshold. As a result, as a subset of pixels for respectively vegetation, sand and water was obtained (Figure 4-14E and Figure A-6E).

4.5 Image Endmember selection

The previous steps spatially distinguished a first approximation water, sand and vegetation pixels. Firstly, from these initial estimates the largest frequency of the NDWI (water) and NDVI (sand and vegetation) values were derived. Secondly, the mean value of the representative pixels was then used as Image Endmember (IE), as it was assumed that the most occurring index values represented relative homogeneous land covers. A flowchart of this process is presented in Figure 4-15.

The IE potentially has the advantage to best represent the actual spectral signal of an image (Chang and Plaza, 2006; Hardy et al., 2020). It incorporates the natural variability in endmembers caused by seasonality and sensor resolutions (Keshava and Mustard, 2002)**.** The advantage of using IE for the LSU model is that it incorporates the full spectral range of data of the imagery for classification into fractional abundance. Besides, it is globally applicable and does not require prior comprehensive knowledge of the study area nor extensive user inputs.

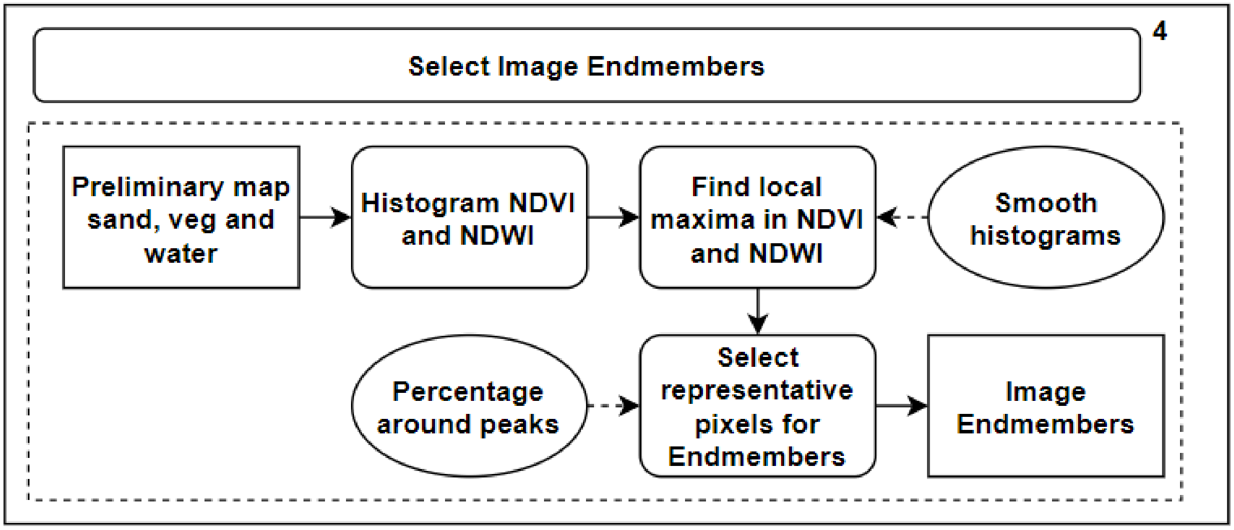

Figure 4-15; flowchart of the process from a preliminary map of the three land cover features water, sand and vegetation to the matrix of endmembers for each band. Note that this flowchart zooms in on box 4.5 "Select image Endmembers" of Figure 4-1.

As a first step, the largest frequencies of index values were selected as the local maxima of the subpart of the histogram of NDWI (water) or NDVI (sand or vegetation). Subpart of the histograms was obtained by selecting NDWI values higher than the Otsu threshold for water (Figure 4-16). For vegetation and sand, the histogram of NDVI was split in two by values respectively higher and lower than the Otsu threshold (Figure 4-17). The selection of local maxima may be prohibited when image histograms were spiky due to prevailing spectral reflectance values (Wegener, 1990; Schlingmeier and Schott, 1998), generally present in the 8-bit radiometric resolution of the Landsat 4, 5 and 7 sensors. Therefore, neighboring bins were averaged to smoothen the distribution of the index band values using a first order Savitzky-Golay (S-G) smoothing (Savitzky and Golay, 1964). The S-G smoothing is ideal to reduce noise while maintaining the shape and height of the actual data series (Schafer, 2011). Details about the first order S-G smoothing are provided in Appendix 0. The smoothed histogram bins were then used to calculate the local maxima. The local maxima were found as the zero crossing of the first derivative, where the highest frequency was selected in the case of multiple local maxima (Figure 4-16; Figure 4-17).

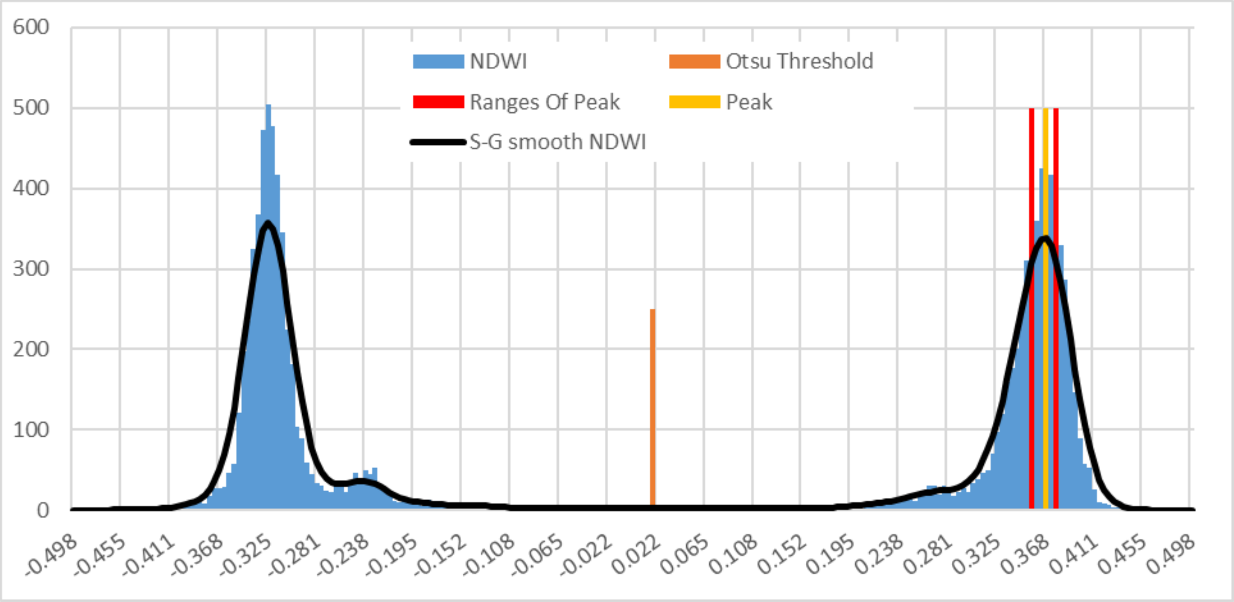

Figure 4-16; Histogram of NDWI for Landsat-8 image at June 3 2018 with its Savitzky-Golay smoothed histogram values and the corresponding peak and range of peak values for water (right). Otsu threshold was 0.018 and the peak value for water was 0.367.

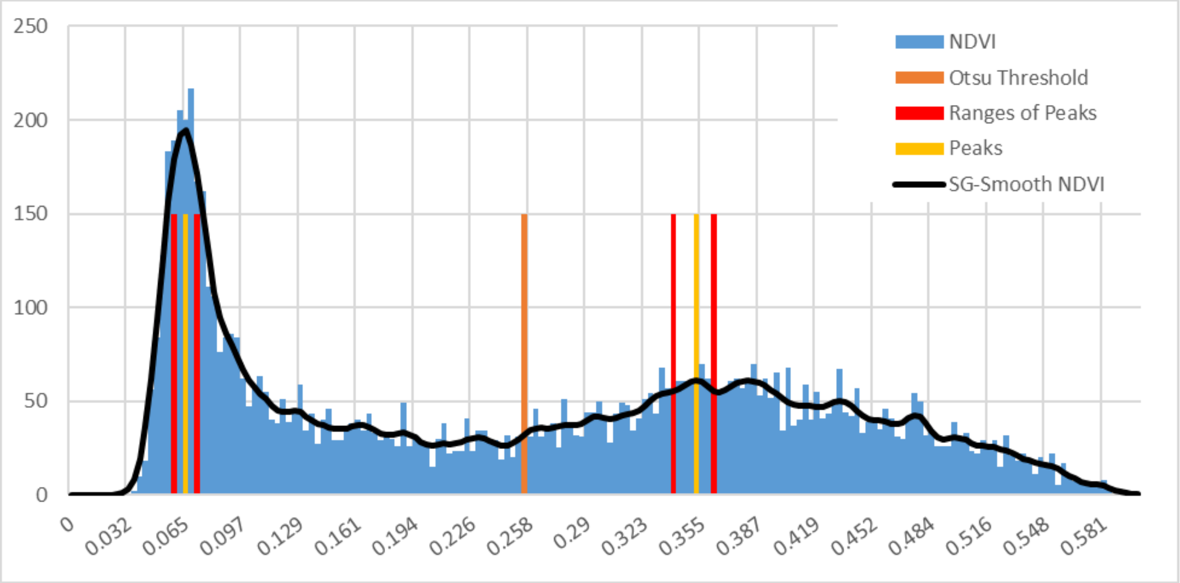

Figure 4-17; Histogram of NDVI for Sentinel-2 image of July 5 2017 with its Savitzky-Golay (SG) smoothed values and the corresponding peak and range of peak values for sand (left) and vegetation (right). Otsu threshold was -0.256, and the peak values for respectively sand and vegetation were 0.062 and 0.348.See code: B-10.

Secondly, the IE were calculated from a subset of pixels with index values around the local maxima of NDWI or NDVI. The range around the local maxima was estimated automatically as the index values at both side of the local maximum, where the number of observations was represented by 90% of those of the local maximum (Figure 4-16; Figure 4-17). The range was applied as it was assumed that a range of index values revealed a better representative spectral signature for each land cover type than a single index value. Consecutively, the range of the NDVI and NDWI values gave a subset of pixels *within* the previous classified map by the Otsu threshold (e.g. Figure 4-14E and Figure A-6E). Thus, based on a single index band, the most common index values within that spatial subset were selected and spatially presented in Figure 4-18A and Figure A-7A. The pixels within the range of index values were assumed to be representative for each of the three land cover types. The mean spectral value for each band was calculated from these pixels. This characterized the endmember for each of the three land cover features for each single image (Figure 4-18B and Figure A-7B).

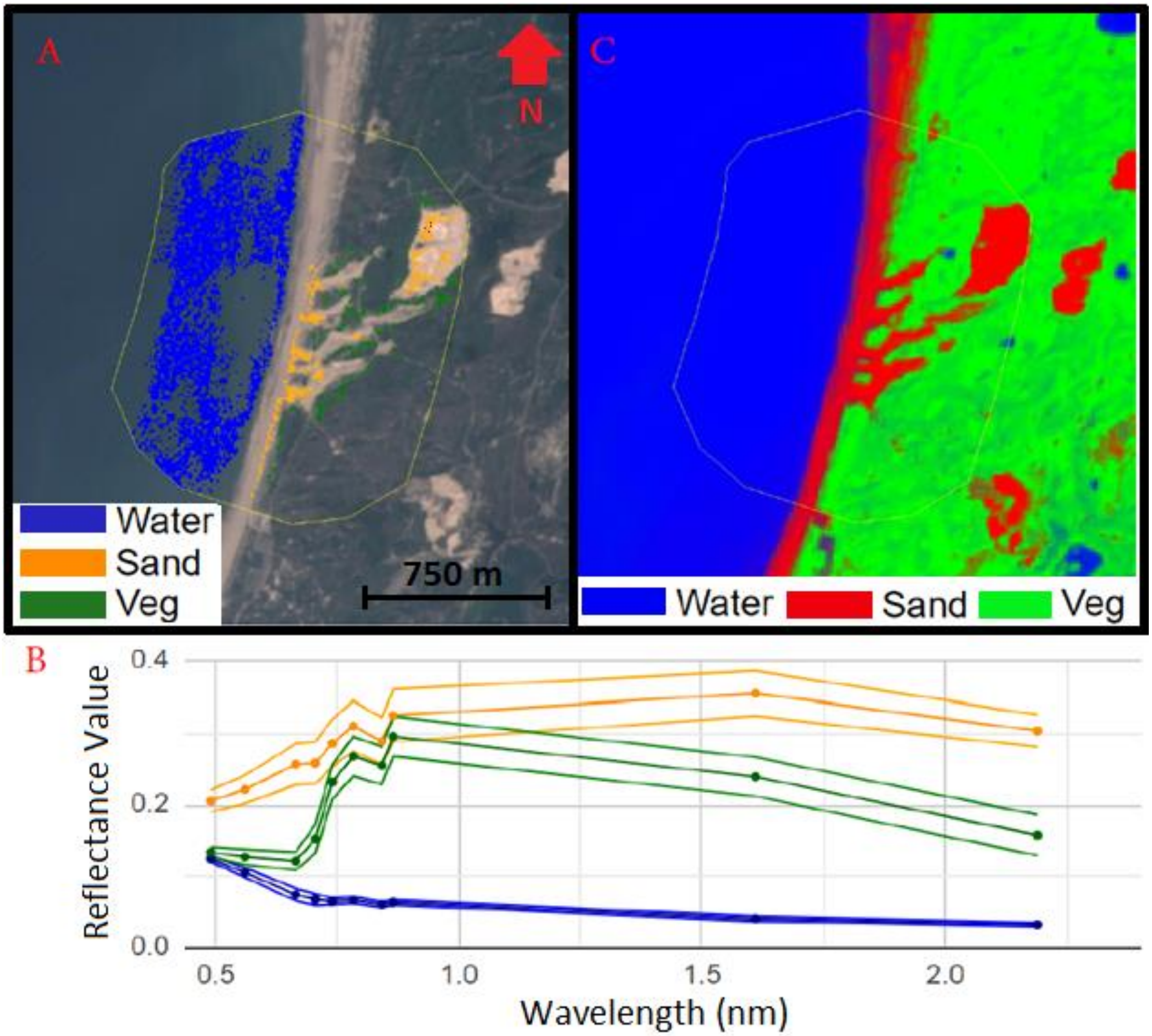

Figure 4-18; Sentinel-2 image of July 5 2017 for A) in true colour with on the foreground the selected pixels for the image endmembers (IE), B) the spectral response function for each land cover feature, with the central line representing the mean value and the lower and upper line one standard deviation, and C) the fractional abundance map of sand, water and vegetation. Legend in A corresponds to the colours in B. See code: B-11.

4.6 Linear Spectral Unmixing

To indicate bare sand areas in dunes, sub-pixel analysis using the Spectral Mixture Analysis (SMA) was chosen (Keshava and Mustard, 2002; Somers et al., 2011). This method assumes that every pixel is a combination of the spectral signature of all objects within that pixel, weighted by their spatial abundance (Keshava and Mustard, 2002). These objects have distinctive spectral properties and are called *endmembers*, and the fraction within the pixel they appear is called *fractional abundance* (Keshava and Mustard, 2002). When the number of objects of a certain area is known a priori, in theory that would mean that the spectral signal of every pixel can be described as a fraction of the endmembers present. Subsequently, every single pixel can thus be described as

$$f'_e = S_b \times E_{b,e} + w_b \tag{3}$$

where f' is the mathematically correct vector of fractional cover for every endmember e, defined by the vector of spectral signal S for every band b and the matrix of endmembers E for every band and endmember, plus the additive noise vector w for every band (Keshava and Mustard, 2002; Somers et al., 2011). Although the additive noise vector w allows to solve equation (3) mathematically, physically it has no meaning. To make sense physically, no additive error should be present, which assumes that solar radiation is reflected with a single bounce over the full pixel size towards the satellite sensor. Though that is typically not the case on the earth's surface, it allows to relate the spectral response of a pixel to the fractional abundance of each endmember within that pixel (Nash and Conel, 1974; Roberts et al., 1993; Keshava and Mustard, 2002). This requires two constraints to be included: 1) nonnegativity, and 2) full additivity (Keshava and Mustard, 2002). First, every endmember fraction should be nonnegative (i.e. there cannot be a negative fractional abundance of an endmember), meaning that $f_e \geq 0$. Furthermore, the summation of the fractional coverage should equal 1, meaning that $\sum f_e = 1$. Rewriting equation (3), every single pixel can thus be described as

$$f_e = S_b \times E_{b,e} \tag{4}$$

where, in contrast to equation (3), f is the vector of fractional cover for every endmember e, constraint to $f_e \geq 0$ and $\sum f_e = 1$. This type of a linear mixture model is called Linear Spectral Unmixing (LSU). Despite on the earth's surface the conditions for LSU are almost never met, the mixed pixels problems is most frequently solved using linear models (Keshava and Mustard, 2002). Within the GEE environment, nonnegativity is applied using the common active set method (Murty and Yu, 1988; Hancher, 2018), while the full additivity is added using Lagrange multipliers (Kay, 1993; Hancher, 2018). Endmembers were defined in the previous section as Image Endmembers (IE), and unmixing of these endmembers into a per-pixel fractional cover was done using equation (4). Figure 4-18C and Figure A-7C show examples of these *unmixed* images.

Mathematically, the best unmixing models are obtained using the unmixing model without the constraints of nonnegativity and full additivity (Van Der Meer, 1999; Keshava and Mustard, 2002). Subsequently, each image was also inverted into fractional cover without the constraints applied in equation (3). This gave the mathematically correct vector of fractional abundance of the endmembers (f'_e). Using matrix multiplication, the unmixing process was reversed to obtain the corresponding spectral values for each band using the unconstrained fractional abundance vector and the endmember matrix:

$$S'_b = f'_e \times E_{b,e} \tag{5}$$

where the modelled, reversed spectral values at each pixel were given by S'_b, $E_{b,e}$ is the endmember matrix and f'_e is the unconstraint fractional abundance vector. The subscript *e* and *b* represented the axis for respectively the endmembers and the spectral bands. Then, difference between the actual spectral values of the image and the reversed unmixed image was calculated using

$$w_b = S_b - S'_b \tag{6}$$

by subtracting the modelled image (S'_b) from the actual image (S_b), which gave the additive noise vector w_b, similar as in equation (3). Finally, the Root-Mean-Squared-Error (RMSE) for every pixel was obtained using

$$RMSE_{pixel} = \left(\sum_{b=0}^{n} \frac{(w_b)^2}{n} \right)^{\frac{1}{2}} \tag{7}$$

by squaring the additive noise vector, summing all squared values and divide that by the number of bands *n*. Finally, the root of that value was taken. The overall image or region specific RMSE was estimated using

$$RMSE_{region} = \sum_{i=0}^{m} \frac{RMSE_{pixel}}{m} \tag{8}$$

where the RMSE was the summation of all RMSE pixel values and *m* the number of pixels within a specified region (see for equations 5-8: Van der Meer, 1999). The RMSE indicated the overall goodness of the unmixed image. A relative high RMSE, which was defined as a value higher than the instrument noise, indicated a poor fit of the modelled image endmembers (Mertes et al., 1993). The instrument noise, indicated as the Signal to Noise ratio and scaled to floating values, is found around 0.018 for Landsat-8 imagery for the Near Infrared and Red bands (Ren et al., 2014) and on average 0.012 for the Sentinel-2A used visible and infrared bands (Drusch et al., 2012). High RMSE values indicate image spectra outside the endmember domain (Van Der Meer, 1999; Keshava and Mustard, 2002). Ideally, high RMSE values are not found within the Region of Interest (ROI), as pixels with a high RMSE indicate that the set of endmembers does not represented all pixels within the ROI.

A unique advantage of spectral mixture analysis is that each single pixel is divided into subpixel components. Subsequently, the shade fraction of a pixel can be estimated for a single pixel. Namely, as natural surfaces are never illuminated perfectly, variation in topography, vegetation or build-up features can result in a mixture of shadow in the spectral reflectance on a sub-pixel scale (Keshava and Mustard, 2002; Powell et al., 2007). Although no specific shade endmember was applied in this study, the water endmember was spectrally close to that of shade (Mertes et al., 1993). Thus, the water endmember was used to estimate the shade fraction on a sub-pixel scale.

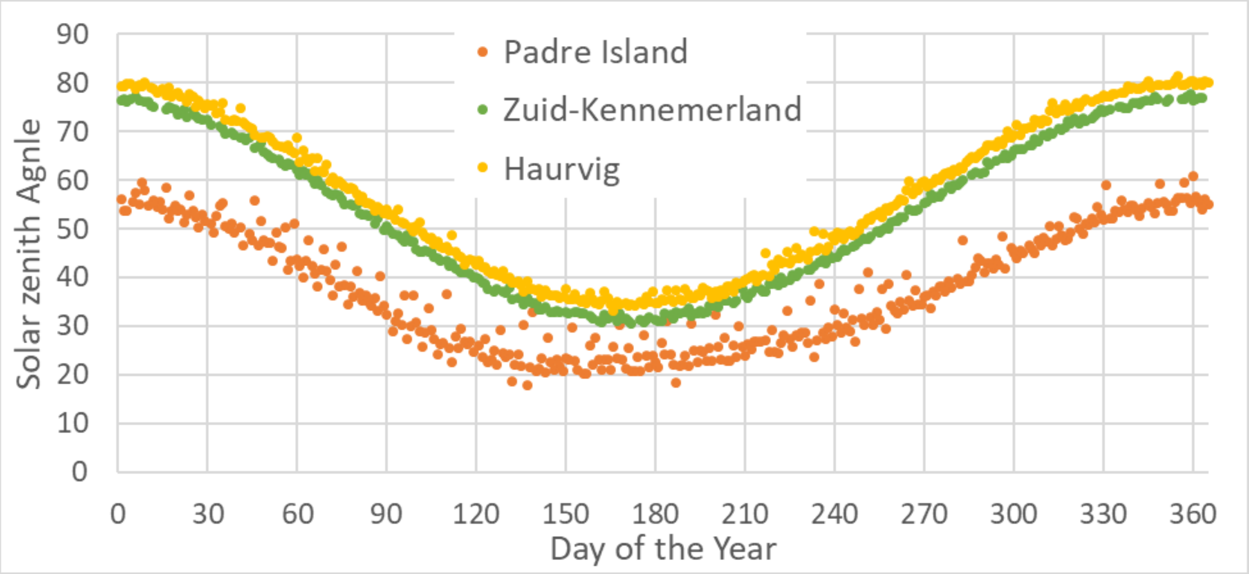

Figure 4-19; Mean solar zenith angle over the day of the year as was present in the metadata of the used imagery.

Regarding the nature of the trough blowouts, it was assumed that shadow was present at the low-lying blowout throats and at the lateral walls. Consequently, the fractional abundance of water within the BROI was hypothesized to be relief-based shadow. More precisely, at the blowouts at the higher latitudes (Haurvig, Zuid-Kennemerland), shadow covered a substantial amount of the blowout during the winter season. This related to the higher sun angle of the imagery (Figure 4-19) and the fact that these blowouts are located in relatively high (10-12 m) foredunes. For these blowouts, each pixel within the BROI was analyzed following

$$f_e = f_{veg} + f'_{sand} \tag{9}$$

where f_{veg} was the fractional abundance of vegetation and f_e the total fractional abundance of the endmembers, while f'_{sand} was defined as

$$f'_{sand} = f_{water} + f_{sand} \tag{10}$$

where f_{sand} was the original fractional abundance of sand, f_{water} the fractional abundance of water and f'_{sand} the expected fractional abundance of sand, following the argumentation depicted previously. At Padre Island, the sun angle was relatively low (Figure 4-19) and the region was characterized by relatively low foredunes (1-5 m). Moreover, actual water was regularly present within the BROI when water table rises by for example overwash or high precipitation (Kocurek et al., 1992; Jewell et al., 2014). Therefore, the shadow correction method as discussed here was only applied to the Kennemer and Haurvig study site.

4.7 Blowout Extent and vegetation proxy

The basis for the detection of the blowout extent consisted of the unmixed image. Trough blowouts were characterized by their unvegetated corridor connecting the beach to the backdunes through vegetated foredunes. The spectral difference emerging from different land cover allowed the detection of the trough blowouts within the foredunes from the satellite imagery. However, the open connection to the beach did not define a spectral difference between the entrance of the blowout and the beach itself. Therefore, the beach entrance of the trough blowouts was confined to a maximum spatial extent based on the timeseries.

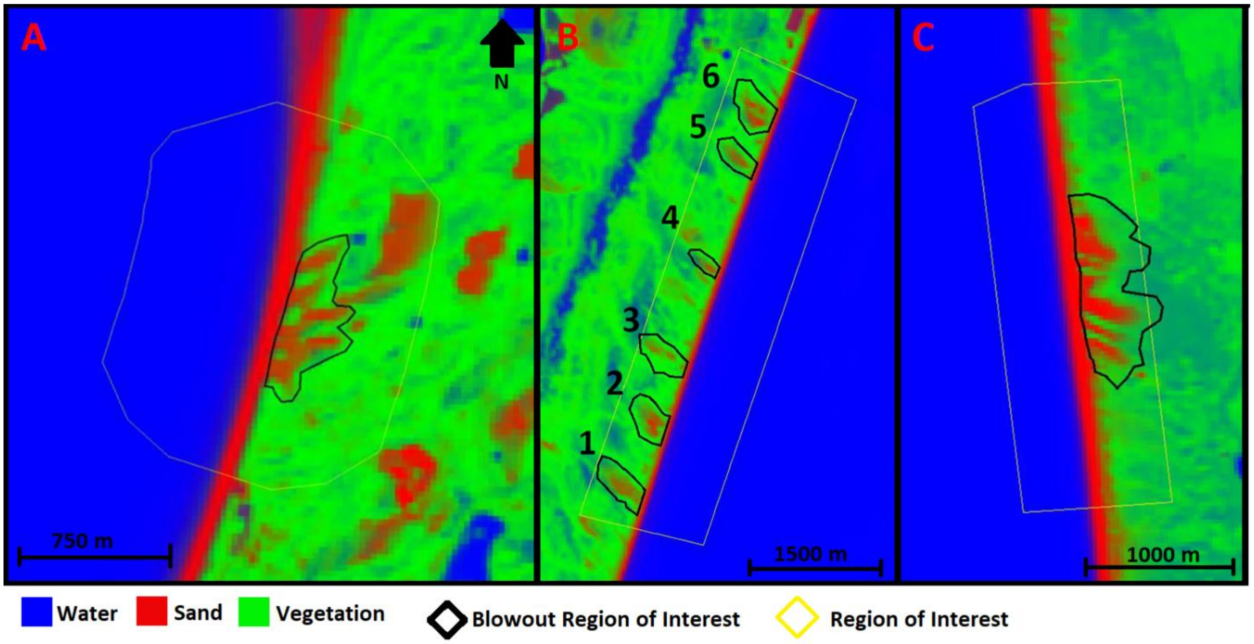

Figure 4-20; Composite images of A) Zuid-Kennemerland, B) Padre Island and C) Haurvig. Images show the fractional cover obtained from the LSU image composites (see text for explanation). For Padre Island (B), the blowouts could be individually determined and are labelled 1 to 6.

A timeseries of fractional abundances of sand, vegetation and water (i.e. the unmixed images) was made by yearly composition of the imagery using the median value. Yearly composites were made a-priory, as there is a skewed distribution of image availability over time (Figure 3-7). These yearly composites were summed to estimate the spatial evolution of the blowout over time (Figure 4-20). The border between the beach and blowout entrance was visually determined by alongshore lengthening of the transition between the beach and the vegetated foredune on either side of the blowout. Subsequently, a specified spatial extent within the ROI where the blowout evolved over time was determined. This area is referred to as the Blowout Region of Interest (BROI) and shown for each study area in Figure 4-20. The Zuid-Kennemerland and Haurvig study area were characterized by multiple blowouts throats located close together. Accordingly, on the scale of the coarsest resolution satellite imagery (30 m), single trough blowouts could not be determined consecutively throughout the timeseries. Therefore, the blowouts within these study sites were aggregated together in one single BROI. On the other hand, the blowouts located in the Padre Island could be monitored individually as they had sufficient alongshore spacing. Then, within the BROI and for every single image, pixels were assigned to the blowout when the fractional abundance of sand was above 50%. The estimated area of the blowout will be further referred to as the Blowout Extent (BE).

Within the BE, a proxy for the vegetation encroachment or decay was estimated using the NDVI. The NDVI is a common and proven way to represent vegetation cover within a pixel (Ormsby et al., 1987; Carlson and Ripley, 1997) and also works well if no properties of the soil were known (Purevdorj et al., 1998). An increase in the NDVI value indicated an increased photosynthetic active radiation within a pixel and thus as a proxy for the vegetation growth. A weighted mean NDVI value for the pixels within the BE was calculated. Moreover, inter-image differences NDVI values were determined to show spatiotemporal evolution of the vegetation within and in the vicinity of the blowouts.

Inter-sensor spectral differences may result in undesired variation in NDVI values, and thus in inadequate proxies for vegetation cover. The spectral resolution of the Landsat-4, 5 and 7 and Sentinel-2 for the red and NIR band was comparable (Figure 3-6). For example, on average the NDVI variated 2.5% between the Landsat-5 and Landsat-7 and 3.1% between Landsat-7 and Sentinel-2 (Teillet et al., 2001; D'Odorico et al., 2013). However, that did not account for the NIR band of the Landsat-8 sensor, such that calibration of the NDVI value was necessary to align the NDVI value with the other datasets (Roy et al., 2016). This was specifically found in areas of low vegetation cover between the Landsat-7 and Landast-8 sensors (Xu and Guo, 2014). Subsequently, the NDVI from the Landsat-8 sensor was calibrated to correspond with the other datasets using

$$NDVI_{cal} = -0.0195 + 1.0348 \times NDVI_{L8} \tag{11}$$

where $\mathrm{NDVI}_{\mathrm{cal}}$ was the calibrated NDVI used as vegetation proxy for the Landsat-8 imagery and $\mathrm{NDVI}_{\mathrm{L8}}$ was the actual NDVI value captured by the Landsat-8 sensor. This linear cross-calibration was found to represent best the actual NDVI value between the Landsat-8 and Sentinel-2 sensors (Zhang et al., 2018).

4.8 Accuracy assessment of the satellite imagery

The validation of the proposed methodology in the previous section was performed using six high resolution (1 m) Unmanned-Air-Vehicle (UAV) images of the Zuid-Kennemerland study area. As the area had been shown to be highly dynamic (e.g. Ruessink et al., 2018), only satellite imagery taken within 1 month of the flight date of a UAV image were considered for validating the satellite imagery. Accordingly, 36 satellite images were compared to the six UAV images, consisting of 15 Landsat-7, 14 Landsat-8 and 7 Sentinel-2A images.

4.8.1 The UAV vegetation index

The UAV images were a different dataset that could not be processed using the workflow as proposed for moderate resolution satellite imagery. Firstly, the spectral indices used for the vegetation and water detection (section 4.3) could not be calculated for the UAV images as they did not capture information in the infrared part of the light spectrum. Secondly, valuable LMM products can only be achieved if there are more bands than endmembers (Keshava and Mustard, 2002; Chen et al., 2010), which was not the case for the three-banded UAV imagery (Figure 3-6). Nevertheless, the high spatial resolution allowed to validate the products of the satellite imagery on a sub-pixel scale.

The detection of water can be difficult, as the separation between water and land cover features relies mainly on differences in the infrared region of the spectrum (McFeeters, 1996; Foody et al., 2005). Also, the spatial coverage of the UAV images was mostly limited to land area (Figure 3-9). Subsequently, the validation with UAV imagery aimed at the separation of sand and vegetation. For this binary classification, the ExGminExR vegetation index was used (Meyer and Neto, 2008; Ruessink et al., 2018), which was defined as

$$ExGminExR = (2g - r - b) - (1.4r - b) \tag{12}$$

where *b*, *g* and *r* correspond to respectively the 8-bit bands of blue, green and red (Meyer and Neto, 2008). Relative high reflectance of vegetation in the green band and relative absorption in the red band presented the vegetation by relative high ExGminExR values (Figure 3-3). On the other hand, sand was generally presented by relative high reflectance in the red band and lower reflectance in the blue and green band (Figure 3-3). Subsequently, sand was highlighted by relatively low ExGminExR values.

A binary classification of sand and vegetation was made using the Otsu threshold (Otsu, 1979). This separated sand from vegetation on a 1 m spatial resolution using an image specific threshold. In line with Ruessink et al (2018), the Otsu was assumed to be a necessary additional step in contrast to the introduced fixed threshold of zero by Meyer and Neto (2008). Unfortunately, the classification of the UAV imagery using this methodology classified shadows as vegetation. Considering the nature of coastal trough blowouts, relief-based shadows were most likely part of the sandy lateral wall or throat of the blowout. In line with Ruessink et al. (2018), relief-based shadows on the northern facing slopes were manually corrected for the October 2014 and March 2017 images.

4.8.2 Accuracy assessment

A confusion matrix was constructed to compare the unmixed sand cover fraction from the satellite imagery with the 1 m resolution UAV images. Sub-pixel fractional cover of sand, vegetation and water was produced by the Linear Spectral Unmixing (LSU) model on the spatial resolution of the satellite imagery. On a 1 m spatial resolution, the UAV images were classified into sand and vegetation. Subsequently, about

100 (Sentinel-2, 10 m resolution) or 900 (Landsat, 30 m resolution) UAV 1 by 1 m pixels were analysed for every pixel of the satellite imagery. Within each medium resolution satellite imagery pixels, the fractional cover of sand classified UAV pixels was compared. The confusion matrix was then built up from 10 classes, each regularly spaced from 0 to 100 per cent of sand coverage.

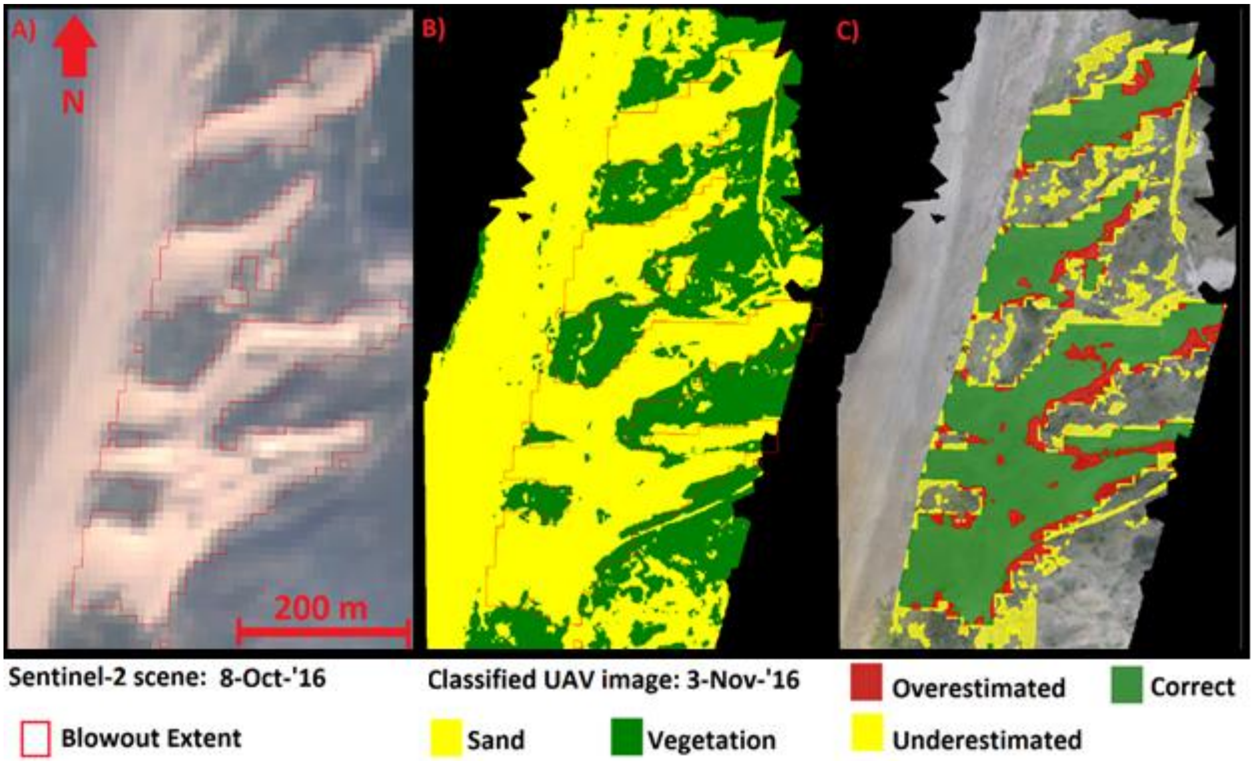

Figure 4-21; A) Sentinel-2 scene with the estimated blowout extent, B) classified UAV image using Otsu-threshold, and C) Comparison of the Blowout Extent estimated from image A and image B, with the UAV image on the background.

Furthermore, the estimated Blowout Extent (BE) for the satellite imagery was compared to the BE calculated from the UAV imagery. An example of this procedure is given in Figure 4-21. The BE for the UAV images was calculated from the sand classified pixels within the Blowout Region of Interest (BROI). In case that the UAV image did not completely spatially cover the BROI, the BE was estimated only for that part of the BROI covered by the UAV image. Subsequently, the area of the blowout of the ground-truth reference (UAV imagery) was compared qualitatively to the blowout subtracted from the satellite imagery. Also, the area of over and underestimation of the ground-truth reference were calculated (Figure 4-21).

5 Results

5.1 Validation of satellite derived sand-vegetation classification

Before the results on the spatiotemporal development of the blowouts at the three study sites are presented and examined, first the validity of the applied methodology was studied using the six available UAV orthomosaics at Zuid-Kennemerland. This validation is presented as a confusion matrix of the per pixel fractional sand cover and the total area of the blowout.

Table 5-1; Confusion matrix for the fractional cover of sand from the reference image (UAV) and the classified satellite imagery. Numbers refer to the number of pixels at the resolution of the satellite imagery.

		REFERENCE: Sand fraction from UAV imagery										Total
		0-10	10-20	20-30	30-40	40-50	50-60	60-70	70-80	80-90	90-100	
Classified: Sand fraction from satellite imagery	0-10	1354	623	519	451	345	349	270	227	165	323	4626
	10-20	411	190	163	151	162	151	92	112	104	200	1736
	20-30	270	132	139	117	164	164	95	106	105	265	1557
	30-40	167	112	136	158	138	118	106	89	119	374	1517
	40-50	121	96	113	135	137	138	125	137	163	529	1694
	50-60	79	68	85	94	109	119	149	161	163	741	1768
	60-70	69	58	69	84	86	112	159	174	199	982	1992
	70-80	33	39	45	51	81	84	133	172	298	1390	2326
	80-90	27	27	39	33	69	87	133	190	285	2164	3054
	90-100	25	58	67	66	100	122	270	469	653	9918	11748
Total		2556	1403	1375	1340	1391	1444	1532	1837	2254	16886	32018

The confusion matrix of fractional sand cover of the satellite and UAV imagery is given in Table 5-1. About half of the UAV pixels (almost) purely was sand covered (sand fraction > 90%), as the UAV imagery was taken just around the extent of the blowouts. The fractional cover from the LSU model classified 40% of the pixels in the same category as the reference images. About two-third of the pixels (71%) were classified in a category within 20% of the reference images. A minority of the satellite pixels (13%) were given a fractional sand cover over 50 per cent differing to the percentage of sand pixels from the UAV images.

The area of the blowout at the Zuid-Kennemerland study site estimated from the UAV images was slightly underestimated (about 2%) by the satellite imagery. Nine satellite images overestimated the area by 5%, while 14 images underestimated the area over 5%. The area of the blowout obtained from the UAV image on 28 October 2014, although only compared to two satellite images, was largest underestimated by respectively 14% and 21%. The first satellite image on 16 March 2014 had the largest overestimation of the area (16%). Compared to the reference UAV estimated area, the Sentinel-2 images gave better area estimations (99.8% ±5.5%) than the Landsat imagery (98.0% ±9.4%). On average, the blowout area for the Sentinel-2 imagery differed 6,161 m^2 ±3422 m^2 from the area reference UAV data, while for the 30 m resolution Landsat data these numbers were 9,615 m^2 ±5,843 m^2

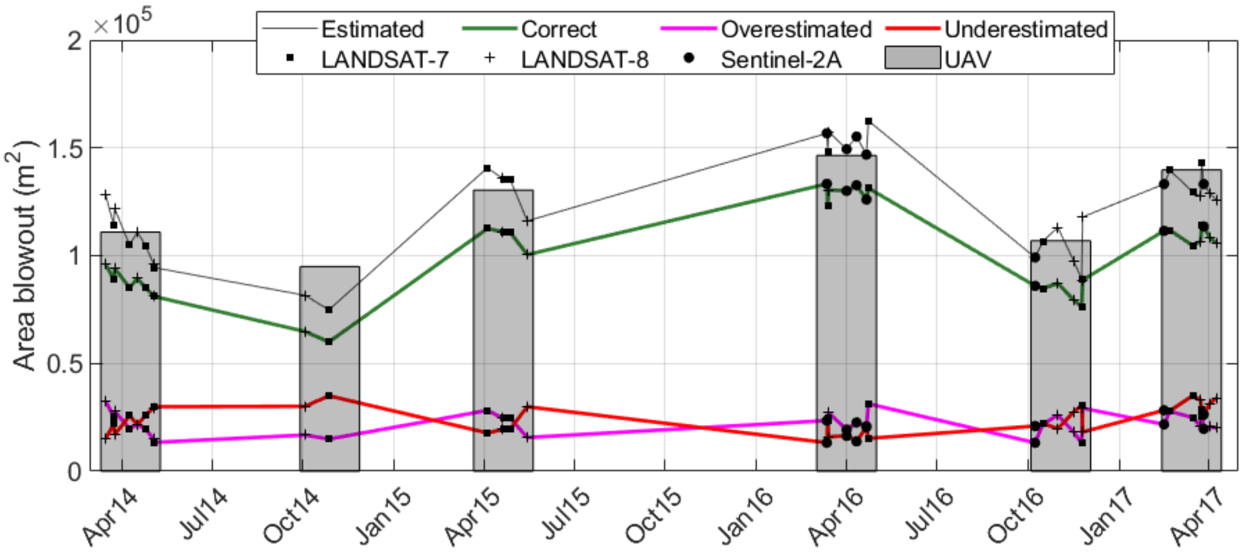

Figure 5-1; Area of the blowout calculated from the UAV and satellites within the Blowout Region of Interest (BROI).

Overall, the UAV images and within the Blowout Region of Interest (BROI), 64.2% of the area was determined as blowout (sand) and 35.8% as non-blowout (vegetation) (Table 5-2). For the satellite imagery, 52.0% of the area of the blowout was correctly classified as sand, while 24.5% was correctly classified as vegetation. The under and overestimation of the area of the blowout (Figure 5-1) refer respectively to sand classified as vegetation and vegetation classified as sand. Under and overestimations were a logical result of differences in sensor resolutions but were for most images in balance (Table 5-2; 11.4 versus 12.2%). As a result, the estimated area of the Blowout Extent (BE) corresponded well (within 2%) to the ground-truth reference area. Thus, it is safe to say that the proposed methodology has a sufficient accuracy to examine spatiotemporal evolution of trough blowouts in vegetated foredunes with medium-resolution (10-30 m) satellite imagery.

Table 5-2; Summed area (m²) of the blowout within the Blowout Region of Interest (BROI) for the reference UAV images and the classified satellite imagery calculated at the 1 m resolution of the UAV images.

		REFERENCE: UAV				TOTAL	
		Sand	Percentage	Veg	Percentage	Pixels	Percentage
CLASSIFIED	Sand	3657284	52.0	799195	11.4	4456479	63.3
	Veg	857030	12.2	1721611	24.5	2578641	36.7
TOTAL		4514314	64.2	2520806	35.8	7035120	100.0

5.2 Zuid-Kennemerland

5.2.1 Multi-year spatiotemporal development blowouts

In the winter of 2012-2013, the five adjacent notches at Zuid-Kennemerland were excavated. Obviously, this was reflected in the observed area of the blowouts, which reached almost 100,000 m^2 shortly after excavation (Figure 5-2). The small areas observed in the four years before were mainly related to the beach extending land inward into the Blowout Region of Interest (BROI) (Figure 5-2). There was a clear seasonal pattern in the area over the years. Largest Blowout Extents (BE) were observed at the end of the winter (March-April), while relatively low BE were observed at the end of the summer (August-September). Taking the maximum end winter BE as a reference, the area of the blowouts grew about 20.000 m^2 per year in the first three years after excavation. In the spring of 2016, a maximum extent of around 160,000 m^2 was reached (Figure 5-2). Up to 2020, the area did not grow substantially more than the area reached in the first months of 2016. Surprisingly, the extent expanded only to about 140,000 m^2 in the winter of 2017. After each maximum extent reached at the end of the winter, the area of the blowouts diminishes up to 30,000 to 50,000 m^2 (Figure 5-2). The extent at the end of the summer grew rapidly (30,000 m^2/year) in the first two years towards about 110,000 m^2 in the summer of 2015, similar to the increase observed from the winter extents. The last five years, the summer extents yearly returned to around 110,000 m^2. Moreover, the extents subtracted from the UAV images were added within the temporal chart and fitted well within the estimated 2-monthly moving average trendline (Figure 5-2).

The BE increased sharply from near 0 to almost 100.000 m^2 due to excavation of the notches in the winter of 2012-2013. In the period before excavation (2009-2012), no significant sand areas were present within the BROI, apart from some patches along the beach and two small (< 900 m^2) areas in the north and south during the winter months (Figure 5-3). Figure 5-2 (upper left) shows the transformation the study area underwent from three consecutive Landsat-7 images. Before the excavation, the foredune was clearly vegetated and separated the sandy beach from the backdunes (Figure 5-2).

Just after excavation the five adjacent notches were detectable (Figure 5-2). The devegetated parabolic dunes (‘Peperdel’ and ‘Kattendel’) were located just land inward and partly disconnected from the blowouts, especially during the summer months (Figure 5-3). The second and third notches (from the south) were not independently detectable from the 30 m Landsat imagery and are thus shown connected. Within in one year after excavation (Figure 5-2), the area in between the devegetated slopes and the notches became connected. The increase in the BE in the first year after excavation to 120.000 m^2 was mainly related to the growth in sand area just landward of the excavated blowout throats, illustrating the development of depositional lobes.

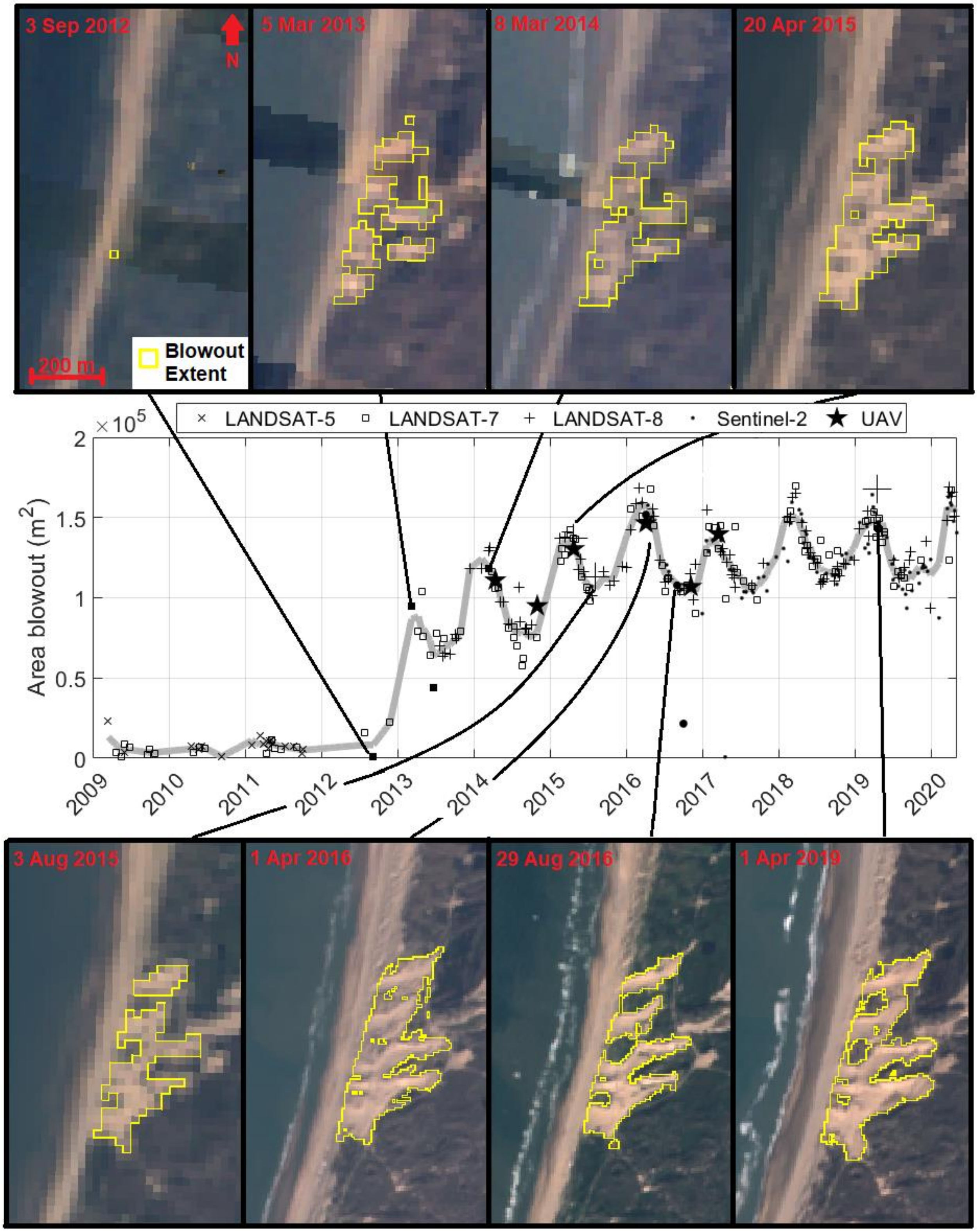

Figure 5-2; The blowout extent over time for the satellites and the UAV images at Zuid-Kennemerland (center). In grey a 3-monthly moving average for the satellite data is shown. Example imagery are given around the graph and in Figure 6-3. Example images are highlighted with larger (Landsat-8 and Sentinel-2) and filled (Landsat-7) symbols. See for all images: B-5

Three to five years after excavation (2015-2017), the BE expanded dominantly in northeastern direction. Both devegetated parabolic dunes became year-round connected to the first, second and third notches (Figure 5-3). The third and fourth notches became connected even during the summer. This resulted in an increase of the extent to around 160.000 m^2 in the April 2016. Meanwhile from 2014 onwards, the most northern notch kept expanding in northeastern direction, while the four southern notches had reached their maximum landward winter extent already in 2014 (Figure 5-3). In contrast, the southern notch, including parts of the southern devegetated parabolic dune, grew dominantly east to southeasterly in the last five years (Figure 5-3). With the addition of the Sentinel-2 10 m resolution imagery from 2015, the vegetated ridge between the second and third notch could be detected. Since 2016, the annual maximum BE did not increase anymore and stabilized around 160.000 m^2 and seasonal variation in the extent were dominant (Figure 5-2).

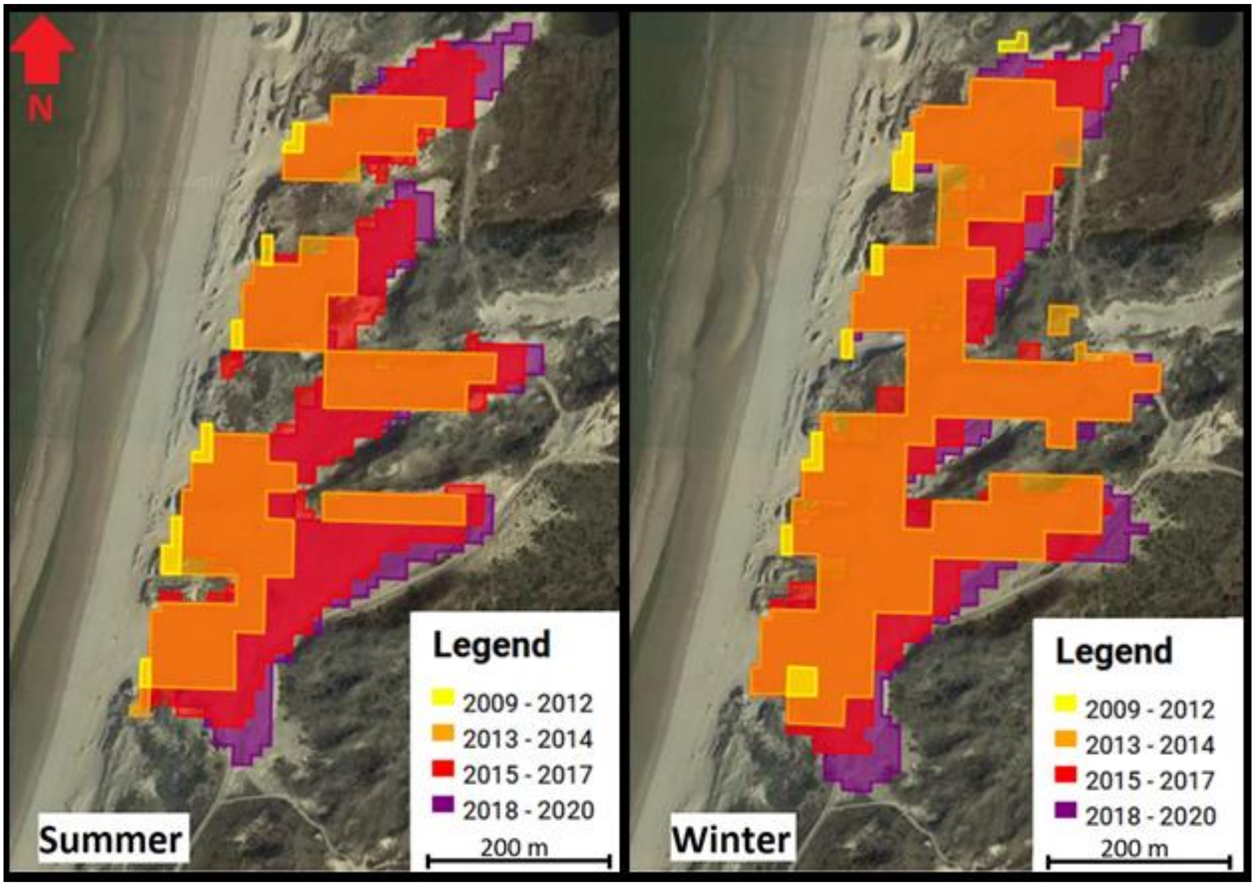

Figure 5-3; Mean composites of the extent of the blowout in two to three-year intervals for the summer (June-August) and winter (December-March), on top of a Google Earth image at March 20th 2019.

5.2.2 Seasonal variations blowouts

The BE clearly fluctuated between a local maximum (around April) till a local minimum (around August) in the entire study period. The difference between minimum and maximum BE was typically 50.000 m^2. As an example for the seasonal differences, two Landsat-8 images and two Sentinel-2 are chronically shown in Figure 5-2. The difference in BE between August and April was mainly due to the change from sand to vegetation 1) in the area between the notches and 2) on the landward side between the former parabolic dunes. In the summer, the northern two notches and the most southern notch were detected separately as the presence of vegetation allowed for sufficient spectral difference between the adjacent notches. Contrary, no clear separation was detected between the second and third notches. At the end of the winter, relatively more sand was present between the adjacent notches, disabling the detection of the individual notches on the resolution of the Landsat and Sentinel-2 imagery. Moreover, the blowout depositional lobes extended further (30-50 m) land inward. This combination resulted in strong seasonal fluctuation of the BE.

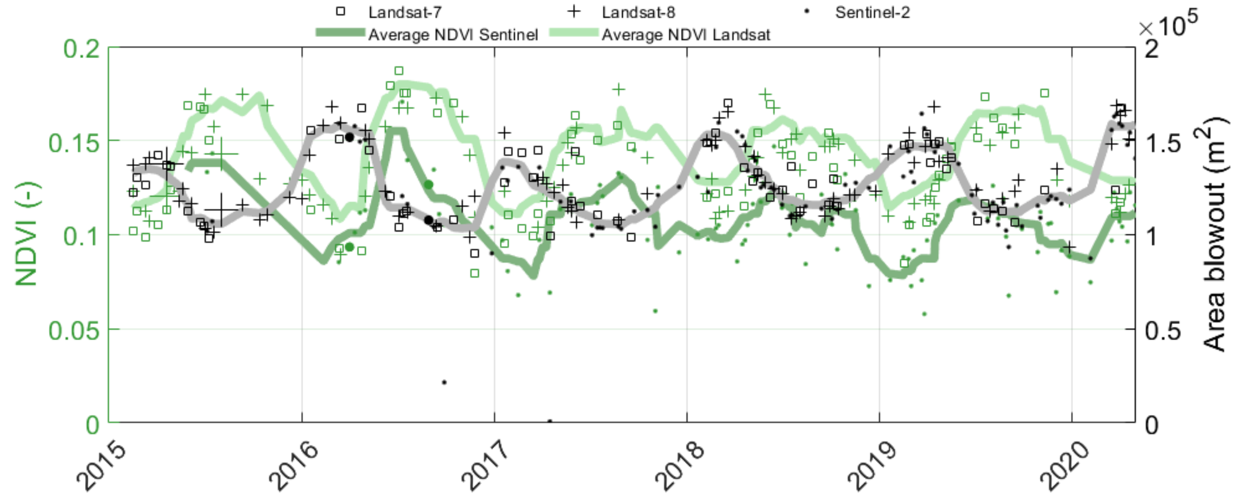

Figure 5-4; The vegetation proxy NDVI and the Blowout Extent (BE) for January-2015 till May-2020 plotted over time. The light green and grey shaded lines refer to the 3-monthly moving average, for respectively the NDVI (separately for Landsat and Sentinel sensors) and BE. Selected example images (Figure 5-2; Figure 5-5) are highlighted with enlarged symbols.

The seasonal variations in the BE were further examined using the Normalized Difference Vegetation Index (NDVI) in and around the BE for the period 2015-2020 (Figure 5-4). This period excluded the multi-annual grow of the BE not relevant for the seasonal changes. While the maximum extent of the blowouts was reached yearly in March or April, the NDVI value, serving as a proxy for the vegetation cover inside the Blowout Extent (BE), was minimal during those months (Figure 5-4). As the blowouts increased in their extents through the months December to March, the NDVI started increasing in the beginning of April and reached a maximum around 0.18 in June. The NDVI value dropped starting in the end of the summer and generally reached a minimum value around 0.1 in January and February. The NDVI value increased over approximately three months, while the NDVI lowered relatively slowly over the autumn and winter. Subsequently, the relatively small BE in the summer had an overall higher NDVI value than the relatively large BE during the winters. A difference of about 0.03 was found between the NDVI value of the Landsat and Sentinel-2 missions. Nevertheless, the pattern of increase and decrease of the NDVI value, thus growth and decay of the vegetation, within the blowouts was similar for both missions.

Spatially, the variation of the NDVI value is shown in Figure 5-5. Within the summer extents of the blowouts, increase in the NDVI value was observed. For the coarser Landsat-8 imagery (Figure 5-5A), the total NDVI increased about 0.023 mainly due to an increase of the NDVI vale at pixels located at the edge of the blowout extent. For the 10 m resolution Sentinel-2 imagery (Figure 5-5B), the total NDVI increased about 0.033. The increase was observed at two patches within the devegetated parabolic dunes and at the landward part of the fourth and fifth blowout. Subsequently, the overall NDVI value within the blowout extent increased by increment of the vegetation at the depositional lobes of the blowouts. NDVI values also increased sharply (> 0.3) between the blowout throats, which clearly indicates why those areas were not part of the blowouts during the summers (Figure 5-2).

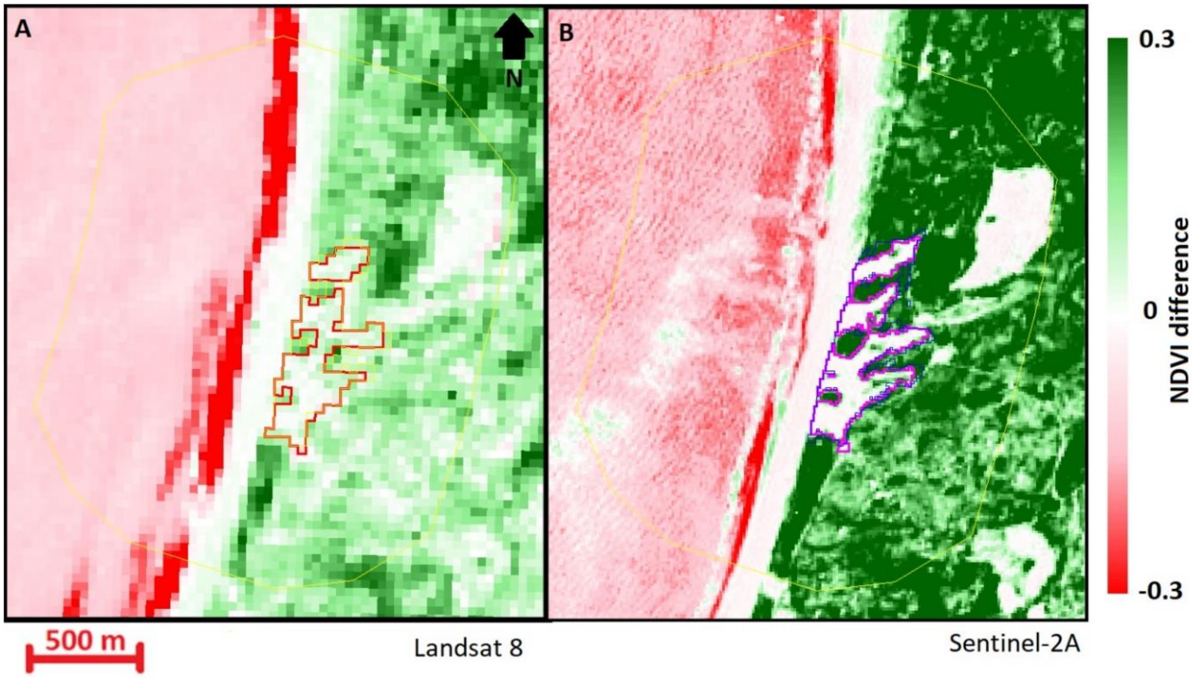

Figure 5-5: NDVI difference between A) Landsat-8 images in 2015, and B) Sentinel-2A images in 2016. The Region of Interest and Blowout Extents are given in correspondence to the true color images in Figure 5-2.

5.3 Padre island

The blowouts at Padre Island were spatially sufficiently separated to track the development of each individual blowout at the resolution of the coarsest used satellite imagery (30 m). Furthermore, the blowouts showed different stages of growth and decay in area. As such, the BE and NDVI values will be presented over time and discussed sequentially for each of the 6 individual blowouts (Figure 5-6). No clear seasonal pattern in the increase and decrease in the extents of the blowouts was observed for the Padre Island study site. Variations in the NDVI value within the BE were rather episodic, or varied on multi-annual time scales (Figure 5-6). Overall, the NDVI value remained low (< 0.15) during the summer (May-October) when the blowout had a significant size (> 20,000 m^2).

The most southern blowout (1) was connected to the beach by a relatively long (300 m) alongshore sandy patches at the start of observations from 1984 to 1990 (Figure 5-7A). Over the whole study period, the landward extent transgressed about 500 m landward in north westerly direction at a rate of 13 m/year. While transgressing landward, the BE gradually grew from 25,000 m^2 to 54,000 m^2 between 1984 and 2014 (Figure 5-6). Growth of the area was a result of alongshore widening from about 120 m in 1985 to 250 m in 2005, resulting in a circular shape of the blowout (Figure 5-7C-D). From 2005, growth of the BE was a result from exclusively cross-shore lengthening of the blowout. The blowout moved landward first (1984-2011) in north easterly direction (Figure 5-7A-D), while in easterly direction since 2011 (Figure 5-7D-E). Since 2013, the blowout decreased in size to about 45,000 m^2 by 2020, though increased temporally up to about 53,000 m^2 in 2017 by increase of area on the seaward side. The mean summer NDVI value stayed around 0.13 within the BE the first ten years after the start of observations in 1984. Between 1994 and 2002 a decrease of the NDVI value to about 0.10 was observed while the BE gradually grew. The NDVI remained its 2002 value up to 2014, and then slightly increased to 0.115 for the last 6 years in the period the BE diminished in size.

The second blowout from the south (2) was also characterized by gradual growth in area (Figure 5-6). This blowout had an open connection to the beach up to 1987, until vegetation growth separated the BE from the beach. During 1984 to 1995, the blowout consisted of two to three disconnected patches of sand. These patches eventually joined to one blowout in 1995 (Figure 5-6A-C). Then, the blowout started to grow relatively constantly at a rate of 2,500 m^2/year to 80,000 m^2 (Figure 5-6). Growth was mainly a result of north easterly movement of the landward side of the BE, while the location of the seaward end of the blowout remained at same location (Figure 5-7C-F). During the growth of the BE, the summer NDVI value within the BE gradually decreased from 0.17 to 0.10 between 1995 and 2010. For five year (2010-2015), the NDVI value remained at 0.10 and then slightly increased to 0.11 in the last five years (2015-2020) (Figure 5-6).

The third blowout from the south (3) was observed to grow slightly up to 1995 and then disappeared completely by 2010 (Figure 5-6). Interestingly, this blowout had already lost the open sandy connection to the beach in 1984 (Figure 5-7A). The growth from 1984 to 1997 was a result of the connection of the two sandy patches which were initially separated. This resulted in a maximum BE of around 38,000 m^2 in 1997. From 1997, the seaward part of the BE started diminishing in area while remaining at its location (Figure 5-7C-D). Concurrently, the landward part moved in north easterly direction. Eventually, the landward part became completely overgrown by vegetation in 2010 (Figure 5-7D). The BE grew at a rate of around 1,300 m^2/year from 1986 to 1997, while decayed faster at a rate of approximately 2,900 m^2/year between 1997 and 2010. Relatively high but constant NDVI values (0.13 till 0.16) were observed during the existence of the third blowout, indicating the continuous presence of partly vegetated pixels within the BE (Figure 5-6). High NDVI values observed since 2010 may be biased by redundant pixels detected as 'blowout', in fact being partly vegetated pixels.

The blowout in the center of the study area (4) appeared for the first time clearly in 1990. Then, it grew stepwise to 2014, after which it started to decay in size (Figure 5-6). The blowout lost an open sandy connection to the beach around 1998. Due to north easterly movement of the landward extremity, the blowout grew till 2014. The BE grew relatively slowly up to 2007 (700 m^2/year), but faster (3,100 m^2/year) from 2007 up to a maximum extent of 34,000 m^2 observed in spring 2013 and 2014 (Figure 5-6). In contrast to the adjacent blowouts, blowout 4 decreased in area due to encroachment of vegetation on the landward side, splitting the blowout into three parts in 2015 (Figure 5-7D-E). The landward part then became completely overgrown with vegetation in late 2019, while the seaward part remained present up to 2020 (Figure 5-7F). Summer mean NDVI values within the BE were relatively high (±0.2) up to 1992 as the BE consisted of a small number of pixels. Then, a relatively large number of pixels was partly covered by vegetation. From 1992 to 2012, the NDVI value decreased gradually till a minimum of 0.10 just before the BE maximized in 2014 (Figure 5-6). From 2013 to 2015, the NDVI increased to 0.13 and remained constant in the last 5 years while the BE continuously decreased (Figure 5-6).

The second blowout from the north (5) was relatively small (12,000 m^2), rectangular shaped and connected to the beach at the start of the study period (Figure 5-6). Up to 1994, the blowout gradually decreased in size (up to around 5,000 m^2) by vegetation colonization, which also detached the sandy surface of the BE from the beach since 1990 (Figure 5-7B). From 1995 to 2013, the blowout enlarged by landward expansion in north easterly direction at a rate of approximately 16 m/year. The seaward extremity remained at the 1995 location up to 2007, thus the blow-out lengthened in the cross-shore direction (Figure 5-7C-D). Between 2007 and 2013, the complete blowout started moving landward and the extent increased by alongshore widening to 50,000 m^2 in the summer of 2013. Since 2013, gradual decrease of the BE to about 35,000 m^2 was observe as a result of vegetation recolonization at the north eastern (seaward) side of the blowout (Figure 5-6; Figure 5-7E). In 2018, a temporal decrease of the BE to 28,000 m^2 was observed, probably related to a sudden increase in the vegetation cover (NDVI value) at the seaward side of the blowout. The mean summer NDVI value within the BE followed the opposite trend of the area of the blowout (Figure 5-6). The NDVI dropped relatively quickly (in 7 years) from 0.22 to 0.11 when the blowout enlarged between 1995 and 2002 (Figure 5-6). Up to 2013, the NDVI value continued decreasing gradually to 0.095. In 2014, the NDVI value increased rapidly to 0.11 and remained at that value till the end of the study period with concurrent gradual decrease of the BE (Figure 5-6).

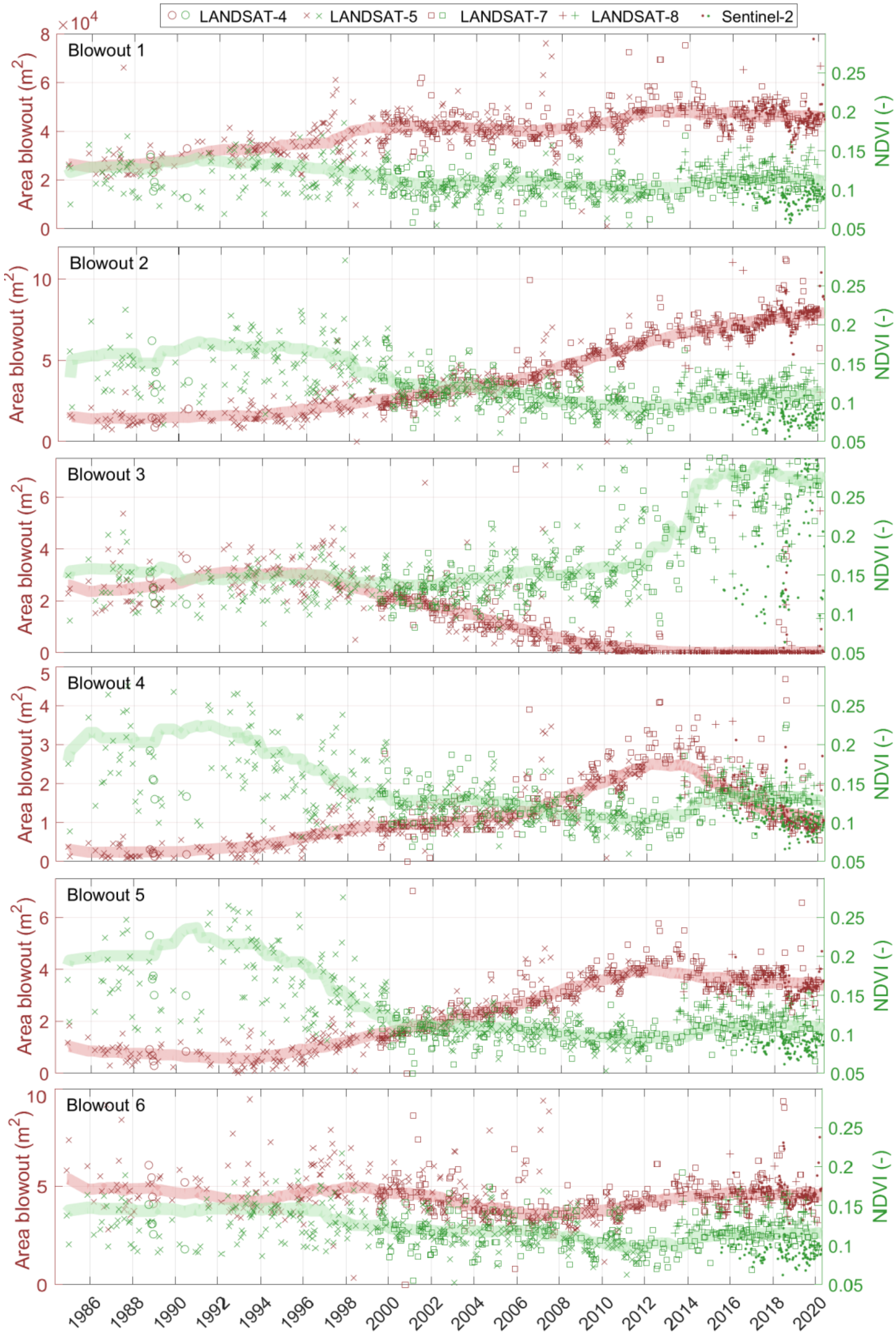

Figure 5-6; Extent of the single blowouts over time with corresponding NDVI value. The shaded lines indicate the 5-year averaged blowout area for all data and 5-year mean NDVI value for the Landsat-5 and Landsat-7 missions over the summer months (May-October) to minimize inter-satellite and seasonal differences. See for all charts: B-6

The most northern blowout (6) initially consisted of two parts between 1984 and 1992, namely a landward decaying part and a seaward growing part. They became clearly isolated in 1986b(Figure 5-7A-B). As the decay was faster than the growth, the area of the blowout decreased from around 53,000 m^2 to 43,000 m^2 during that period (Figure 5-6). The landward part had decayed completely in 1992. The seaward part of the blowout moved eastward at a rate of approximately 7 m/year. Four stages could be defined for the development of the area of the blowout. Firstly, the blowout grew at a rate of approximately 1,450 m^2/year from 33,000 m^2 (in 1985) till 55,000 m^2 (in 2000) by eastward movement (Figure 5-6). Vegetation was observed clearly between the beach and the blowout from 1997, while the orientation of the BE rotated slightly eastward during this period (Figure 5-7A-C). The summer NDVI value within the BE was relatively high (0.15) up to 1997, as partly vegetated pixels were consistently present in the BE (Figure 5-7A-B).Secondly, the BE decreased relatively quickly in size between 2000 and 2007 at a rate of 3,000 m^2/year to about 34,000 m^2 (Figure 5-6). Vegetation recolonized on the seaward side and in the center, splitting the BE in two parts. The NDVI value decreased concurrently to 0.11 (Figure 5-7C-E). Thirdly, the BE grew to around 50,000 m^2 by 2013 at a rate of approximately 2,700 m^2/year, while the NDVI value further decreased (Figure 5-6). Since 2013, the BE fluctuated in size between 40,000 m^2 and 60,000 m^2 as the two parts of the BE occasionally connected (Figure 5-6). The blowout moved slightly eastward while remaining orientated in northeast–southwest direction (Figure 5-7D-F). Simultaneously, the NDVI value increased to near 0.12, mainly because the area in between the sandy patches consisted of partly vegetated pixels (Figure 5-7F).

Consequently, the overall development of the blowouts is characterized by connection to the beach at the start of the study period. The seaward openings to the beach were relatively wide: the beach was broader (up to 150 m) and sandy patches stretched from the beach land inward. From 1990, the blowouts fixated more clearly within the vegetated foredunes and the alongshore width, especially for the part close to the shore, reduced. Gradually, vegetation growth at the seaward side disconnected the blowouts from the beach and decreased the width of the beach (Figure 5-7), indicated by the NDVI value increase on the foredune ridge (Figure 5-8). Most of the blowouts showed a growth in extent while moving land inward in north westerly direction. Concurrently, vegetation recolonization of the former BE was indicated by multiannual increase of the NDVI value (Figure 5-8). For example, in the former region of blowout 1, 3 and 6 in 2002 (Figure 5-8C), the NDVI value continued increasing over a decade up to 2015 (Figure 5-8D-E).

The alongshore width of multiple blowouts (number 1, 2, 5 and 6) grew over the decades, especially on the landward side. Blowout 3 was already disconnected from the beach in 1984. Moreover, the NDVI value increased in the center of blowout 3 in 2002 (Figure 5-8C), after which the blowout completely diminished in size and vegetation had completely overgrown the blowout by 2010 (Figure 5-6). The most northern blowout (6) had a relatively large landward part at the start of the study period (1984), which decayed around 1994. In contrast to the other blowouts, blowout 6 grew in a more eastern direction from 1984 to 2000. Summarizing, the blowouts moved land inward in north westerly direction and got disconnected with the beach. The blowouts then each follow a distinct pattern of growth, decay or stabilization in their bare sand extents.

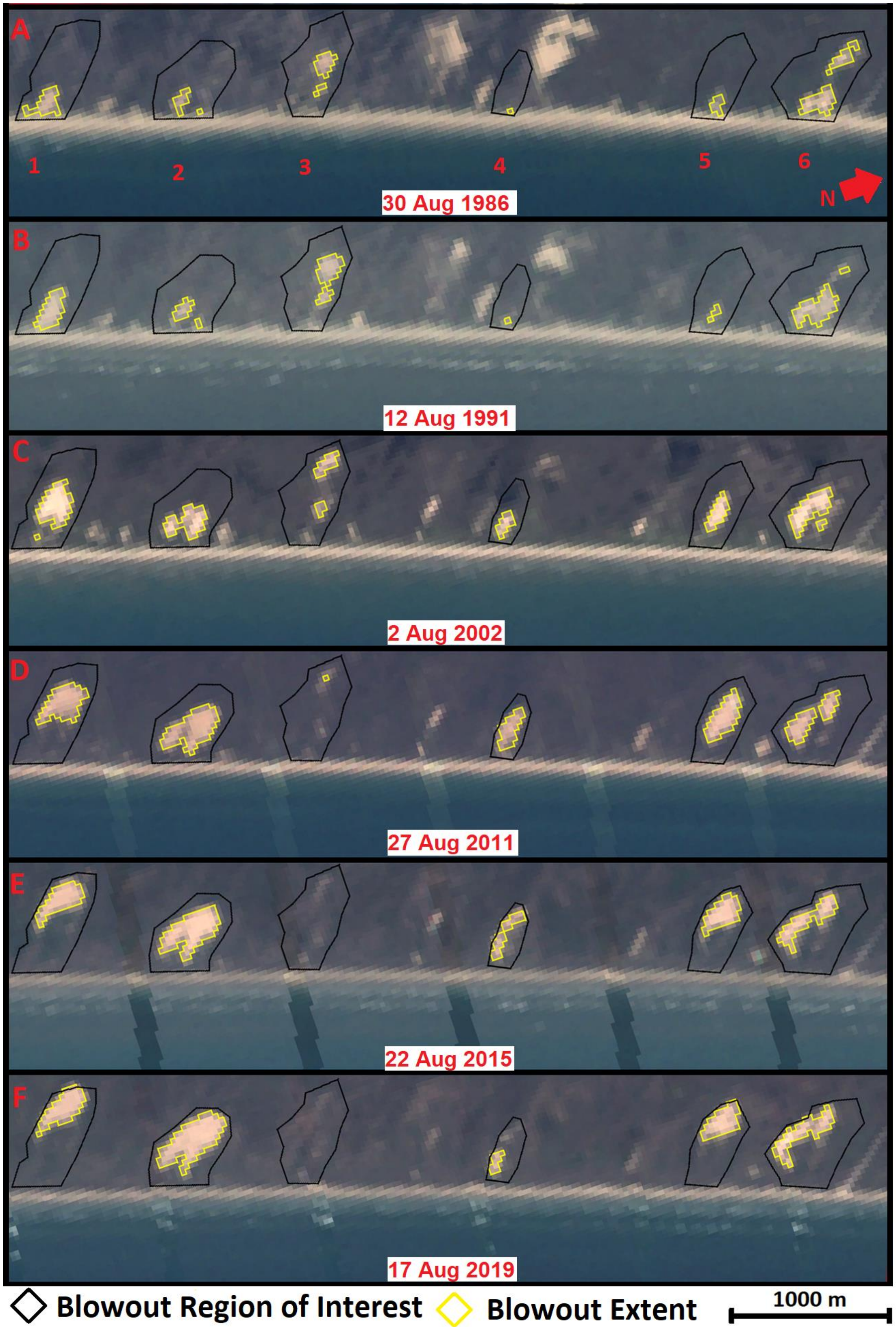

Figure 5-7; Two Landsat 5 (A,B) and 4 Landsat-7 (C,D,E,F) Top-of-the-Atmosphere True Color scenes at Padre Island, corresponding to the NDVI changes displayed in Figure 5-8.

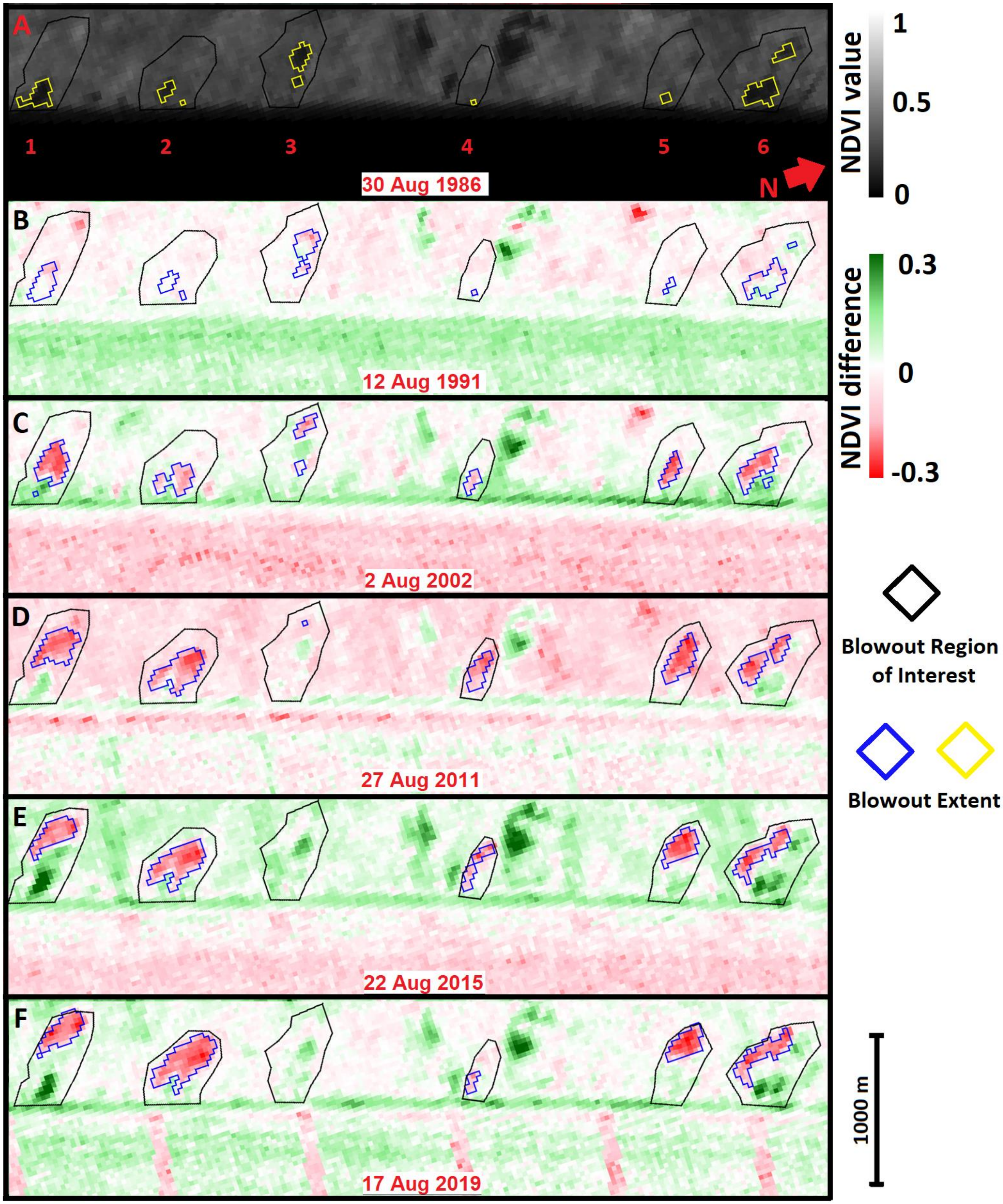

Figure 5-8; A) NDVI value for Landsat-5 image, and B-F) NDVI difference between A. The blowout extent and blowout region of interest are given for each scene. Corresponding True-Color scenes can be found in Figure 5-7 for visual reference.

5.4 Haurvig

5.4.1 Multi-year spatiotemporal development blowouts

The blowout system near Haurvig varied strongly between end summer and end winter aerial extent, and occasionally more than doubled in extent (Figure 5-9). The lowest yearly extent was reached dominantly at the end of the summer (August or September) and grew gradually over the study period. From 1984 to 2019, the BE in the summer increases from around 40.000 m^2 to 160.000 m^2 (Figure 5-9). The growth of the summer BE extent over time was divided into four sections: growth in 1984-2000, stabilization between 2000-2006, growth in 2006-2009 and stabilization in 2009-2020 (Figure 5-9).

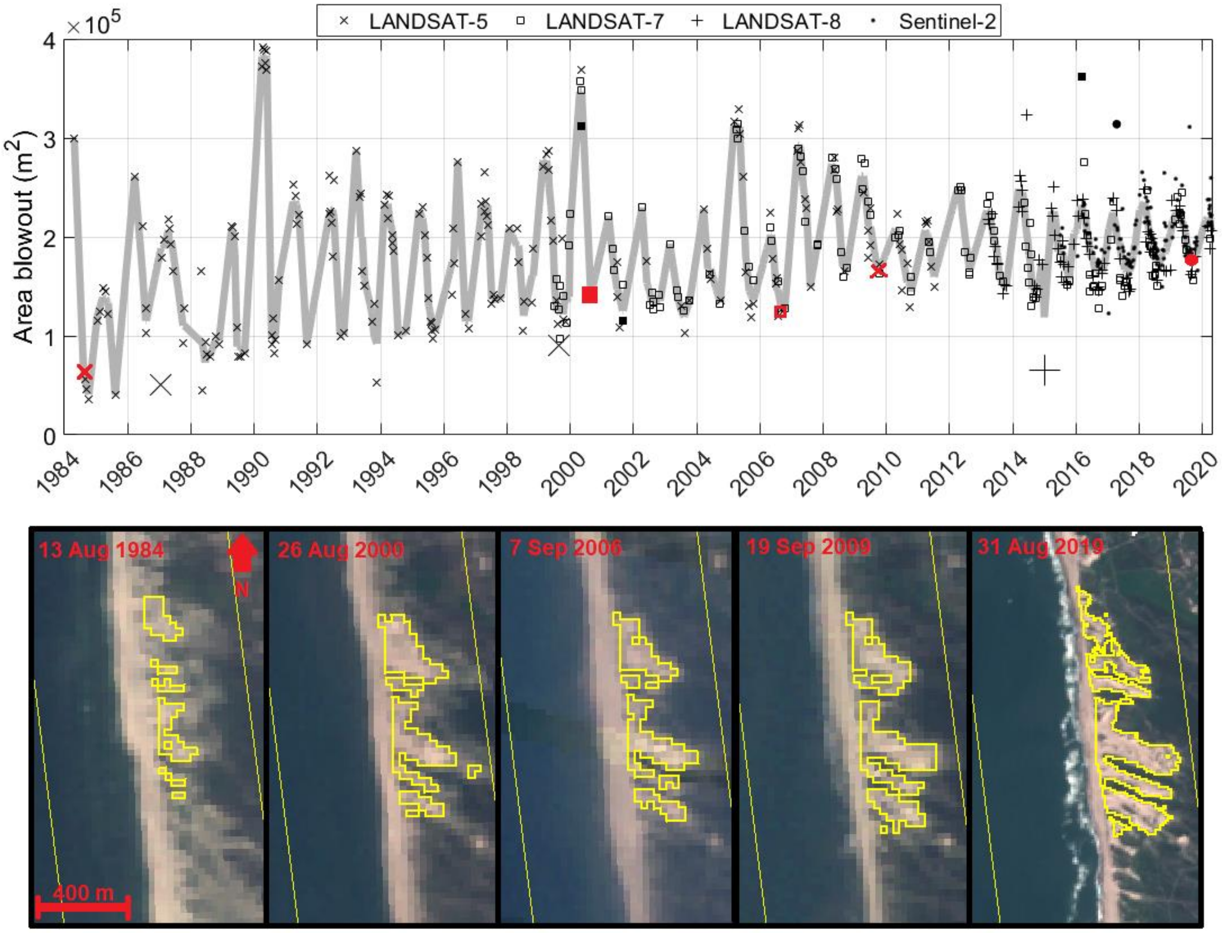

Figure 5-9; The blowout extent over time for the satellites imagery at Haurvig (upper graph). In grey a 3-monthly moving average for the is shown. Discussed example images in Figure 5-10 and Figure 6-4 are highlighted with larger (Landsat-5, Landsat-8 and Sentinel-2) and filled (Landsat-7) symbols. Example images below the graph are highlighted with red symbols. See for all images: B-7

The BE at Haurvig grew with about 5,500 m^2/year from 1984 to 2000 up to an extent of around 130,000 m^2 (Figure 5-9). In 1984, there were no clear blowouts present but the foredune was sporadically non-vegetated. Growth of the blowouts was a result from the development of four to five distinctive blowout throats up to about 300 m land inward (Figure 5-9). The extent grew in east-south-easterly direction. The widest blowout was found in the north of the study area. During the winter, the bare sand areas connected by alongshore widening of the blowouts.

This period was characterized by large winter-summer variations. The seasonal differences of the Blowout Extent (BE) were extreme: at the end of the winter the BE was generally over 200,000 m^2, which meant a two to three times larger area than the preceding or consecutive summer. The maximum annual winter extent generally fluctuated between 200.000 m^2 and 275.000 m^2, though in the years 1990 and 2000 extremely large BE (> 300,000 m^2) were observed (Figure 5-9). For example, in 2000 the BE temporally increased to 370.000 m^2 and thus grew about three times the area than during the preceding and consecutive summer (Figure 5-9). Before and after the occasional increase in 2000, the BE was typically relatively small (< 150,000 m^2) in the summers and consisted of individual separated bare sand areas stretching up to 300 m land inward (Figure 5-10A). During the winter of 2000, the BE grew substantially to over 500 m land inward (Figure 5-10B). The different blowouts connected land inward of the throats. Only three months later, establishment of vegetation had started on the landward side of the BE. The blowouts diminished in size, though the former BE was visually still detectable (Figure 5-10C). One year later, vegetation continued to establish on the landward side and the BE returned to its pre August 1999 conditions (Figure 5-10D).

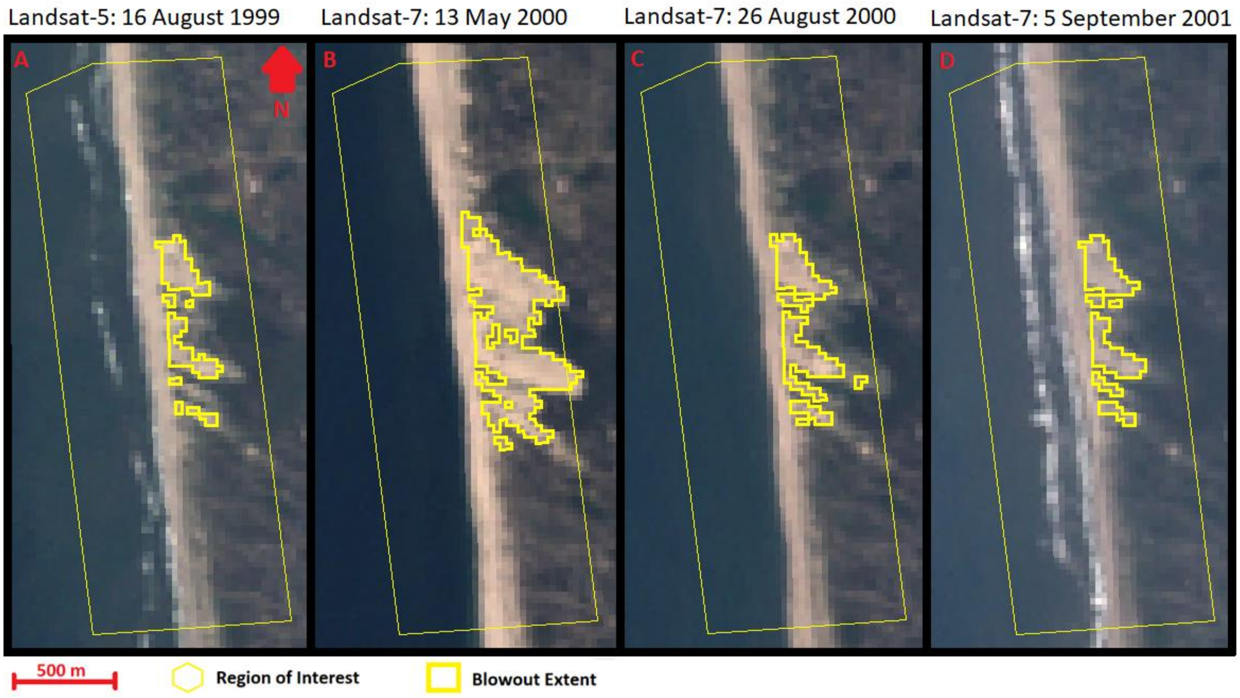

Figure 5-10; Example Landsat imagery of the growth and decay of an extremely large (>300,000 m^2) blowout extent at Haurvig observed in May 2000.

By the year 2000, the blowouts were fixated more into four to five distinct throats grown about 300 m land inward in east-south-easterly direction (Figure 5-9). In the following six years up to 2006, no significant growth of the BE was observed (Figure 5-9). Also, the spatial distribution of the BE did hardly adjust (Figure 5-9). For the winters, only in 2005 there was a large (> 250,000 m^2) increase of the BE, while in the other winters the remained relatively small (< 225,000 m^2). Still, the blowouts frequently connected alongshore during the winter months. Overall, the summer BE from 2000 to 2006 did not change spatially and sustained an extent around 130,000 m^2.

Between 2006 and 2009, the BE grew relatively rapid with about 12,000 m^2/year to around 160,000 m^2 (Figure 5-9). During this period, the BE exceeded three consecutive winters to a relatively large area (> 275,000 m^2), just after another extreme increase (330,000 m^2) in 2005. The southern three blowout throats grew around 100 m in land inward direction with respect to 2006 (Figure 5-9). Also, south of the southern blowout throat, the BE increased by an additional bare sand patch. The northern blowout throat did not increase in landward direction. Instead, a growth of the area was observed on the northern side compared to the BE in 2006 (Figure 5-9).

Since 2009, the BE stabilized at yearly minimal summer BE extent between 150,000 m^2 and 160,000 m^2 (Figure 5-9). Interestingly, the BE during the winter never increased over 250,000 m^2 and thus the seasonal variations in BE were relatively small. The blowouts developed to more distinct adjacent corridors of sand through the vegetated foredune. The southern two adjacent blowouts extended an additional 50 to 100 m land inward and reached a cross-shore length of about 450 m (Figure 5-9). In the south, the patch of bare sand in 2009 developed into a new opening through the foredune. In contrast to the first 25 years of observation, the southern three blowouts became isolated also during the winter months. At the northern end of the study site, three to four corridors through the foredune became detectable (Figure 5-9). Generally, these corridors connected landward into a common depositional lobe stretching about 300 m land inward from the beach. In contrast to the south, there was no further landward movement of the BE in the north (Figure 5-9).

5.4.2 Seasonal variations blowouts

Despite some extreme increases in the BE (e.g. in 1990, 2000 and 2005), the BE fluctuated on a seasonal scale, most constant in the period 2014-2020 (Figure 5-9). The strong seasonal variation in BE continued over the complete study period. Interestingly, the NDVI value within the BE, serving as the proxy for vegetation cover, had the opposite trend as the BE (Figure 5-11). Generally, the NDVI within the BE started rising just before or when the BE started decreasing. Contrary, the NDVI value decreased when the BE started increasing in area (Figure 5-11). Subsequently, the relatively small BE in the summer had an overall higher NDVI value than the relatively large BE during the winters. The blowouts increased in their extents through the months November to March, while during that period the NDVI value dropped with about 0.05. Yearly, a similar increase of the NDVI value was observed between March and September. Accordingly, an interannually stable NDVI value was observed. Surprisingly, a difference of about 0.03 was found between the NDVI value of the Landsat and Sentinel-2 missions. Nevertheless, the pattern of increase and decrease of the NDVI value, thus growth and decay of the vegetation, within the blowouts was similar for both missions.

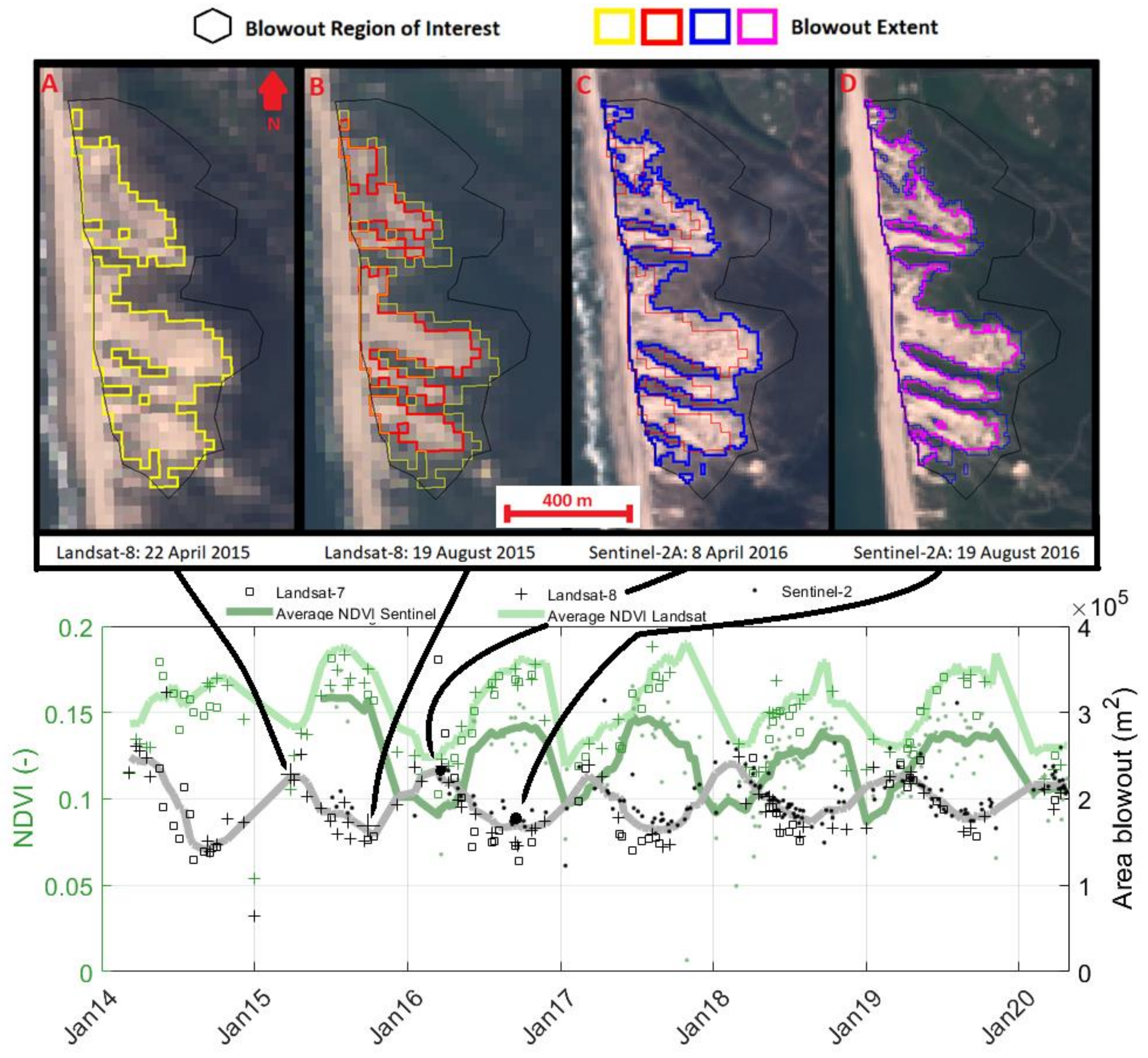

Figure 5-11; Blowout extent and NDVI value within the blowout for the last 6 years of observation at Haurvig. The shaded lines represent 3-monthly averaged values of the NDVI (separately for Landsat and Sentinel sensors) and the blowout extent. Example true color images are added, where thick colored lines indicate the current blowout extent, and the thin line the blowout extent of the previous image.

To examine the spatial distribution of seasonal variation in vegetation cover, the NDVI value was presented using two NDVI difference images (Figure 5-12). Within the BE, the NDVI value grew with 0.033 from April to August 2015 for two Landsat-8 scenes (Figure 5-12A-B) and 0.037 from April to August 2016 for two Sentinel-2 scenes (Figure 5-12CD). Spatially, the increase was not homogenously spread within the BE. For the relatively small BE at the end of the summer, increase in NDVI was basically observed at three places: 1) in the northern and centre blowout throat at the beach entrance, and 2) at the landward extremities of the blowouts. Firstly, in the north and centre blowout throats where the seaward openings were relatively wide showed a large increase of the NDVI within the BE (Figure 5-12). In the northern throat, the increase of the NDVI was significantly up to 150 m land inward (> 0.1). In the centre, the NDVI increase was observed at two distinct patches (Figure 5-12). Interestingly, the three thinner (50-100 m wide) blowout throats (the first, second and fourth from the south) did not show this increase of the NDVI value within the summer BE. Secondly, increase of the NDVI value over the summer was observed in the most landward parts of the BE. Partly, the NDVI increased in the winter BE, though the increase was also observed within the summer BE (Figure 5-12). On the other hand, the area further land inward increased in NDVI with moderate values (±0.15) with respect to the area around the BE and foredunes (> 0.3). This indicates the seasonal dying off and regrowth of vegetation was strongest around the blowouts. Also, the five small (±50 m wide) ridges in between the blowouts showed this remarkable increase in NDVI (Figure 5-12).

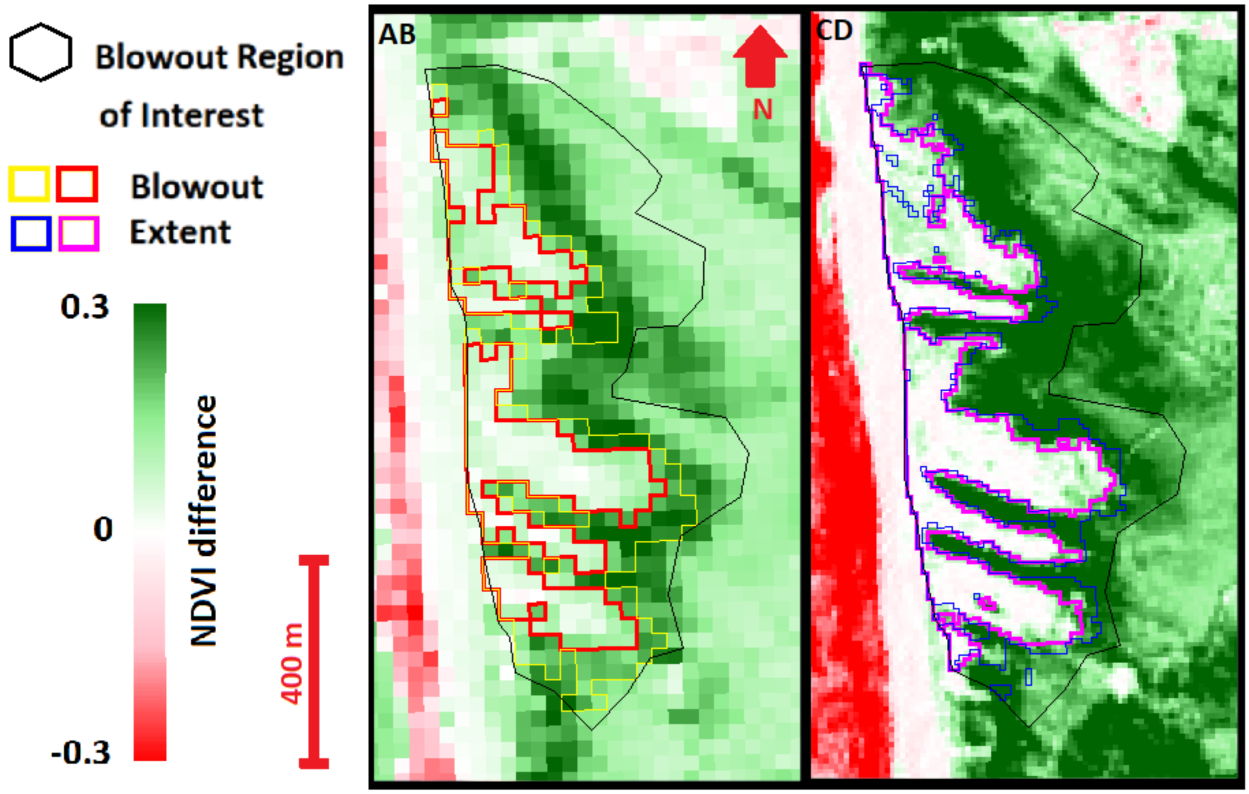

Figure 5-12; NDVI difference between AB) Landsat-8 scenes for 2015, and CD) Sentinel-2A scenes for 2016. The Blowout Extents are overlaid on the NDVI difference images, the thick (thin) colored line corresponds to the end summer (winter) extent (see Figure 5-11 for the true-color representation of the selected scenes).

6 Discussion

6.1 Methodological issues

6.1.1 Selection of cloud free scenes

Generally, clouds and cloud shadows in satellite imagery are either removed by per pixel cloud likelihood algorithms (Foga et al., 2017; Zhu, 2017; USGS, 2018; USGS, 2019) or time series reduction of imagery to statistically likely cloud free pixels (Potapov et al., 2012; Flood, 2013; Griffiths et al., 2013; White et al., 2014; Hermosilla et al., 2015). Here, such methods were found inadequate: the earlier Landsat mission performed badly in coastal areas (Zhu and Helmer, 2018) and a high temporal resolution was desired. Therefore, in this research, scenes were selected based on the statistical likely range of non-cloudy reflectance values.

Although the correct range of pixel values was found empirically, the inter-site and seasonal presence of cloud-free scenes suggest a logical distribution (Table 6-1). Year-round, more imagery was present for the subtropical region Pare Island (65%) than for the temperate climates in northwestern Europe (42-43%), which also was found in the spectral satellite-based observation of cloud cover (Wilson and Jetz, 2016). Obviously, seasonal cloud presence was reflected in the limited number of cloud-free scenes for the winter in Haurvig (18%; Table 6-1). In the generally sunnier spring and summer seasons in northern Europe, about 50% of the imagery were detected as cloud-free.

Table 6-1; Number of scenes passing the cloud filter for the three study areas year-round and per quarter. T stand for total images, F for cloud filtered imagery and P for percentage of scenes passing the cloud filter. Seasonal total scene availability differs as fully cloudy or unilluminated images are more abundant in the winters, which hinders for example georeferencing.

	Zuid-Kennemerland			Padre Island			Haurvig		
	T	F	P	T	F	P	T	F	P
Year-round	787	327	42	1098	712	65	1339	576	43
December - February	153	46	30	238	140	59	231	42	18
March – May	218	122	56	266	147	55	402	218	54
June – August	211	94	45	301	237	79	385	192	50
September – November	205	65	32	293	188	64	321	124	39

A constraint of the applied method is that it is limited to relatively small (< 10 km^2) areas, as the method may be computationally intensive. Moreover, the method is not recommended on local platforms as that requires a bulk of data to be stored locally. Namely, the full timeseries of data required to be cached in memory because that determined the likelihood of any cloud or cloud shadows within the defined Region of Interest (ROI). Nevertheless, performance did well fit within the user-limits of the used cloud computing environment, the Google Earth Engine (GEE). Consequently, the developed cloud-filter may be a valuable framework for selecting cloud-free, spatially small patches of satellite imagery on cloud-computing environments.

6.1.2 Image Endmembers

The method for finding Image Endmembers (IE) relied on the assumption that the most common pixel of a certain index value was representative of the land cover type. IE are preferred methods that account for any inter-scene difference (e.g. platform, atmospheric, seasonal differences), as they are taken from the image itself (Keshava and Mustard, 2002). Nevertheless, it is unlikely that a representative image pixel or group of pixels is composed for 100 percent of one endmember. This may cause errors in the linear inversion to the fractional abundance of the endmembers within the scene (Keshava and Mustard, 2002). In this study, the endmember determination focused on the pixels within the boundary between the sand and vegetated surfaces. Consequently, it was accepted that the endmembers were not representative of the pixels outside the boundary of the blowout and vegetated dune. To show whether the proposed methodology for the definition of endmembers met the assumption that the IE were correctly taken for the Blowout Region of Interest (BROI), the geometric location of the endmembers was calculated throughout the time series of images. Moreover, the Root-Mean-Squared-Error (RMSE) for the LSU was analyzed to deduct if the IE were appropriately chosen.

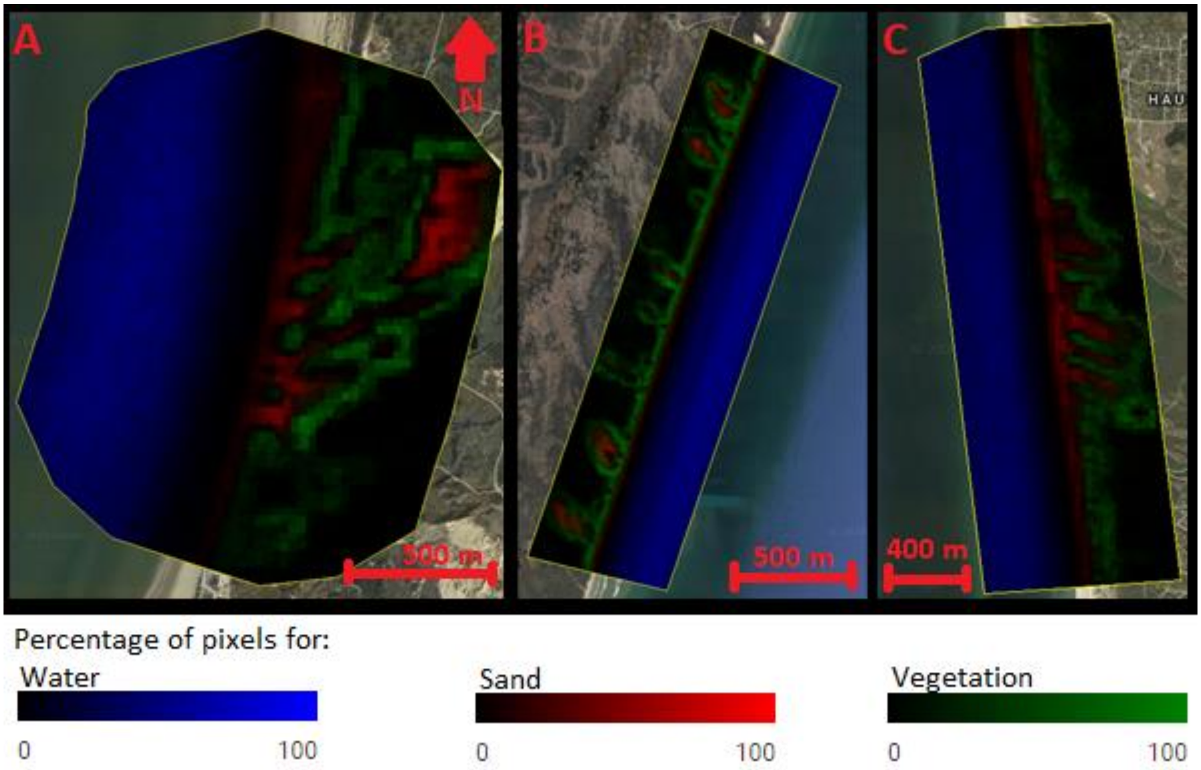

Figure 6-1; Percentage of pixels used as input for the endmembers water, sand and vegetation for the study sites Zuid-Kennemerland (A), Padre Island (B) and Haurvig (C). Images are clipped to the Region of Interest of each study site and presented on top of Google Earth imagery.

The endmembers were independently subtracted from any single scene. Nevertheless, the IE aimed to characterize the spectral signature of the same vegetated, sandy or water surface at any image. Subsequently, the selection of image endmembers was expected to subtract the endmembers from pixels at similar location throughout the time series of imagery, given the natural variability of the area. The water endmember was found spread evenly throughout the deeper sea and diminishing towards the coastline (Figure 6-1). This was expected given the spectral homogenous character of deeper water surfaces. As expected, sandy surfaces and vegetated areas were detected within the blowouts and surrounding to the blowouts (Figure 6-1). In Zuid-Kennemerland, a landward devegetated parabolic dune was included within the Region of Interest (ROI) and frequently used to detect the sand endmember(Figure 6-1A). Although this resulted in the vegetation endmember frequently found further landward of the blowouts, the inclusion of that area was required to ensure there was sufficient sandy surface within the imagery before the excavation of the blowouts in 2013. For Padre Island, the blowouts were shown to migrate significantly northwestward, logically resulting in zones with IE detected for both sand and vegetation (Figure 6-1B, especially in the two most southern blowouts). Most importantly, the dynamic swash zone on the beach and landward locations relatively far from the blowouts were hardly used for the detection of the endmembers.

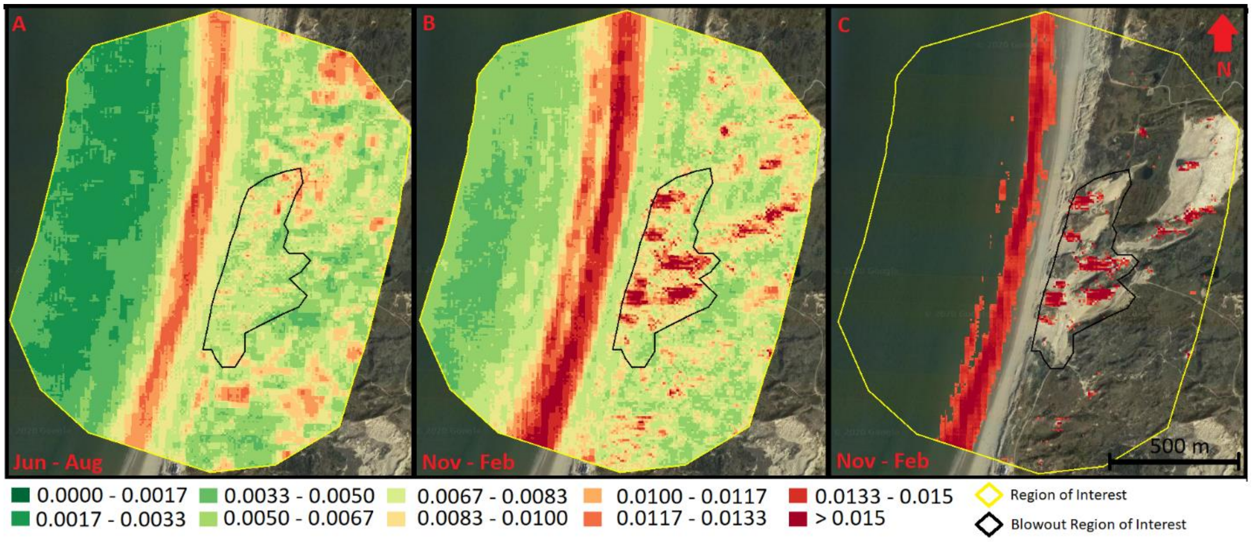

Figure 6-2; Mean Root-Mean-Squared-Error from the non-linear mixture model between 2015 and 2020 for all satellites for the summer (A) and winter (B-C) on top of a Google Earth image (2018). Image C only shows values higher than the mean signal to noise ratio 0.012 for the Sentinel-2A sensor.

Mean Root-Mean-Squared-errors (RMSE) from the non-linear mixture model for the stable period (2015-2020) of the blowout at Zuid-Kennemerland are presented for the winter (November – February) and the summer (June – August) (Figure 6-2). During the summer and winter, significant RMSE values (> 0.012) were observed on the intertidal beach, further land inward and on the north-facing slopes in the blowout. Firstly, the high RMSE values on the intertidal beach indicated the foam resulting from breaking waves. Wave foam is white and has typical visible wavelength values higher than the visibly brightest used endmember sand and therefore did not fit within the defined endmember spectra (Frouin et al., 1996). However, these areas were masked by morphological dilation of the water mask and fell well outside the Blowout Region of Interest (BROI) (Figure 6-2). Secondly, relatively high RMSE values were present further land inward of the BROI during the summers. These areas were found to have greener vegetation than was deduced by the IE close to the blowout. As the IE represented sparse dune vegetation, the greener vegetation fell outside the endmember spectra, resulting in a relative high RMSE (Keshava and Mustard, 2002). However, this greener vegetation was typically not observed close to blowouts and foredunes (Maun, 1998; Schwarz et al., 2019).

Thirdly, high RMSE values were also observed within the BROI during the winters (Figure 6-2). A detailed observation of high (> 0.012) RMSE values (Figure 6-2C) revealed that these values were found on the north-facing slopes of the blowouts and dunes. Landsat and Sentinel-2 imagery are taken between 10 AM and 10:30 AM, giving a relatively high solar zenith angle (Figure 4-19) for especially the higher latitudes. In combination with the relief inside the blowouts, the sun strongly illuminated the north-facing slopes and reflectance values become relatively high (Levin et al., 2006), not enclosed by the endmember spectra. Still, the sand endmember was the endmember with the highest reflectance values (Figure 4-18) and the north-facing slopes were classified as sand by the LMM. Thus, despite relatively high RMSE values within the blowouts, the LMM classified the highly illuminated north-facing slopes correctly as fractional sand cover.

Consequently, the combination of constraining an area by the ROI and Canny edge detection enabled the detection of constant locations of the endmembers. Thus, the IE were adapted for any inter-scene difference, though represented a similar part of either a vegetated, sandy or water surface. Also, analysis of the location of significantly high RMSE values for the LSU model demonstrated that these values did not hindered the classification of the sandy pixels resembling the blowouts.

6.1.3 Validation Satellite imagery

The spatial resolution of the satellite imagery (100 – 900 m^2/pixel) was relatively low compared to the blowouts (10,000 – 400,000 m^2 for the active blowouts), such that omission or inclusion of a single pixel had a relatively large effect on the Blowout Extent. Comparison with high resolution WorldView (2 m) imagery revealed an estimated error of around 12 m^2 and 5 m^2 per pixel for respectively the Landsat (30 m) and Sentinel-2 (10 m) imagery (Ettritch et al., 2018). Subsequently, each single pixel comprised of an error of 1.3 to 5% in comparison with high resolution data. For Zuid-Kennemerland, the UAV images (1 m resolution) detected a Blowout Extent of on average 125,000 m^2, indicating that the blowout consisted of on average 140 Landsat pixels or 1,250 Sentinel-2 pixels. Thus, each single incorrectly detected pixel contributed to a blowout area misestimation of 0.7% (Landsat) or 0.08% (Sentinel-2). The maximum omitted area of the reference UAV imagery by the satellite imagery consisted of 22 Landsat pixels (20,055 m^2) and 87 Sentinel-2 pixels (8,730 m^2) (Figure 5-1). Although the area deviations from the UAV images may be large, the results were still acceptable given the small number of pixels contributing to the error. Also, the zero to negligible area detected as blowout in the years before the excavation at Zuid-Kennemerland provides a good validation of the methodology (Figure 5-2). Subsequently, by using the UAV imagery it is shown that the medium-resolution satellite imagery can provide valuable information, even on a low spatial scale. Although it is inherent in pixel-based analysis that there will remain a difference in the actual geometry of the blowouts and the calculated geometry on 10 to 30 m resolution, the relatively high temporal resolution of the satellite imagery overall gave valuable insights into the development of trough blowouts.

Simultaneously, the difference in area observation by the different spatial resolution of the sensors explained the discrepancy found in NDVI values across the Landsat and Sentinel-2 satellites (Figure 5-4; Figure 5-11). For example, the spatial resolution of the Landsat (30 m) hindered the detection of vegetation in between the individual blowout throats in Zuid-Kennemerland and Haurvig. Subsequently, the lower NDVI values obtained for the Sentinel-2 imagery with respect to the Landsat imagery can be attributed to the difference in spatial resolution. As the spatial resolution increases, the amount of ‘mixed’ (partly sand and vegetation) pixels decreases. Therefore, a lower NDVI value for the Sentinel-2 imagery was observed than for the Landsat imagery. Interestingly, for Haurvig the 10 m resolution Sentinel-2 imagery seemed to overestimate the BE with about 20.000 m^2 with respect to the Landsat-7 and Landsat-

8 30 m resolution imagery (Figure 5-9). Subsequently, the slight increase of the blowout extents during the summers, observed from 2016 to 2020 when the Sentinel-2 sensors were operative, could be biased by the presence of more frequent 10 m resolution imagery. As

6.1.4 Anomalies in the dataset

Unless the efforts for removing redundant imagery within the timeseries of calculated Blowout Extents (BE), there were still outliers in the dataset. Here, examples of the outliers for Zuid-Kennemerland and Haurvig are discussed using seven example images (Figure 6-3; Figure 6-4), while five examples for Padre Island can be found in Figure A-13. Incorrect estimation of the area of the blowout was observed mainly when there was reduced illumination. Generally, illumination reduced when thin clouds such as cirrus or haze covered the study area (Figure 6-3A; Figure 6-4B). In that case, the reflectance of the partly sand-containing pixels was slightly lowered. This lowered the spectral difference between vegetation and sand, resulting in underestimation (Figure 6-3A) or overestimation (Figure 6-4B) of the BE. Poor illumination was also observed for a scene at Haurvig when the sun angle was very low. This resulted in a relatively large part of relief-based shadows within the blowout (Figure 6-4C). As the relief-based shadows were selected as endmembers for sand, the BE was incorrectly determined. Unforeseen snow-covered images were two times present for Haurvig (Figure 6-4A). As the snow cover eliminated the spectral difference between vegetation and sand, vital for the proposed methodology, the BE was occasionally incorrect estimated.

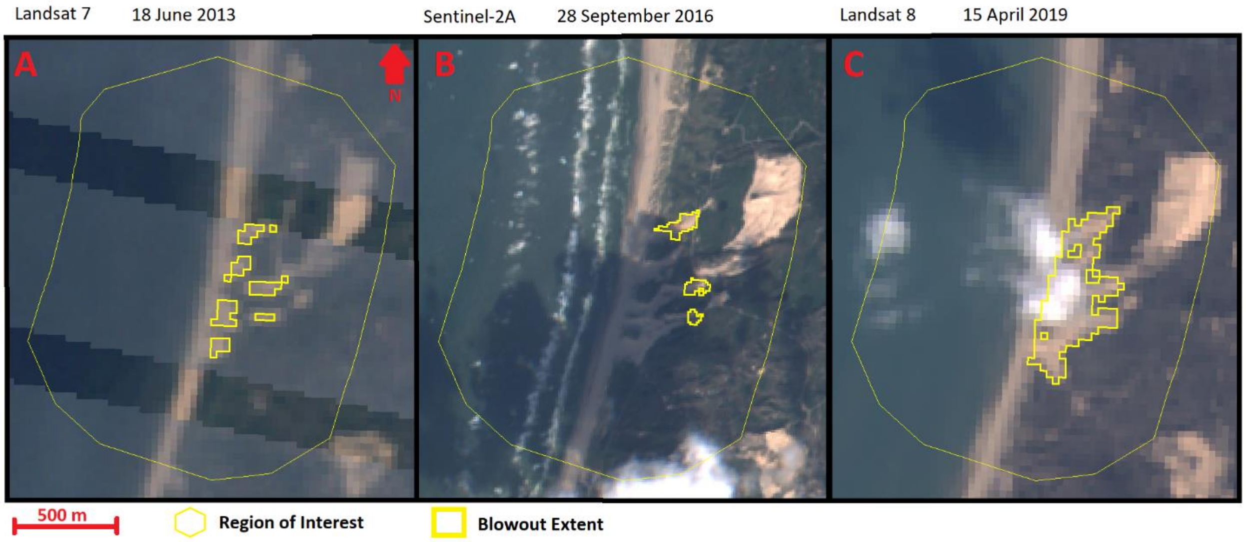

Figure 6-3; Three types of incorrectly estimated Blowout Extents at Zuid-Kennemerland: A) covered by thin clouds, B) covered by cloud shadow, and C) covered by small cloud patches.

Occasionally, images containing clouds or cloud shadows were not correctly removed by the proposed cloud-filter. The BE was overestimated if partly cloud-covered images were not filtered by the cloud-filter (Figure 6-3C; Figure 6-4D). Namely, clouds have relatively high reflectance values and correspond best to the bright beach sand. Cloud shadows also interfered with the detection of the BE. When cloud shadow covered a relatively large part of the study area (Figure 6-3B), this resulted in a large underestimation of the BE as the shadow was included in the water mask. Importantly to note is that the five overestimated outliers from the dataset in the period 2014-2020 were not part of the actual development of the blowout at Haurvig (Figure 5-9) due to cloud cover and poorly illuminated images.

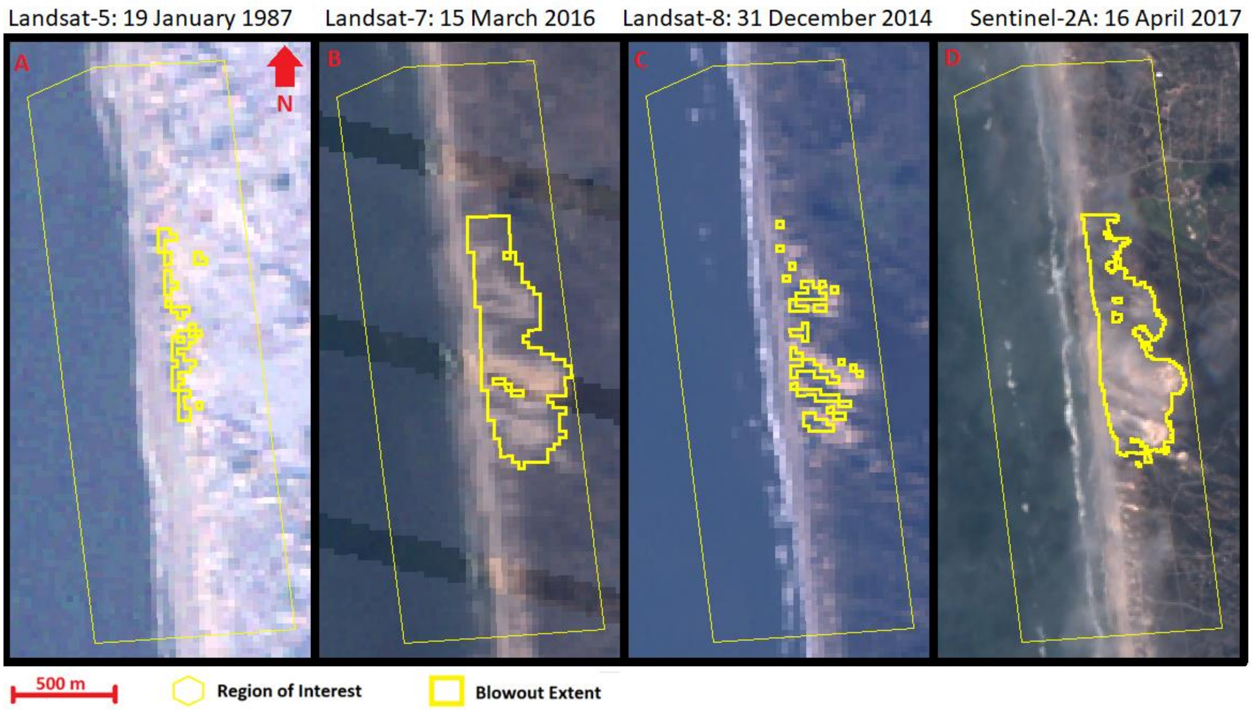

Figure 6-4; Four types of incorrectly estimated Blowout Extents at Haurvig: A) surface covered by snow, B) bad illumination removes clear distinction between sand and vegetation, C) incorrectly sampled endmembers, and D) covered by small cloud patches.

6.1.5 Future spaceborne monitoring

For broader remote sensing applications, the analysis of single scenes showed that seasonal and inter-scene changes may be immense in natural coastal areas. Contrary, the first step in multi-year spectral remote sensing researches is generally 1) the aggregation of annual or multi-year pixels (White et al., 2014; Hermosilla et al., 2015; Robinson et al., 2017), even in this dynamic coastal areas (Carrasco et al., 2019; Marbán et al., 2019), or 2) the selection or collection of annual imagery (Ettritch et al., 2018; Ruessink et al., 2018). As satellite imagery during the winter is generally limited (Table 6-1), the winter state is underrepresented when aggregating pixels on a yearly basis. In-depth singe-scene analysis at Zuid-Kennemerland and Haurvig showed that seasonal effects were strong in the coastal dunes and bare sand area and vegetation cover varied on a monthly scale. Thus, seasonal effects should be considered when low temporal (yearly) resolution remote sensing data, either derived by compositing or from yearly single scenes, are used to describe bare sand development in coastal areas on a multi-year scale. Occasionally, an enormous increase in bare sand area (Haurvig, e.g. in 1990 and 2000) or vegetation cover (Padre Island, e.g. in 2018) was deducted from the single scene methodology. Image compositing will fail to detect the timing of these sporadic events. Consequently, this research demonstrated that single-image analysis should be performed on beforehand to determine if and how image compositing can be done adequately.

Advancement in the resolutions of remote sensing data with simultaneously the increase in technological ability to process data on the cloud provides numerous possible applications for spaceborne monitoring of coastal zones (Klemas, 2010; Yang et al., 2011). For example, an increase in the radiometric resolution of the Landsat-7 (8bit) to Landsat-8 (12bit) enhanced the inter-pixel differences, which was beneficial for the determination of the Otsu threshold and Canny Edge detection. Further advancement of the spatial resolution of Sentinel-2 (10 m) imagery allowed for individual blowout throats detection in Haurvig and Zuid-Kennemerland, as vegetation between the throats could regularly be revealed. Subsequently, the Sentinel-2 database may provide encouraging multi-year blowout development at a relatively high spatial resolution for the coming years as the temporal range of the imagery will extent. Further advancement in (free) worldwide available satellite imagery by for example the Planet (05 m – 5 m resolution) missions provides promising advancement for the detection of blowout development from space (Team, 2017). The deduced methodology can supply a valuable framework for this Planet dataset, though the use of the Shortwave-Infrared band should be replaced appropriately.

A limiting factor during the research is that the used spectral satellite imagery only measures a two-dimensional aerial change in the extent of the blowouts and an indicator for vegetation coverage. However, these areal variations of the sandy surface do not tell whether there is a change in the volumetric balance of the sand. For example, for the Haurvig study site, it was unknown whether the large seasonal sand movement land inward resulted in a yearly accumulated sand budget or whether it was simply a result from seasonal growth and decay of vegetation. Continuous spatial datasets of elevation are required to incorporate the actual spatiotemporal change in sand budget of the system, which could for example be measured for current data using Lidar (Ruessink et al., 2018; Laporte-Fauret et al., 2020). Based on this multi-annual dataset of blowout development, Lidar surveys on a yearly basis are recommended to determine to what degree seasonal fluctuation of blowout extent contributes to the sediment transport of coastal foredune blowouts. To deduce historical blowout development, Ground Penetrating Radar is a promising addition to aerial extent by imagery (González-Villanueva et al., 2011; Jewell et al., 2014). Furthermore, in-situ data, such as wind flow patterns and storm surge events, should be assessed to understand the driving forces of blowout development.

6.2 Development of coastal trough blowouts

6.2.1 Blowout initiation

In the literature, the initiation of foredune trough blowouts has been related to topographic steering and acceleration of wind energy or by locally exposed sand due to the absence of vegetation (Hesp, 2002; Jewell et al., 2017). Moreover, a combination of the previous two triggered by humans can initiate blowout formation. Blowout initiation was observed most clearly at Haurvig. Consistent with the literature, storm surges may have played an important role on blowout initiation by foredune erosion (De Winter et al., 2015; Castelle et al., 2017). At Haurvig, extremely high water levels were observed in 1982 and 1986 (Figure 4-6). This probably triggered the initiation of the blowouts that remained present in the following three decades. Possibly, the blowout initiated by the two storm surges, resulting in relatively far landward protruding and alongshore uniform sandy surfaces (Figure 6-5A). Although no imagery was present before 1984, bare sand areas protruded landward only after the first event in 1984. However, the vegetation recovered quickly in 1985 (Figure 6-5B). After the second storm surge (1986), the locations of the blowouts were stabilized into the foredunes up to three years later and would continue to expand in the following decades (Figure 5-9).

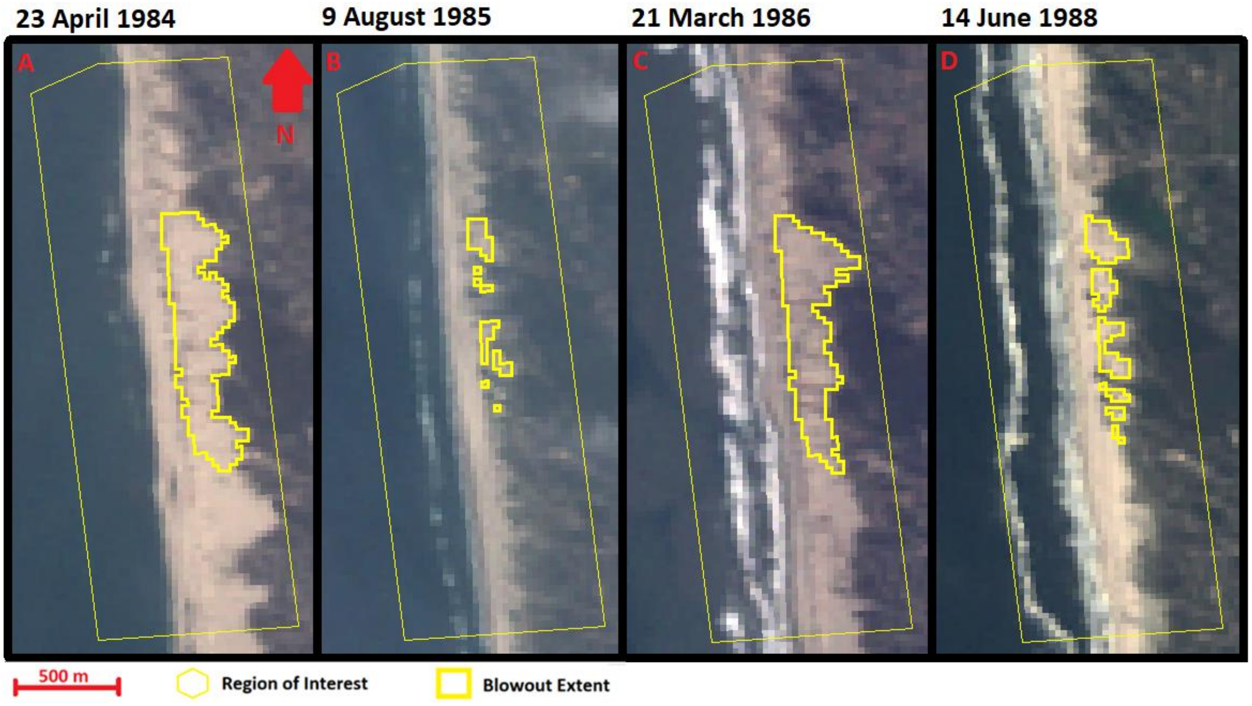

Figure 6-5; Landsat 5 scenes at the start of the study period, showing two times large sandy surfaces protruding land inward just after the winter (A-C) and two times the minor sand extents during the summer shortly after (B-D).

Jewell et al. (2017) mentioned that blowout 4 at Padre Island re-activated during the hurricane Bret in August 1999. However, Figure 5-6 illustrates that this blowout already started to grow in 1990. Possibly, vegetation on the foredune had already been removed locally and triggered the formation of the blowout. Nevertheless, the opening of the throat by hurricane Bret was possibly the trigger for the growth of the blowout extent during 2000-2010. Although the site is hit more often by hurricanes (e.g., Dolly in 2008) hit this part of the US coastline, their impact on blowout initiation or reactivation seems to be small to nonexistent.

6.2.2 Development to full blowout

In line with earlier research, blowouts lengthened and widened during their growing stage (Ruessink et al., 2018; Schwarz et al., 2019). For example, the southern three blowout throats at Haurvig extended over 300 m land inward during the 36-year study period. In Zuid-Kennemerland, the blowouts extended both laterally and land inward in the first year after excavation (Figure 5-2). Although the growth of vegetation on the landward entrance of the blowout is generally linked to closure (Schwarz et al., 2019), results from Padre Island demonstrate that blowout lengthening and widening may continue over decades even though the open and unvegetated connection to the beach was lost. However, Jewell et al. (2017) illustrated with elevation data that the blowouts became increasingly low profile after the connection to the beach was lost.

In agreement with earlier research, the blowouts built out (Zuid-Kennemerland, Haurvig) or transgressed (Padre Island) in the prevailing wind direction (Carter et al., 1990; Hesp and Hyde, 1996; Green et al., 2004). Similarly, as the dominant wind direction was skewed with respect to the shoreline, the blowouts including the depositional lobe developed into a typical skewed orientation (Hesp and Hyde, 1996; Byrne, 1997). Possibly, the deviating easterly movement of the northern blowout (6) at Padre Island was related to a local decrease in vegetation in the early stages of the blowout development (Figure 5-8B). Lengthening of the blowouts in the prevailing wind direction was observed to be higher for blowouts with a relatively narrow width, highlighting the positive feedback from funnelling of wind through the blowout deflation basin (Hesp and Hyde, 1996; Gares and Pease, 2015). For example, the disjointed northern blowout throat at Zuid-Kennemerland expanded more landward than the wider and connected southern blowouts (Figure 5-3). Similarly, the three individual southern blowouts throats expanded further land inward than the wider blowout throat on the northern side of the study area of Haurvig (Figure 5-9).

Strong seasonal expansion (winter) and contraction (summer) of the Blowout Extent (BE) was detected for. Seasonal patterns were stronger the higher latitude of the study site was (i.e. Haurvig had the strongest seasonal variations in BE). There, the seasonal climate differences are more pronounced (Byrne, 1997). Interestingly, the BE maximized in the month just after the winter, highlighting the continuous expansion (contraction) of the BE over the winter (summer) season. For Zuid-Kennemerland, detailed wind velocity measurements were present (Figure 4-4; Figure A-9). There, it was shown that seasonal patterns of the BE were strongly correlated to variations in wind energy. Likely, the BE expanded (contracted) by the concurrent increase (decrease) in potential sand transport by wind. Interestingly, the relatively low energetic wind conditions during the winter of 2016-2017 resulted in a lower increase of the BE over the winter (Figure A-9; Figure 5-2). Subsequently, interannual differences in wind energy may strongly influence the seasonal aerial increase of a blowout. Moreover, strong seasonality of the temperature influences the plant phenology. Presumably, extremely cold winter temperatures at Haurvig triggered vegetation dying off and explained the strong increase of the BE over the winters.

At Haurvig, annually returning variation in BE (about 100,000 m^2) did not explain the episodic large increases (> 200,000 m^2) of the BE. As these events coincided with storm surges (Figure 4-6), it is likely that these storm surges played an important role in the episodic increase of the BE. Possibly, the storm surges locally eroded the foredune and coincided with highly energetic winds. The storm surges had a clear episodic effect by increasing the BE, though longer term increase of the BE corresponded to the period with significant storm surges between 1984 and 2008 (Figure 5-9). Unfortunately, since 2012 no water level measurements were available, but the lack of the occasional significant increase of the blowout suggested that storm surges were not present or sufficiently high. In previous research, overwash and dune scarping during storm surges was generally seen as an event for blowout initiation (Carter et al., 1990; Gares and Nordstrom, 1995; Hesp, 2002). Seldomly, storm surges were included as a major physical disturbance for a blowout reversing the positive feedback of accreting vegetation (Schwarz et al., 2019). Here, results for Haurvig confirm that storm surges indeed may be an important factor for further development and expansion of blowouts.

Besides the natural blowout building process of storm surges, coastal measures possibly also affected the blowout development at Haurvig. Interestingly, the blowout increased during the winter of 2000 during lower water levels than in 2005, but a higher increase of the BE (250,000 m^2) was observed. Probably, the beach nourishment finished in July 1999 temporally increased the sediment availability and aeolian transport into the back dunes.

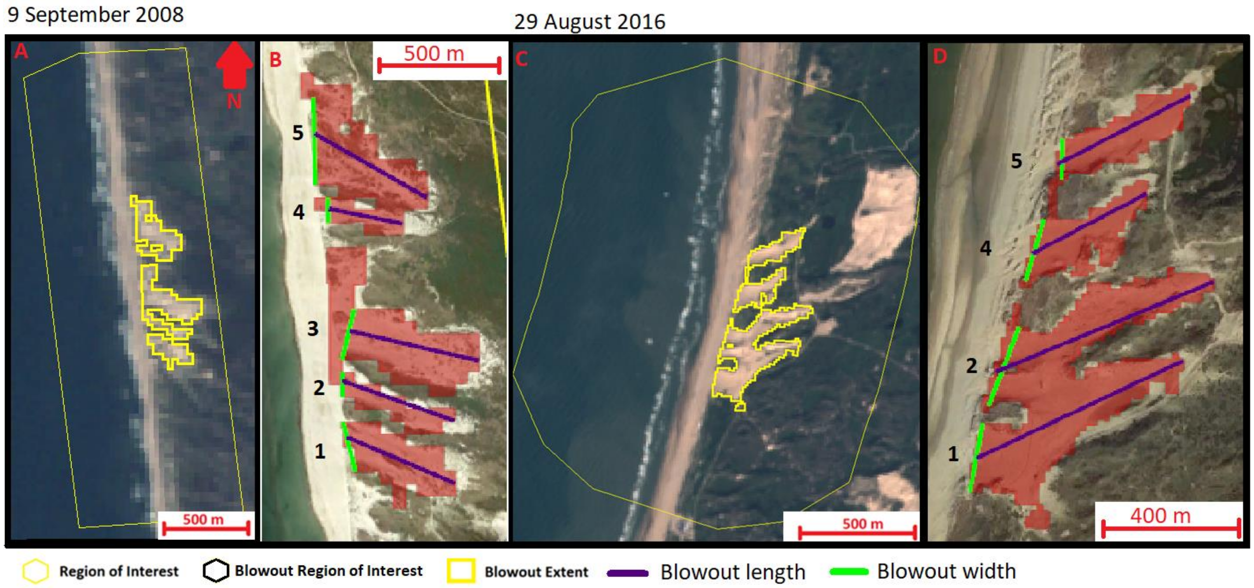

Figure 6-6; Example scenes of A) Landsat-5 at Haurvig in 2008 and C) Sentinel-2A at Zuid-Kennemerland in 2016 with the corresponding blowout extent overlaid on high resolution Google Earth imagery for respectively 2018 (B) and 2019 (D). Estimated blowout length and width are presented with the numbers of the blowout corresponding to the text.

Interestingly, the gradual interannual total increase of the blowout systems at Haurvig (since 2008) and Zuid-Kennemerland (since 2016) seemed to cease (Figure 6-6), despite continuing to fluctuate on a seasonal scale (Figure 5-2; Figure 5-9). To examine this further, the full blowout length and width were estimated from two representative satellite images (Figure 6-6). The assumption was made that the throat width of alongshore adjacent blowouts with a shared depositional lobe was the sum of both. As the used medium resolution imagery hindered individual separation of the deflation basin and the deposition lobe, here the complete size of the sandy part of the blowout was assessed. The individual blowouts that were observed to lengthen most significantly over the observed period (Haurvig 2 and 4, Zuid-Kennemerland 1 and 5), showed a relatively low ratio (< 1:3) between the width of the entrance at the beach and the full blowout length (Table 6-2). Contrary, the blowouts that reached their maximum landward extent by 2008 (Haurvig) and 2016 (Zuid-Kennemerland) were characterized by a higher width to length ratio (> 1:3). Presumably, a low with to length ratio implied that blowouts are in their geomorphological state (Schwarz et al., 2019), where wind acceleration and subsequent erosion is more pronounced present. For higher ratios, this acceleration of wind energy is reduced, explaining the stagnating growth of these blowouts. The ratio of the blowouts corresponded to earlier found ratios of 1:2 to 1:4 between the blowout depositional lobe length and width (Hesp, 2002). For Haurvig and Zuid-Kennemerland, the results suggested that blowouts continue expanding landward up to a certain threshold ratio (around 1:3) between the blowout entrance width and full blowout length. Possibly, these full blowouts extended till a balance between seasonal deposition, erosion and vegetation growth and decay was reached. Once this equilibrium state was reached, blowouts were shown to remain stable for over a decade given that there were no high-energy re-activation events.

Table 6-2; Subtracted blowout length and width and the corresponding ratio between the blowouts for Haurvig (2008) and Zuid-Kennemerland (2016). See Figure 6-6 for the how the length and width were determined spatially.

	Blowout number	throat width (m)	full length (m)	ratio
Haurvig	1	125	285	0.44
	2	60	290	0.21
	3	130	320	0.41
	4	60	180	0.33
	5	210	310	0.68
Zuid-Kennemerland	1	120	400	0.30
	2	150	410	0.37
	4	110	230	0.48
	5	70	260	0.27

6.2.3 Blowout closure

In the current research, only the two-dimensional view of the vegetation and sand was assessed, such that closure of blowouts could only be assessed by vegetation encroachment within or in front of the blowout. In Padre Island, all examined blowouts were shown to move land inward while vegetation colonization separated the beach from the sand blowout. In line with earlier research, vegetation colonization on the foredune, separating the blowout its sand source, was found as a trigger for blowout closure (Gares and Nordstrom, 1995; Hesp, 2002). According to observation by Gares and Nordstrom (1995), the closure was rather a gradual multi-annual process than an abrupt event. Also, the area of blowouts may continue to grow while the sediment volume dynamics of the blowouts had already started decreasing (Jewell et al., 2017), a limitation of the two-dimensional satellite analysis.

In contrast to the four most southern blowouts at Haurvig, the most northern blowout did not expanded landward since 2000 (Figure 5-9). Interestingly, this coincided with seasonal vegetation encroachment at the seaward entrance of that blowout, which was not observed for the other four more southern blowouts (Figure 5-12). In line with earlier research, the growth of vegetation might be stimulated by reduced wind acceleration for relatively wide blowout entrances (Gares and Nordstrom, 1995; Jewell et al., 2017). This suggests that seasonal vegetation encroachment may strongly diminish the wind funneling effect important for the landward expansion of the blowouts. Although yet no sign of reduction of the northern blowout throat was observed, the lack of expansion since 2000 in contrast to the adjacent blowouts may indicate that the northern blowout is in the process of closing. This may also account for the lateral expanding second and third blowout throats (from the south) at Zuid-Kennemerland (Figure 6-6). It is yet unsure what will happen when these throats merge, though the results of Haurvig suggest that eventually seasonal vegetation may colonize the throat and provoke the closure of these blowouts.

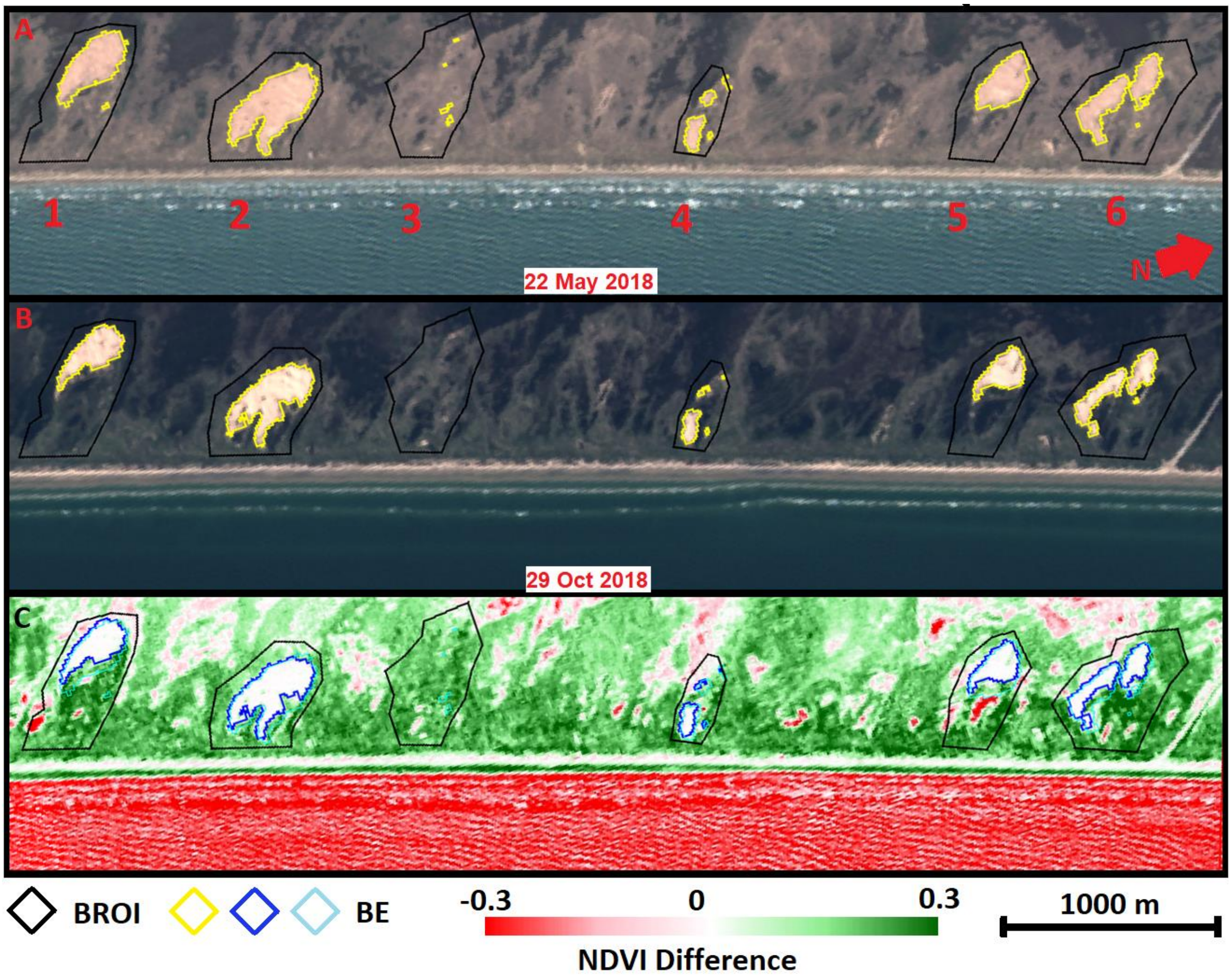

Figure 6-7; Visualization of a short-term NDVI change in 2018. A-B) Sentinel-2A True-colour scene overlaid with the blowout extent and blowout region of interest. C) NDVI difference between B and A, overlaid with the blowout extent of A (light blue) and B (dark blue).

Acceleration of blowout closure was observed when vegetation colonized parts of the blowout. For example, vegetation encroached blowout 4 of Padre Island in 2017. This split up the blowout into two or three sandy patches, possibly related to the increase in distance between the deflation basin and the depositional lobe. The lengthening may have caused a reduction in wind speed within the blowout, resulting in downwind calm conditions where vegetation could settle (Hesp, 2002; Schwarz et al., 2019). Moreover, the relatively large blowouts (1, 4 and 5) decreased temporally between May and October 2018 (Figure 5-6). The blowouts decreased relatively fast by vegetation encroachment on the landward side and only partially regained area about two years later (Figure 5-6). Vegetation growth may have been accelerated by heavy rainfall in the first two weeks of September (The National Weather Service, 2018), when up to 500 mm of rain precipitated (Figure 6-7). Subsequently, rainfall events in arid regions may accelerate the process of blowout closure, likely related to the hysteresis effect between wind power and vegetation cover (Tsoar, 2005; Barchyn and Hugenholtz, 2013).

6.2.4 Blowouts as dynamic coastal dune management

Blowouts are seen as a sustainable coastal measurement that may be beneficial for endemic plant species and enhancement of dune volume (Ruessink et al., 2018; Schwarz et al., 2019). This research analyzed two natural and one man-made blowout systems to examine their spatial extent and vegetation growth. At the excavated blowout system of Zuid-Kennemerland, a relatively high sediment increase observed for the first three years (22,750 m^3/year) was estimated (Ruessink et al., 2018) and corresponded to an aerial increase of 20.000 m^2/year (Figure 5-2). Based on the decadal observations at Haurvig, the blowouts at Zuid-Kennemerland may have reached a similar equilibrium extent where seasonal aerial fluctuations are in balance. No indications for vegetation encroachment within the blowout were observed over the last five years, indicating that the blowouts at Zuid-Kennemerland did not yet show signs of closure. An exception may account when for lateral expansion of adjacent blowouts throats results in merging. This may reduce the funneling wind effect and allow for seasonal vegetation establishment at the seaward entrance, eventually resulting in the closure of the blowout. Overall, it is expected that if the notches remain single openings, the blowouts will remain a corridor for wind acceleration and sediment throughput for over a decade. Nonetheless, integration with topographic measurements is required to validate whether the reached stable blowout position at Zuid-Kennemerland remained a throughput for sediment as observed in the first three years.

Integration of satellite imagery with Ground Penetrating Radar (GPR) surveys is a promising method to deduct decadal scale development of foredune trough blowouts and may additionally predict the sediment increase to aerial development of blowouts (González-Villanueva et al., 2011; Jewell et al., 2014). Additional GPR measurement of, for example, the Haurvig blowout system could reveal the whether the remarkable increase of the BE in 2000 was exaggerated by the beach nourishment applied halfway 1999. Namely, the combination of blowout excavation and beach nourishment may diminish the general encountered loss of nourished sand (de Ruig and Hillen, 1997; Van Duin et al., 2004). This substantially increases the effectiveness of nourishments to current rising sea levels, as that means artificially added sediment would be transported inland by wind instead of lost by wave erosion.

7 Conclusion and Recommendations

In this thesis, a novel approach was developed to monitor relatively large foredune blowouts using the medium resolution spectral data from the freely available Landsat and Sentinel-2 missions. The strength of the method relies on the consecutive spatial reduction of the study area using a combination of an edge detection and Otsu threshold. This resulted in image endmembers which compensated for spectral variations due to for example satellite, atmospheric and seasonal variations. Accordingly, bare sand areas were successfully separated from dune vegetation on an individual image-basis. Errors related to the relative coarse spatial resolution of the satellite imagery compared to the blowouts were inevitable. However, over and underestimations of the blowout area were in balance. On average, the 36 satellite images estimated the area of the blowout within 2% of their actual size. As such, a long and temporal frequent dataset to increase the insights in aerial development of foredune blowouts was developed.

Initiation of foredune blowouts was observed after two consecutive severe storm surges in Haurvig. At Padre Island, blowout initiation was possibly triggered by localized vegetation removal rather than by extreme storm surges by a hurricane. Growth of the area of the blowouts was observed while they have an open connection to the beach. Clearly, blowouts expanded or transgressed land inward in the dominant wind direction. Storm surges at the Haurvig study site, assumed to scarp and erode the front dune ridge, coincided with a strong increase of the blowout extent. Also, the multi-annual growth of the blowout system up to 2008 was probably amplified by occasional storm surges.

Once developed into a full blowout, the aerial extent of blowouts may vary considerably on a seasonal scale. The blowout extent grows during winter, while decreases during the summer. Growth in the winter corresponded to the relatively high energetic wind conditions at Zuid-Kennemerland. Seasonal variations were possibly exaggerated by temperature variations resulting in growth or dying of vegetation, especially for the Zuid-Kennemerland and Haurvig study sites. Interannual variations of the wind energy during the winter were reflected in the blowout extent for Zuid-Kennemerland. The study area Padre Island, located in a relatively arid and warm, lacked strong seasonal variations in blowout extent and was probably more influenced by occasional high-precipitation events. Despite seasonal variations, the blowouts at Haurvig and Zuid-Kennemerland currently seem to have reached a balanced sandy area which may sustain given an open connection to the beach is maintained. Continuous landward expansion of the depositional lobe was found for the blowouts with relatively small entrance widths compared to the full blowout length. The blowouts at Padre Island suggested that once the blowout had transgressed further inland losing its open connection to the beach, closure was initiated. Though the aerial surface of the blowout may continue to increase for multiple years after disconnection from the beach, eventually it leads to disappearance of the blowout.

The construction of the algorithm within the cloud computing platform Google Earth Engine (GEE) allows for worldwide application on numerous study sites. Ongoing analysis of the current study sites is guaranteed as the Landsat and Sentinel-2 missions are scheduled to continue for years. On a broader scale, the dynamic earth’s surface analyzed using satellite imagery on single-image basis demonstrated that popular temporal aggregation methods for satellite imagery should be applied only when seasonal and episodic changes are considered appropriately. An increasing number of higher spatial resolution imagery up to 0.5 m, such as the PLANET missions, provide a growing potential to monitor the blowouts at a higher resolution. The here presented methodology can supply a valuable framework to apply on these relatively new datasets.

Currently, there is a large interest in using artificial foredune blowouts as coastal dune management strategy to bring back aeolian dynamics and increase biodiversity in the back dunes. This research showed that these artificial blowouts remained their size or grew on a multi-annual scale given an open connection to the beach is maintained. Also, growth of the features is stimulated if the throat width remains relatively small compared to the full blowout length. Thus, over widening or growth of vegetation on the seaward side of foredune blowouts should be restrained to maintain the active corridor through the foredune. Future research should include auxiliary data capable of measuring volumes, such LiDAR or Ground Penetrating Radar. This enables the further analysis of seasonal and instantaneous increases of the sand area. Ultimately, this will answer whether the blowout growth and seasonal fluctuations observed for Zuid-Kennemerland and Haurvig was a continuous expansion of the dune elevation or just a local reorganization of the sand and vegetation cover.

References

Anderson J.L., Walker I.J. (2006) Airflow and sand transport variations within a backshore-parabolic dune plain complex: NE Graham Island, British Columbia, Canada (English). Geomorphology, **77** (1-2): 17-34.

Arens, Meijmeijer T., Van Tongeren O. (2015) Noordwestkern: effecten van ingrepen op dynamiek - resultaten monitoring 2013–2015.

Arens, Slings Q., De Vries C.N. (2004) Mobility of a remobilised parabolic dune in Kennemerland, The Netherlands. Geomorphology, **59** (1-4): 175-188.

Arens, Van Kaam-Peters H., Van Boxel J.v. (1995) Air flow over foredunes and implications for sand transport. Earth Surface Processes and Landforms, **20** (4): 315-332.

Arens, Geelen L., Slings Q.L., Wondergem H.E. (2005) Herstel van duinmobiliteit. Naar een nieuw duurzaam beheer, : 2005-2004.

Arens S., Slings Q., Geelen L., Van der Hagen H. (2013) Restoration of dune mobility in the Netherlands. In: Restoration of coastal dunesAnonymous : 107-124. Springer.

Arens S.M., Mulder J.P., Slings Q.L., Geelen L.H., Damsma P. (2013) Dynamic dune management, integrating objectives of nature development and coastal safety: examples from the Netherlands. Geomorphology, **199**: 205-213.

Avis A.M. (1989) A review of coastal dune stabilization in the Cape Province of South Africa. Landscape and Urban Planning, **18** (1): 55-68.

Bagnold R.A. (1954) Experiments on a gravity-free dispersion of large solid spheres in a Newtonian fluid under shear. Proceedings of the Royal Society of London.Series A.Mathematical and Physical Sciences, **225** (1160): 49-63.

Barbosa L.M., Dominguez J. (2004) Coastal dune fields at the Sao Francisco River strandplain, northeastern Brazil: Morphology and environmental controls. Earth Surface Processes and Landforms, **29** (4): 443-456.

Barchyn T.E., Hugenholtz C.H. (2013) Dune field reactivation from blowouts: Sevier Desert, UT, USA (English). Aeolian Research, **11**: 75-84.

Bate G., Ferguson M. (1996) Blowouts in coastal foredunes (English). Landscape and Urban Planning, **34** (3-4): 215-224.

Bennett J., Hails J.R. (1981) Sand movement in the coastal margin of the Coorong, South Australia: 155.

Bongiorno D.L., Bryson M., Dansereau D.G., Williams S.B. (2013) Spectral characterization of COTS RGB cameras using a linear variable edge filter**8660**: 86600N.

Brinkkemper J.A., Christensen D.F., Price T.D., Naus I., Hansen A.B., van Bergeijk V., van de Wetering J., Ruessink B.G., Ernstsen V.B., Aagaard T. (2017) Surf zone morphodynamics during low-moderate energetic condtions; The TASTI field experiment. Proceedings Coastal Dynamics 2017, : 1038-1048.

Byrne M.-. (1997) Seasonal sand transport through a trough blowout at Pinery Provincial Park, Ontario (English). Canadian Journal of Earth Sciences, **34** (11): 1460-1466.

Camara G., Souza R., Pedrosa B., Vinhas L., Monteiro A.M.V., Paiva J., Carvalho M.d., Gattass M. (2000) TerraLib: Technology in support of GIS innovation**2**: 1-8.

Canny J. (1986) A computational approach to edge detection. IEEE Transactions on Pattern Analysis and Machine Intelligence, (6): 679-698.

Cappelen J., Jørgensen B. (1999) Observed Wind Speed and Direction in Denmark - with Climatological Standard Normals, 1961-90. Danish Meteorological Institute, .

Carlson T.N., Ripley D.A. (1997) On the relation between NDVI, fractional vegetation cover, and leaf area index. Remote Sensing of Environment, **62** (3): 241-252.

Carrasco L., O'Neil A.W., Morton R.D., Rowland C.S. (2019) Evaluating combinations of temporally aggregated Sentinel-1, Sentinel-2 and Landsat 8 for land cover mapping with Google Earth Engine. Remote Sensing, **11** (3): 288.

Carter, Wilson P. (1990) The geomorphological, ecological and pedological development of coastal foredunes at Magilligan Point, Northern Ireland. Coastal dunes.Form and processes.John Wiley & Sons, Chichester, : 129-157.

Carter, Hesp P.A., Nordstrom K.F. (1990) Erosional landforms in coastal dunes. Coastal Dunes: form and process, : 217-250.

Casey K.A., K��b A., Benn D.I. (2012) Geochemical characterization of supraglacial debris via in situ and optical remote sensing methods: a case study in Khumbu Himalaya, Nepal. The Cryosphere, **6** (1): 85-100.

Castelle B., Bujan S., Ferreira S., Dodet G. (2017) Foredune morphological changes and beach recovery from the extreme 2013/2014 winter at a high-energy sandy coast (English). Marine Geology, **385**: 41-55.

Chander G., Markham B.L., Helder D.L. (2009) Summary of current radiometric calibration coefficients for Landsat MSS, TM, ETM , and EO-1 ALI sensors. Remote Sensing of Environment, **113** (5): 893-903.

Chander G., Helder D.L., Markham B.L., Dewald J.D., Kaita E., Thome K.J., Micijevic E., Ruggles T.A. (2004) Landsat-5 TM reflective-band absolute radiometric calibration. IEEE Transactions on Geoscience and Remote Sensing, **42** (12): 2747-2760.

Chang C., Plaza A. (2006) A fast iterative algorithm for implementation of pixel purity index. IEEE Geoscience and Remote Sensing Letters, **3** (1): 63-67.

Chen J., Jönsson P., Tamura M., Gu Z., Matsushita B., Eklundh L. (2004) A simple method for reconstructing a high-quality NDVI time-series data set based on the Savitzky–Golay filter. Remote Sensing of Environment, **91** (3-4): 332-344.

Chen X., Chen J., Jia X., Wu J. (2010) Impact of collinearity on linear and nonlinear spectral mixture analysis: 1-4.

Claverie M., Ju J., Masek J.G., Dungan J.L., Vermote E.F., Roger J., Skakun S.V., Justice C. (2018) The Harmonized Landsat and Sentinel-2 surface reflectance data set. Remote Sensing of Environment, **219**: 145-161.

Clinton N. (2017) Otsu's Method for Image Segmentation.

Crist E.P. (1985) A TM tasseled cap equivalent transformation for reflectance factor data. Remote Sensing of Environment, **17** (3): 301-306.

Cui D., Wu Y., Zhang Q. (2010) Massive spatial data processing model based on cloud computing model**2**: 347-350.

Danaher T., Collett L. (2006) Development, optimisation and multi-temporal application of a simple Landsat based water index**29**.

de Ruig J.H., Hillen R. (1997) Developments in Dutch coastline management: Conclusions from the second governmental coastal report. Journal of Coastal Conservation, **3** (2): 203.

De Stoppelaire G.H., Gillespie T.W., Brock J.C., Tobin G.A. (2004) Use of remote sensing techniques to determine the effects of grazing on vegetation cover and dune elevation at Assateague Island National Seashore: impact of horses. Environmental management, **34** (5): 642-649.

De Winter R.C., Gongriep F., Ruessink B.G. (2015) Observations and modeling of alongshore variability in dune erosion at Egmond aan Zee, the Netherlands. Coastal Engineering, **99**: 167-175.

Dech J.P., Maun M.A., Pazner M.I. (2005) Blowout dynamics on Lake Huron sand dunes: Analysis of digital multispectral data from colour air photos (English). Catena, **60** (2): 165-180.

Demetriades-Shah T.H., Steven M.D., Clark J.A. (1990) High resolution derivative spectra in remote sensing. Remote Sensing of Environment, **33** (1): 55-64.

D'Odorico P., Gonsamo A., Damm A., Schaepman M.E. (2013) Experimental evaluation of Sentinel-2 spectral response functions for NDVI time-series continuity. IEEE Transactions on Geoscience and Remote Sensing, **51** (3): 1336-1348.

Donchyts. (2018) Planetary-scale surface water detection from space.

Donchyts, Schellekens J., Winsemius H., Eisemann E., van de Giesen N. (2016) A 30 m resolution surface water mask including estimation of positional and thematic differences using landsat 8, srtm and openstreetmap: a case study in the Murray-Darling Basin, Australia. Remote Sensing, **8** (5): 386.

Drees M., Olff H. (2001) Rabbit grazing and rabbit counting. Coastal dune management Shared experience of European conservation practice.Liverpool University Press, Liverpool, : 86-95.

Drusch M., Del Bello U., Carlier S., Colin O., Fernandez V., Gascon F., Hoersch B., Isola C., Laberinti P., Martimort P. (2012) Sentinel-2: ESA's optical high-resolution mission for GMES operational services. Remote Sensing of Environment, **120**: 25-36.

Earnshaw, Madsen H.T. (2013) COADAPT
- Dune Erosion and safety along the Lodbjerg-Nymindegab Coast Denmark. COADAPT, .

Earnshaw, Madsen H.T., Soerensen P. (2014) ANALYSIS AND MODELLING OF EXTREME LOCALISED DUNE EROSION EVENTS ALONG DENMARK'S NORTH SEA HIGH WATER DUNE BARRIER. Coastal Engineering Proceedings, **1** (34): 26.

Elmore A.J., Mustard J.F., Manning S.J., Lobell D.B. (2000) Quantifying vegetation change in semiarid environments: precision and accuracy of spectral mixture analysis and the normalized difference vegetation index. Remote Sensing of Environment, **73** (1): 87-102.

ESA. (2019) Copernicus Data Acces Policy
2020 (-05-11).

ESA. (2015a) Sentinel-2 User Handbook
. ESA, .

ESA. (2015b) Sentinel-2 User Handbook.

Ettritch G., Bunting P., Jones G., Hardy A. (2018) Monitoring the coastal zone using earth observation: application of linear spectral unmixing to coastal dune systems in Wales. Remote Sensing in Ecology and Conservation, **4** (4): 303-319.

Fisher A., Flood N., Danaher T. (2016) Comparing Landsat water index methods for automated water classification in eastern Australia. Remote Sensing of Environment, **175**: 167-182.

Flood N. (2013) Seasonal composite Landsat TM/ETM images using the medoid (a multi-dimensional median). Remote Sensing, **5** (12): 6481-6500.

Foga S., Scaramuzza P.L., Guo S., Zhu Z., Dilley Jr R.D., Beckmann T., Schmidt G.L., Dwyer J.L., Hughes M.J., Laue B. (2017) Cloud detection algorithm comparison and validation for operational Landsat data products. Remote Sensing of Environment, **194**: 379-390.

Foody G.M., Muslim A.M., Atkinson P.M. (2005) Super-resolution mapping of the waterline from remotely sensed data. International Journal of Remote Sensing, **26** (24): 5381-5392.

Forkuor G., Dimobe K., Serme I., Tondoh J.E. (2018) Landsat-8 vs. Sentinel-2: examining the added value of sentinel-2's red-edge bands to land-use and land-cover mapping in Burkina Faso. GIScience & remote sensing, **55** (3): 331-354.

Franklin G.L., Torres-Freyermuth A., Medellin G., Allende-Arandia M.E., Appendini C.M. (2018) The role of the reef–dune system in coastal protection in Puerto Morelos (Mexico). Natural Hazards and Earth System Sciences, **18** (4): 1247-1260.

Frouin R., Schwindling M., Deschamps P. (1996) Spectral reflectance of sea foam in the visible and nearâ€infrared: In situ measurements and remote sensing implications. Journal of Geophysical Research: Oceans, **101** (C6): 14361-14371.

Gadgil R.L. (2002) Marram grass (Ammophila arenaria) and coastal sand stability in New Zealand. New Zealand Journal of Forestry Science, **32** (2): 165-180.

Gao B. (1996) NDWI—A normalized difference water index for remote sensing of vegetation liquid water from space. Remote Sensing of Environment, **58** (3): 257-266.

Gares P.A. (1992) Topographic changes associated with coastal dune blowouts at island beach state park, New Jersey (English). Earth Surface Processes and Landforms, **17** (6): 589-604.

Gares P.A., Pease P. (2015) Influence of topography on wind speed over a coastal dune and blowout system at Jockey's Ridge, NC, USA (English). Earth Surface Processes and Landforms, **40** (7): 853-863.

Gares P.A., Nordstrom K.F. (1995) A Cyclic Model of Foredune Blowout Evolution for a Leeward Coast: Island Beach, New Jersey (English). Annals of the Association of American Geographers, **85** (1): 1-20.

GEE G.E., Engine. (2019) GEE Data Catalog.

Giles P.T., McCann S.B. (1997) Foredune development on Iles de la Madeleine (Quebec), Atlantis Canada. Canadian Journal of Earth Sciences, **34** (11): 1467-1476.

González-Villanueva, Costas S., Pérez-Arlucea M., Jerez S., Trigo R.M. (2013) Impact of atmospheric circulation patterns on coastal dune dynamics, NW Spain. Geomorphology, **185**: 96-109.

González-Villanueva, Costas S., Duarte H., Pérez-Arlucea M., Alejo I. (2011) Blowout evolution in a coastal dune: Using GPR, aerial imagery and core records (English). Journal of Coastal Research, (SPEC. ISSUE 64): 278-282.

Goodchild M.F. (2007) Citizens as sensors: the world of volunteered geography. GeoJournal, **69** (4): 211-221.

Gorelick N., Hancher M., Dixon M., Ilyushchenko S., Thau D., Moore R. (2017) Google Earth Engine: Planetary-scale geospatial analysis for everyone (English). Remote Sensing of Environment, **202**: 18-27.

Green, Garland G.G., Diab R. (2004) Wind characteristics and blowout formation near mabibi, northern kwazulu-natal (English). South African Geographical Journal, **86** (2): 104-112.

Green, Eastwood M.L., Sarture C.M., Chrien T.G., Aronsson M., Chippendale B.J., Faust J.A., Pavri B.E., Chovit C.J., Solis M. (1998) Imaging spectroscopy and the airborne visible/infrared imaging spectrometer (AVIRIS). Remote Sensing of Environment, **65** (3): 227-248.

Griffiths P., van der Linden S., Kuemmerle T., Hostert P. (2013) A pixel-based Landsat compositing algorithm for large area land cover mapping. IEEE Journal of Selected Topics in Applied Earth Observations and Remote Sensing, **6** (5): 2088-2101.

Hagolle O., Huc M., Villa Pascual D., Dedieu G. (2015) A multi-temporal and multi-spectral method to estimate aerosol optical thickness over land, for the atmospheric correction of FormoSat-2, LandSat, VENµS and Sentinel-2 images. Remote Sensing, **7** (3): 2668-2691.

Hancher M. (2018) Linear Spectral Unmixing in the Google Earth Engine

.

Hansen E., DeVries-Zimmerman S., van Dijk D., Yurk B. (2009) Patterns of wind flow and aeolian deposition on a parabolic dune on the southeastern shore of Lake Michigan (English). Geomorphology, **105** (1-2): 147-157.

Hardy A., Oakes G., Ettritch G. (2020) Tropical Wetland (TropWet) Mapping Tool: The Automatic Detection of Open and Vegetated Waterbodies in Google Earth Engine for Tropical Wetlands. Remote Sensing, **12** (7): 1182.

Hermosilla T., Wulder M.A., White J.C., Coops N.C., Hobart G.W. (2015) An integrated Landsat time series protocol for change detection and generation of annual gap-free surface reflectance composites. Remote Sensing of Environment, **158**: 220-234.

Hesp. (1996) Flow dynamics in a trough blowout (English). Boundary-Layer Meteorology, **77** (3-4): 305-330.

Hesp, Smyth T.A.G. (2016) Jet flow over foredunes. Earth Surface Processes and Landforms, **41** (12): 1727-1735.

Hesp, Pringle A. (2001) Wind Flow and Topographic Steering within a Trough Blowout. Journal of Coastal Research, : 597-601.

Hesp, Hyde R. (1996) Flow dynamics and geomorphology of a trough blowout (English). Sedimentology, **43** (3): 505-525.

Hesp, Hilton M., Konlecher T. (2017) Flow and sediment transport dynamics in a slot and cauldron blowout and over a foredune, Mason Bay, Stewart Island (Rakiura), NZ (English). Geomorphology, **295**: 598-610.

Hesp, Smyth T.A.G., Walker I.J., Gares P.A., Wasklewisz T. (2016) Flow within a trough blowout at Cape Cod (English). Journal of Coastal Research, **1** (75): 288-292.

Hesp P. (2012) Dune Coasts. In: Anonymous : 193-221.

Hesp P. (2002) Foredunes and blowouts: initiation, geomorphology and dynamics (English). Geomorphology (Amsterdam, Netherlands), **48** (1-3): 245-268.

Hesp P. (1988) Morphology, dynamics and internal stratification of some established foredunes in southeast Australia (English). Sedimentary geology, **55** (1-2): 17-41.

Hilton M., Harvey N., Hart A., James K., Arbuckle C. (2006) The impact of exotic dune grass species on foredune development in Australia and New Zealand: A case study of Ammophila arenaria and thinopyrum junceiforme (English). Australian Geographer, **37** (3): 313-334.

Hoonhout B., de Vries S. (2017) Aeolian sediment supply at a mega nourishment. Coastal Engineering, **123**: 11-20.

Hossain M.S., Bujang J.S., Zakaria M.H., Hashim M. (2015) Assessment of Landsat 7 Scan Line Corrector-off data gap-filling methods for seagrass distribution mapping. International Journal of Remote Sensing, **36** (4): 1188-1215.

Houser C., Mathew S. (2011) Alongshore variation in foredune height in response to transport potential and sediment supply: South Padre Island, Texas. Geomorphology, **125** (1): 62-72.

Houser C., Labude B., Haider L., Weymer B. (2013) Impacts of driving on the beach: Case studies from Assateague Island and Padre Island National Seashores. Ocean & Coastal Management, **71**: 33-45.

Houston J. (2008) Management of Natura 2000 habitats. 2130* Fixed coastal dunes with herbaceous vegetation ('grey dunes'). European Commission, .

Huete. (1988) A soil-adjusted vegetation index (SAVI). Remote Sensing of Environment, **25** (3): 295-309.

Hugenholtz. (2010) Topographic changes of a supply-limited inland parabolic sand dune during the incipient phase of stabilization (English). Earth Surface Processes and Landforms, **35** (14): 1674-1681.

Hugenholtz, Levin N., Barchyn T.E., Baddock M.C. (2012) Remote sensing and spatial analysis of aeolian sand dunes: A review and outlook. Earth-Science Reviews, **111** (3-4): 319-334.

Hughes J.N., Annex A., Eichelberger C.N., Fox A., Hulbert A., Ronquest M. (2015) Geomesa: a distributed architecture for spatio-temporal fusion**9473**: 94730F.

Immitzer M., Vuolo F., Atzberger C. (2016) First experience with Sentinel-2 data for crop and tree species classifications in central Europe. Remote Sensing, **8** (3): 166.

Jensen J.R. (2009) Remote sensing of the environment: An earth resource perspective 2/e. Pearson Education India.

Jewell, Houser C., Trimble S. (2017) Phases of blowout initiation and stabilization on Padre Island revealed through ground-penetrating radar and remotely sensed imagery (English). Physical Geography, **38** (6): 556-577.

Jewell, Houser C., Trimble S. (2014) Initiation and evolution of blowouts within Padre Island National Seashore, Texas. Ocean & Coastal Management, **95**: 156-164.

Ji L., Zhang L., Wylie B. (2009) Analysis of dynamic thresholds for the normalized difference water index. Photogrammetric Engineering & Remote Sensing, **75** (11): 1307-1317.

Jungerius P.D. (1984) A simulation model of blowout development (English). Earth Surface Processes and Landforms, **9** (6): 509-512.

Jungerius P.D., van der Meulen F. (1989) The development of dune blowouts, as measured with erosion pins and sequential air photos (English). Catena, **16** (4-5): 369-376.

Kapur J.N., Sahoo P.K., Wong A.K. (1985) A new method for gray-level picture thresholding using the entropy of the histogram. Computer vision, graphics, and image processing, **29** (3): 273-285.

Kay S.M. (1993) Fundamentals of statistical signal processing. Prentice Hall PTR.

Käyhkö J. (2007) Aeolian blowout dynamics in subarctic Lapland based on decadal levelling investigations (English). Geografiska Annaler, Series A: Physical Geography, **89** (1): 65-81.

Kelly A.H. (2016) An Overview of the Coastal Management in the Planning System of New South Wales (NSW), Australia, at the Local Government Level: Is an Environmental Statutory Shift in Planning Law Overdue?**34**: 9-22.

Keshava N., Mustard J.F. (2002) Spectral unmixing. IEEE Signal Processing Magazine, **19** (1): 44-57.

Khattab M.F., Merkel B.J. (2014) Application of Landsat 5 and Landsat 7 images data for water quality mapping in Mosul Dam Lake, Northern Iraq. Arabian Journal of Geosciences, **7** (9): 3557-3573.

Klemas V. (2010) Remote sensing techniques for studying coastal ecosystems: An overview. Journal of Coastal Research, **27** (1): 2-17.

Kocurek G., Townsley M., Yeh E., Havholm K.G., Sweet M.L. (1992) Dune and dune-field development on Padre Island, Texas, with implications for interdune deposition and water-table-controlled accumulation. Journal of Sedimentary Research, **62** (4): 622-635.

Kooijman A.M., Besse M., Haak R., Van Boxtel J.H., Esselink H., ten Haaf C., Nijssen M., Van Til M., Van Turnhout C. (2005) Effectgerichte maatregelen tegen verzuring en eutrofiëring in open droge duinen. Eindrapport fase, **2**.

Kuipers M. (2014) The daring Dutch: restoring the dynamic dunes.

Lane D.M., Scott D., Hebl M., Guerra R., Osherson D., Zimmer H. (2017) An Introduction to Statistics. Rice University.

Laporte-Fauret Q., Castelle B., Marieu V., Bujan S., Michalet R., Rosebery D. (2020) Coastal Dune Morphology Evolution Combining Lidar and UAV Surveys, Truc Vert beach 2011-2019. Journal of Coastal Research, **95** (sp1): 163-167.

Leprieur C., Kerr Y.H., Mastorchio S., Meunier J.C. (2000) Monitoring vegetation cover across semi-arid regions: comparison of remote observations from various scales. International Journal of Remote Sensing, **21** (2): 281-300.

Levin N., Kidron G.J., Ben-Dor E. (2006) The spatial and temporal variability of sand erosion across a stabilizing coastal dune field (English). Sedimentology, **53** (4): 697-715.

Li W., Du Z., Ling F., Zhou D., Wang H., Gui Y., Sun B., Zhang X. (2013) A comparison of land surface water mapping using the normalized difference water index from TM, ETM and ALI. Remote Sensing, **5** (11): 5530-5549.

Loveland T.R., Dwyer J.L. (2012) Landsat: Building a strong future. Remote Sensing of Environment, **122**: 22-29.

Luijendijk A., Hagenaars G., Ranasinghe R., Baart F., Donchyts G., Aarninkhof S. (2018) The State of the World's Beaches. Scientific reports, **8**.

Maini R., Aggarwal H. (2008) Study and comparison of various image edge detection techniques. International journal of image processing (IJIP), **3** (1).

Marbán P.R., Mullinax J.M., Resop J.P., Prosser D.J. (2019) Assessing beach and island habitat loss in the Chesapeake Bay and Delmarva coastal bay region, USA, through processing of Landsat imagery: A case study. Remote Sensing Applications: Society and Environment, **16**: 100265.

Martimort P., Arino O., Berger M., Biasutti R., Carnicero B., Del Bello U., Fernandez V., Gascon F., Greco B., Silvestrin P. (2007) Sentinel-2 optical high resolution mission for GMES operational services: 2677-2680.

Martini P. (1981) Coastal dunes of Ontario: distribution and geomorphology. Géographie physique et Quaternaire, **35** (2): 219-229.

Maun. (1998) Adaptations of plants to burial in coastal sand dunes. Canadian Journal of Botany, **76** (5): 713-738.

Maun M.A. (2009) The biology of coastal sand dunes. Oxford University Press.

McFeeters S.K. (1996) The use of the Normalized Difference Water Index (NDWI) in the delineation of open water features. International Journal of Remote Sensing, **17** (7): 1425-1432.

Menon S.V., Seelamantula C.S. (2014) Robust Savitzky-Golay filters: 688-693.

Mertes L.A., Smith M.O., Adams J.B. (1993) Estimating suspended sediment concentrations in surface waters of the Amazon River wetlands from Landsat images. Remote Sensing of Environment, **43** (3): 281-301.

Meyer G.E., Neto J.C. (2008) Verification of color vegetation indices for automated crop imaging applications. Computers and Electronics in Agriculture, **63** (2): 282-293.

Mir-Gual M., Pons G.X., Martín-Prieto J.Á, Roig-Munar F.X., Rodríguez-Perea A. (2013) Geomorphological and ecological features of blowouts in a western Mediterranean coastal dune complex: A case study of the Es Comú de Muro beach-dune system on the island of Mallorca, Spain (English). Geo-Marine Letters, **33** (2-3): 129-141.

Mulder J.P., Hommes S., Horstman E.M. (2011) Implementation of coastal erosion management in the Netherlands. Ocean & Coastal Management, **54** (12): 888-897.

Muñoz-Vallés S., Cambrollé J. (2015) The threat of native-invasive plant species to biodiversity conservation in coastal dunes. Ecological Engineering, **79**: 32-34.

Murty K.G., Yu F. (1988) Linear complementarity, linear and nonlinear programming. Citeseer.

Myneni R.B., Hall F.G., Sellers P.J., Marshak A.L. (1995) The interpretation of spectral vegetation indexes. IEEE Transactions on Geoscience and Remote Sensing, **33** (2): 481-486.

Nash D.B., Conel J.E. (1974) Spectral reflectance systematics for mixtures of powdered hypersthene, labradorite, and ilmenite. Journal of Geophysical Research, **79** (11): 1615-1621.

Neal A., Roberts C.L. (2001) Internal structure of a trough blowout, determined from migrated ground-penetrating radar profiles (English). Sedimentology, **48** (4): 791-810.

Nolet C., van Puijenbroek M., Suomalainen J., Limpens J., Riksen M. (2018) UAV-imaging to model growth response of marram grass to sand burial: Implications for coastal dune development. Aeolian Research, **31**: 50-61.

Nordstrom K.F., McCluskey J.M. (1985) The effects of houses and sand fences on the eolian sediment budget at Fire Island, New York. Journal of Coastal Research, : 39-46.

Nordstrom K.F., Lampe R., Vandemark L.M. (2000) Reestablishing naturally functioning dunes on developed coasts. Environmental management, **25** (1): 37-51.

Ojeda E., Appendini C.M., Mendoza E.T. (2017) Storm-wave trends in Mexican waters of the Gulf of Mexico and Caribbean Sea. Natural Hazards and Earth System Sciences, **17** (8): 1305-1317.

Orfanidis S.J. (1995) Introduction to signal processing. Prentice-Hall, Inc.

Ormsby J.P., Choudhury B.J., Owe M. (1987) Vegetation spatial variability and its effect on vegetation indices. International Journal of Remote Sensing, **8** (9): 1301-1306.

Otsu N. (1979) A threshold selection method from gray-level histograms. IEEE transactions on systems, man, and cybernetics, **9** (1): 62-66.

Pease P., Gares P. (2013) The influence of topography and approach angles on local deflections of airflow within a coastal blowout (English). Earth Surface Processes and Landforms, **38** (10): 1160-1169.

Pettorelli N., Vik J.O., Mysterud A., Gaillard J., Tucker C.J., Stenseth N.C. (2005) Using the satellite-derived NDVI to assess ecological responses to environmental change. Trends in ecology & evolution, **20** (9): 503-510.

Peyrat J., Fichtner A. (2011) Plant species diversity in dry coastal dunes of the southern Baltic coast. Community ecology, **12** (2): 220-226.

Potapov P.V., Turubanova S.A., Hansen M.C., Adusei B., Broich M., Altstatt A., Mane L., Justice C.O. (2012) Quantifying forest cover loss in Democratic Republic of the Congo, 2000–2010, with Landsat ETM data. Remote Sensing of Environment, **122**: 106-116.

Powell R.L., Roberts D.A., Dennison P.E., Hess L.L. (2007) Sub-pixel mapping of urban land cover using multiple endmember spectral mixture analysis: Manaus, Brazil. Remote Sensing of Environment, **106** (2): 253-267.

Provoost S., Jones M.L.M., Edmondson S.E. (2011) Changes in landscape and vegetation of coastal dunes in northwest Europe: a review. Journal of Coastal Conservation, **15** (1): 207-226.

Provoost S., Van Til M., Deronde B., Knotters A. (2005) Remote sensing of coastal vegetation in the Netherlands and Belgium. Proceedings' Dunes and Estuaries 2005, : 139-149.

Purevdorj T.S., Tateishi R., Ishiyama T., Honda Y. (1998) Relationships between percent vegetation cover and vegetation indices. International Journal of Remote Sensing, **19** (18): 3519-3535.

Pye, Blott S.J. (2017) Evolution of a sediment-starved, over-stabilised dunefield: Kenfig Burrows, South Wales, UK. Journal of coastal conservation, **21** (5): 685-717.

Pye K. (1990) Physical and human influences on coastal dune development between the Ribble and Mersey estuaries, northwest England. In: Coastal dunes: form and processAnonymous : 339-359. Wiley Chichester.

Pye K., Tsoar H. (2008) Aeolian sand and sand dunes. Springer Science & Business Media.

Radoux J., Chomé G., Jacques D., Waldner F., Bellemans N., Matton N., Lamarche C., d'Andrimont R., Defourny P. (2016) Sentinel-2's potential for sub-pixel landscape feature detection. Remote Sensing, **8** (6): 488.

Ren H., Du C., Liu R., Qin Q., Yan G., Li Z., Meng J. (2014) Noise evaluation of early images for Landsat 8 Operational Land Imager. Optics express, **22** (22): 27270-27280.

Richter R. (1997) Correction of atmospheric and topographic effects for high spatial resolution satellite imagery. International Journal of Remote Sensing, **18** (5): 1099-1111.

Riksen M.J., Goossens D., Huiskes H.P., Krol J., Slim P.A. (2016) Constructing notches in foredunes: Effect on sediment dynamics in the dune hinterland. Geomorphology, **253**: 340-352.

Ritchie W. (1972) The evolution of coastal sand dunes. Scottish Geographical Magazine, **88** (1): 19-35.

Rivero O., Astrup S.K., Lassen A. (2018) Shoreface nourishment effects: An analysis of the 2011 nourishment performed at Skodbjerge.

Roberts D.A., Smith M.O., Adams J.B. (1993) Green vegetation, nonphotosynthetic vegetation, and soils in AVIRIS data. Remote Sensing of Environment, **44** (2-3): 255-269.

Robin M., Chapuis J., Lebouvier M. (2011) Remote sensing of vegetation cover change in islands of the Kerguelen archipelago. Polar Biology, **34** (11): 1689.

Robinson N., Allred B., Jones M., Moreno A., Kimball J., Naugle D., Erickson T., Richardson A. (2017) A dynamic Landsat derived normalized difference vegetation index (NDVI) product for the conterminous United States. Remote Sensing, **9** (8): 863.

Rouse Jr J.W., Haas R.H., Schell J.A., Deering D.W. (1973) Monitoring the vernal advancement and retrogradation (green wave effect) of natural vegetation.

Roy D.P., Kovalskyy V., Zhang H.K., Vermote E.F., Yan L., Kumar S.S., Egorov A. (2016) Characterization of Landsat-7 to Landsat-8 reflective wavelength and normalized difference vegetation index continuity. Remote Sensing of Environment, **185**: 57-70.

Ruessink B.G., Arens S.M., Kuipers M., Donker J.J.A. (2018) Coastal dune dynamics in response to excavated foredune notches (English). Aeolian Research, **31**: 3-17.

Ryu J., Won J., Min K.D. (2002) Waterline extraction from Landsat TM data in a tidal flat: a case study in Gomso Bay, Korea. Remote Sensing of Environment, **83** (3): 442-456.

Salman A., Lombardo S., Doody P. (2004) Living with coastal erosion in Europe: Sediment and Space for Sustainability. Eurosion project reports, .

Savitzky A., Golay M.J. (1964) Smoothing and differentiation of data by simplified least squares procedures. Analytical Chemistry, **36** (8): 1627-1639.

Scaramuzza P., Barsi J. (2005) Landsat 7 scan line corrector-off gap-filled product development**16**: 23-27.

Schafer R.W. (2011) What is a Savitzky-Golay filter. IEEE Signal Processing Magazine, **28** (4): 111-117.

Schlingmeier D., Schott J.R. (1998) Resolution enchancement of thermal infrared images via high-resolution class-map and statistical methods**3372**: 100-111.

Schowengerdt R.A. (2006) Remote sensing: models and methods for image processing. Elsevier.

Schwarz C., Brinkkemper J., Ruessink G. (2019) Feedbacks between Biotic and Abiotic Processes Governing the Development of Foredune Blowouts: A Review. Journal of Marine Science and Engineering, **7** (1): 2.

Scott D.W. (2012) Multivariate density estimation and visualization. In: Handbook of computational statisticsAnonymous : 549-569. Springer.

Sellers P.J. (1985) Canopy reflectance, photosynthesis and transpiration. International Journal of Remote Sensing, **6** (8): 1335-1372.

Short A.D., Hesp P.A. (1982) Wave, beach and dune interactions in southeastern Australia (English). Marine Geology, **48** (3-4): 259-284.

Smyth T.A.G., Hesp P.A. (2016) Numerical modelling of turbulent flow structures in a trough blowout (English). Journal of Coastal Research, **1** (75): 328-332.

Smyth T.A.G., Jackson D., Cooper A. (2014) Airflow and aeolian sediment transport patterns within a coastal trough blowout during lateral wind conditions (English). Earth Surface Processes and Landforms, **39** (14): 1847-1854.

Smyth T.A.G., Jackson D.W.T., Cooper J.G. (2013) Three dimensional airflow patterns within a coastal trough-bowl blowout during fresh breeze to hurricane force winds (English). Aeolian Research, **9**: 111-123.

Somers B., Asner G.P., Tits L., Coppin P. (2011) Endmember variability in spectral mixture analysis: A review. Remote Sensing of Environment, **115** (7): 1603-1616.

Song C., Woodcock C.E., Seto K.C., Lenney M.P., Macomber S.A. (2001) Classification and change detection using Landsat TM data: when and how to correct atmospheric effects?. Remote Sensing of Environment, **75** (2): 230-244.

Starr C., Evers C., Starr L. (2010) Biology: concepts and applications. Cengage Learning.

Sturges H.A. (1926) The choice of a class interval. Journal of the american statistical association, **21** (153): 65-66.

Taylor E.B., Gibeaut J.C., Yoskowitz D.W., Starek M.J. (2015) Assessment and monetary valuation of the storm protection function of beaches and foredunes on the Texas coast. Journal of Coastal Research, **31** (5): 1205-1216.

Team P. (2017) Planet application program interface: In space for life on Earth. San Francisco, CA, **2017**: 40.

Teillet P.M., Barker J.L., Markham B.L., Irish R.R., Fedosejevs G., Storey J.C. (2001) Radiometric cross-calibration of the Landsat-7 ETM and Landsat-5 TM sensors based on tandem data sets. Remote Sensing of Environment, **78** (1-2): 39-54.

The National Weather Service. (2018) South Texas Heavy Rainfall - September 2-16, 2018**2020** (13-07-).

Thomsen M., Astrup S.K., Lassen A. (2018) Building with Nature:
Systems Description of
Skodbjerge.

Tinley K.L. (1985) Coastal dunes of South Africa. National Scientific Programmes Unit: CSIR.

Tobias O.J., Seara R. (2002) Image segmentation by histogram thresholding using fuzzy sets. IEEE Transactions on Image Processing, **11** (12): 1457-1465.

Torres-Sánchez J., López-Granados F., Peña J.M. (2015) An automatic object-based method for optimal thresholding in UAV images: Application for vegetation detection in herbaceous crops. Computers and Electronics in Agriculture, **114**: 43-52.

Tsoar H. (2005) Sand dunes mobility and stability in relation to climate. Physica A: Statistical Mechanics and its Applications, **357** (1): 50-56.

Tuxen K.A., Schile L.M., Kelly M., Siegel S.W. (2008) Vegetation colonization in a restoring tidal marsh: A remote sensing approach. Restoration Ecology, **16** (2): 313-323.

USGS. (2019a) LANDSAT 8 (L8)
DATA USERS HANDBOOK.

USGS. (2019b) Landsat 7 User Handbook
.

USGS. (2019c) February 13, 2019 - New Landsat Level-3 Products Released.

USGS. (2019d) Landsat 8 surface reflectance code (LaSRC) product.

USGS. (2018a) Landsat 4–7 Surface Reflectance (LEDAPS) Product Guide. USGS: Sioux Falls, SD, USA, .

USGS. (2018b) Landsat Collections (English). Fact Sheet, : 2.

USGS. (2001) Science Data Users Handbook. http://landsathandbook.gsfc.nasa.gov/inst_cal/prog_sectS_2.html, .

USGS. (1984) Landsat 4 Data Users Handbook.

Van Boxel J.H., Jungerius P.D., Kieffer N., Hampele N. (1997) Ecological effects of reactivation of artificially stabilized blowouts in coastal dunes (English). Journal of Coastal Conservation, **3** (1): 57-62.

Van Der Meer. (1999) Iterative spectral unmixing (ISU). International Journal of Remote Sensing, **20** (17): 3431-3436.

Van der Meer, De Jong S.M. (2011) Imaging spectrometry: basic principles and prospective applications. Springer Science & Business Media.

Van Duin M., Wiersma N.R., Walstra D., Van Rijn L.C., Stive M. (2004) Nourishing the shoreface: observations and hindcasting of the Egmond case, The Netherlands. Coastal Engineering, **51** (8-9): 813-837.

Van Koningsveld M., Mulder J.P.M. (2004) Sustainable coastal policy developments in the Netherlands. A systematic approach revealed. Journal of Coastal Research, : 375-385.

Vermote E.F., Kotchenova S. (2008) Atmospheric correction for the monitoring of land surfaces. Journal of Geophysical Research: Atmospheres, **113** (D23).

Vimpere L., Kindler P., Castelltort S. (2019) Chevrons: Origin and relevance for the reconstruction of past wind regimes. Earth-Science Reviews, .

Wand M.P. (1997) Data-based choice of histogram bin width. The American Statistician, **51** (1): 59-64.

Wang P., Briggs T.M.R. (2015) Storm-Induced morphology changes along barrier islands and poststorm recovery. In: Coastal and Marine Hazards, Risks, and DisastersAnonymous : 271-306. Elsevier.

Wegener M. (1990) Destriping multiple sensor imagery by improved histogram matching. International Journal of Remote Sensing, **11** (5): 859-875.

Weise B.R., White W.A. (1980) Padre Island National Seashore: A guide to the geology, natural environments, and history of a Texas barrier island. Bureau of Economic Geology, University of Texas at Austin.

Weszka J.S. (1978) A survey of threshold selection techniques. Computer graphics and Image processing, **7** (2): 259-265.

White J.C., Wulder M.A., Hobart G.W., Luther J.E., Hermosilla T., Griffiths P., Coops N.C., Hall R.J., Hostert P., Dyk A. (2014) Pixel-based image compositing for large-area dense time series applications and science. Canadian Journal of Remote Sensing, **40** (3): 192-212.

Whitman R.T., Park M.B., Ambrose S.M., Hoel E.G. (2014) Spatial indexing and analytics on Hadoop: 73-82.

Wilson A.M., Jetz W. (2016) Remotely sensed high-resolution global cloud dynamics for predicting ecosystem and biodiversity distributions. PLoS biology, **14** (3): e1002415.

Woodcock C.E., Allen R., Anderson M., Belward A., Bindschadler R., Cohen W., Gao F., Goward S.N., Helder D., Helmer E. (2008) Free access to Landsat imagery. Science, **320** (5879): 1011.

Wright L.D., Short A.D. (1984) Morphodynamic variability of surf zones and beaches: a synthesis. Marine Geology, **56** (1-4): 93-118.

Xu. (2006) Modification of normalised difference water index (NDWI) to enhance open water features in remotely sensed imagery. International Journal of Remote Sensing, **27** (14): 3025-3033.

Xu D., Guo X. (2014) Compare NDVI extracted from Landsat 8 imagery with that from Landsat 7 imagery. American Journal of Remote Sensing, **2** (2): 10-14.

Yang, Guan C., Hasi E. (2017) Dynamic Changes of Typical Blowouts Based on High-Resolution Data: A Case Study in Hulunbuir Sandy Land, China (English). Mathematical Problems in Engineering, **2017**.

Yang, Yu M., Hu F., Jiang Y., Li Y. (2017) Utilizing cloud computing to address big geospatial data challenges. Computers, Environment and Urban Systems, **61**: 120-128.

Yang, Li M., Liu Y., Cheng L., Duan Y., Zhou M. (2014) River delineation from remotely sensed imagery using a multi-scale classification approach. IEEE J.Sel.Top.Appl.Earth Obs.Remote Sens, **7**: 4726-4737.

Yang, Goodchild M., Huang Q., Nebert D., Raskin R., Xu Y., Bambacus M., Fay D. (2011) Spatial cloud computing: how can the geospatial sciences use and help shape cloud computing?. International Journal of Digital Earth, **4** (4): 305-329.

Yin G., Mariethoz G., McCabe M.F. (2017) Gap-filling of landsat 7 imagery using the direct sampling method. Remote Sensing, **9** (1): 12.

Yokota T., Kobayashi A., Uda T., Serizawa M., Katsuki A., Noshi Y. (2018) Model for predicting formation of blowout on coastal sand dune using cellular automaton method (English). Proceedings of the 9th International Conference on APAC 2017, (213039): 572-583.

Young N.E., Anderson R.S., Chignell S.M., Vorster A.G., Lawrence R., Evangelista P.H. (2017) A survival guide to Landsat preprocessing. Ecology, **98** (4): 920-932.

Yu J., Wu J., Sarwat M. (2015) Geospark: A cluster computing framework for processing large-scale spatial data: 70.

Zhang H.K., Roy D.P., Yan L., Li Z., Huang H., Vermote E., Skakun S., Roger J. (2018) Characterization of Sentinel-2A and Landsat-8 top of atmosphere, surface, and nadir BRDF adjusted reflectance and NDVI differences. Remote Sensing of Environment, **215**: 482-494.

Zhu. (2017) Change detection using landsat time series: A review of frequencies, preprocessing, algorithms, and applications. ISPRS Journal of Photogrammetry and Remote Sensing, **130**: 370-384.

Zhu, Helmer E.H. (2018) An automatic method for screening clouds and cloud shadows in optical satellite image time series in cloudy regions. Remote Sensing of Environment, **214**: 135-153.

A. Additional Figures

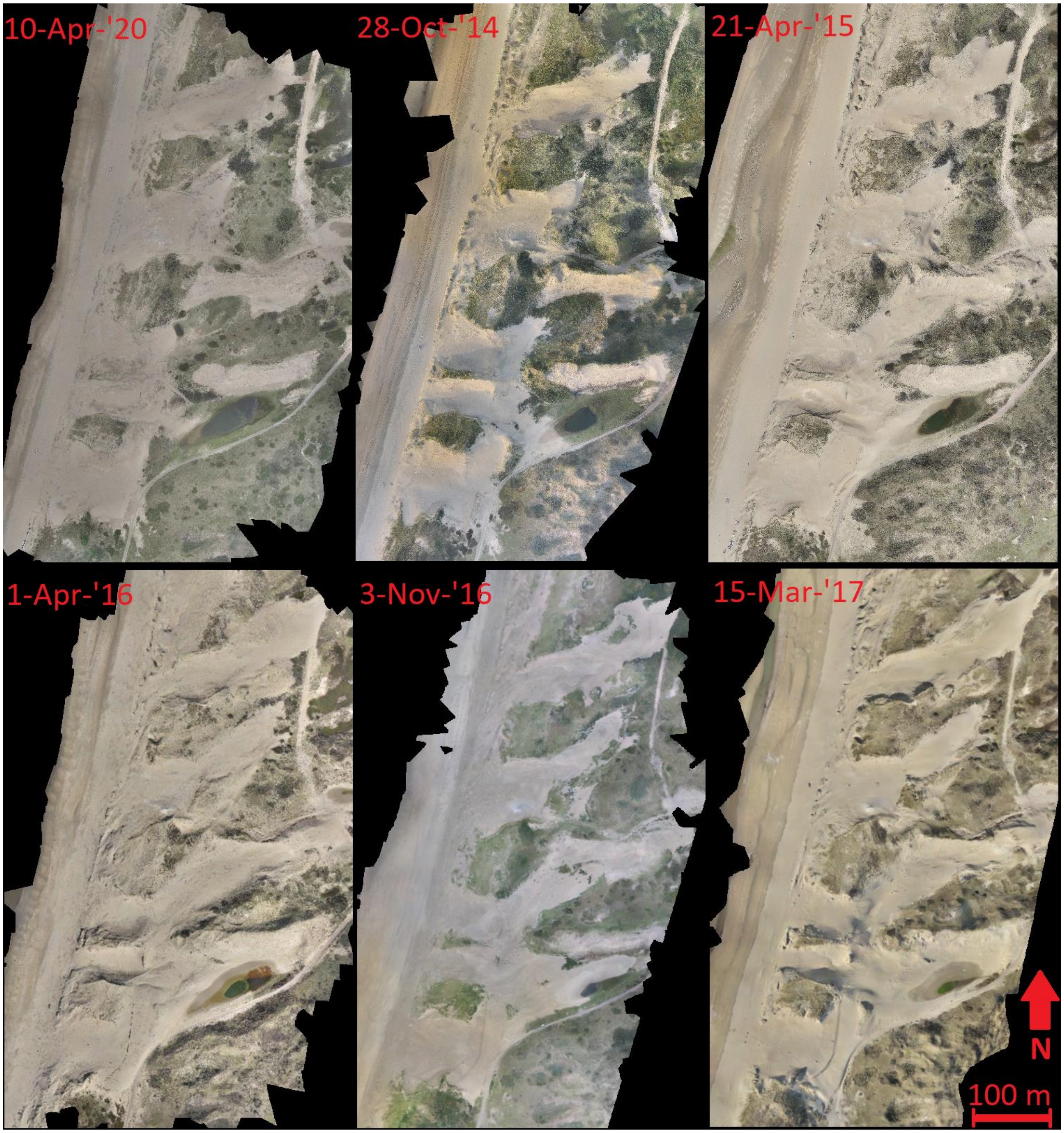

Figure A-1; Unmanned Air Vehicle images taken Zuid-Kennemerland from 2014 till 2017 and used throughout this study.

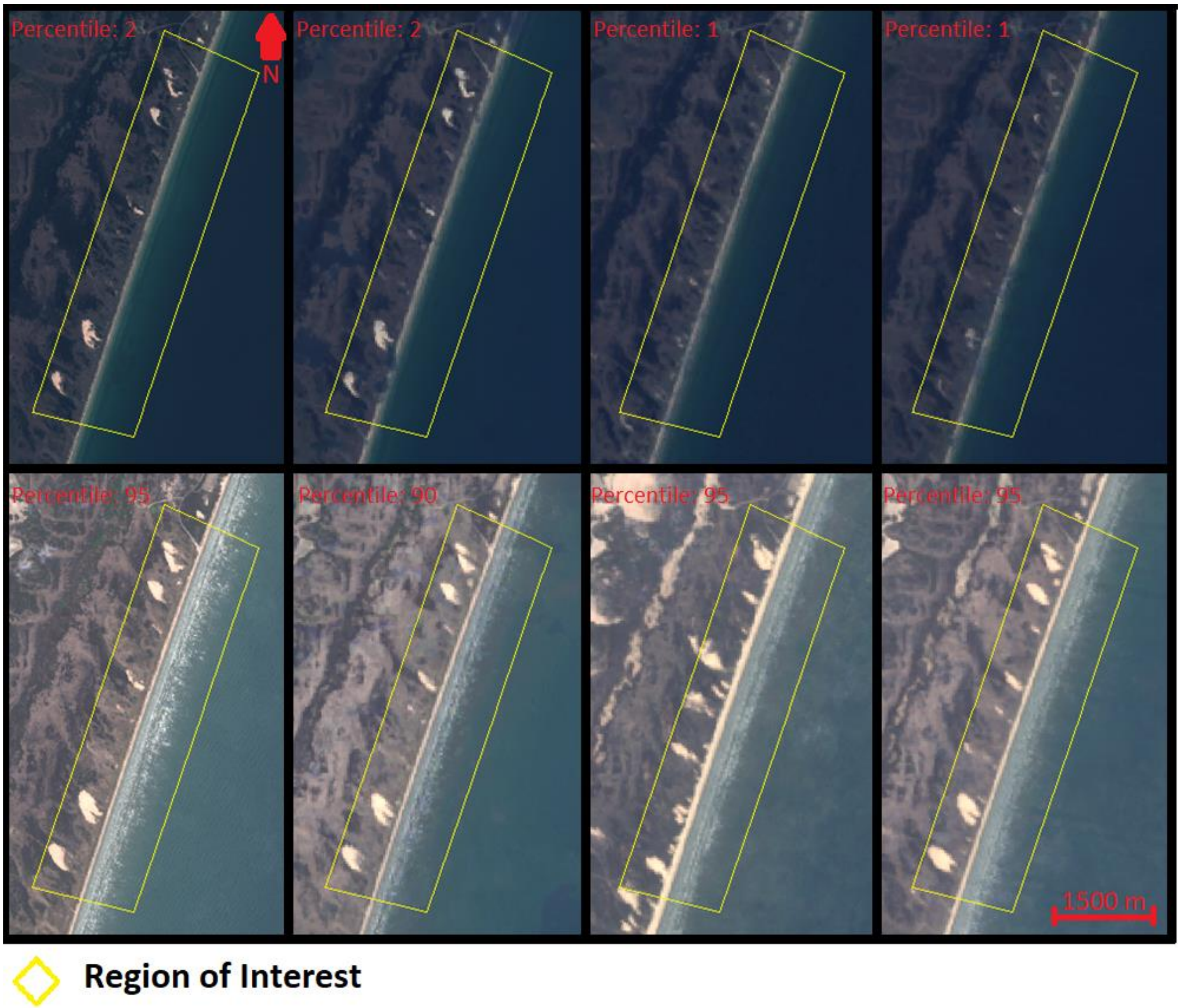

Figure A-2; Percentile images used for the smallest (upper figures) and highest (lowest figures) acceptable percentile values for the Padre Island study site. From left to right: Sentinel-2, Landsat 8, Landsat 4, 5 and 7 before 2003 and Landsat 5 and 7 after 2003. Percentile values used are presented in the top left corner.

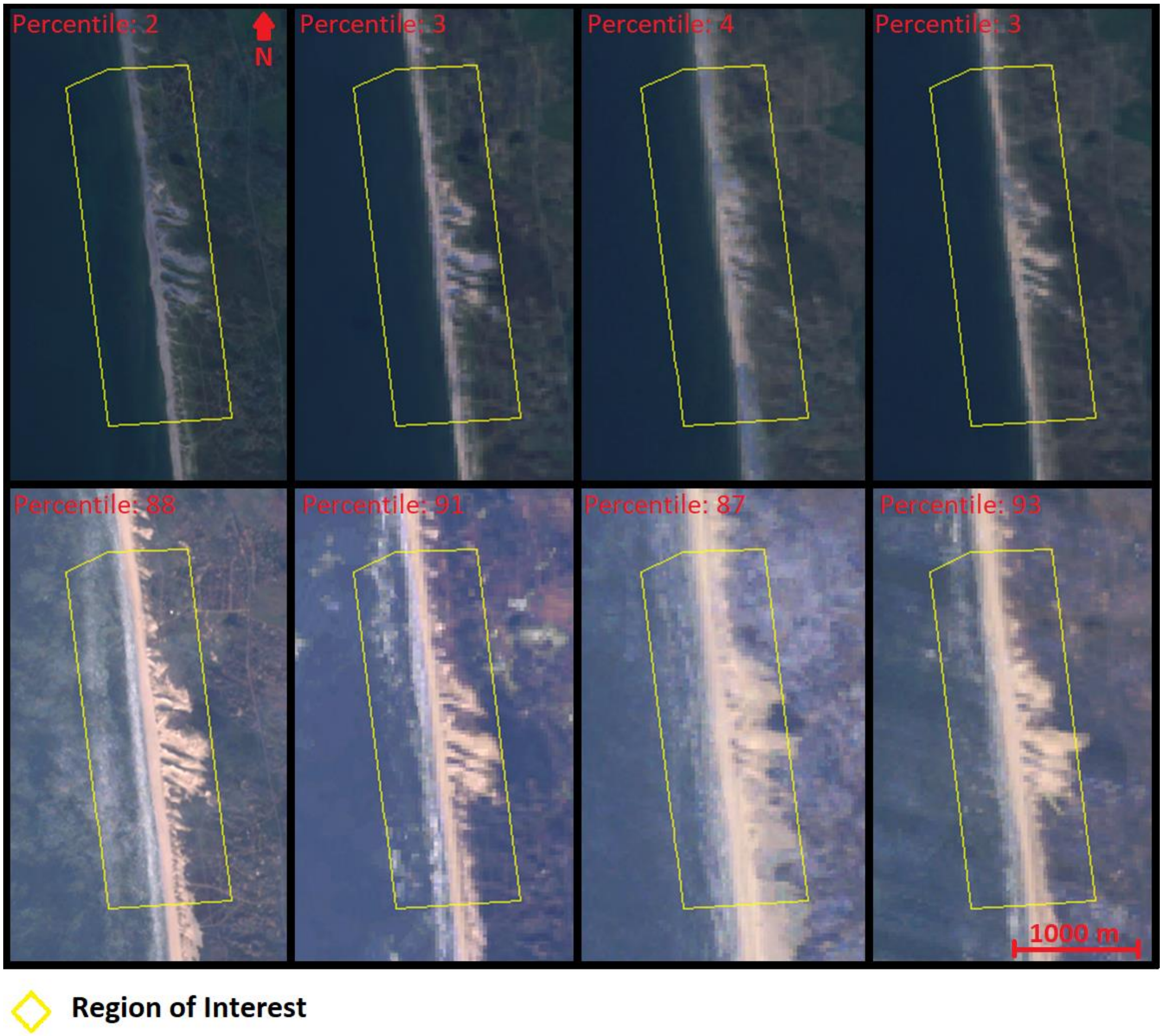

Figure A-3; Percentile images used for the smallest (upper figures) and highest (lowest figures) acceptable percentile values for the Haurvig study site. From left to right: Sentinel-2, Landsat 8, Landsat 4, 5 and 7 before 2003 and Landsat 5 and 7 after 2003. Percentile values used are presented in the top left corner.

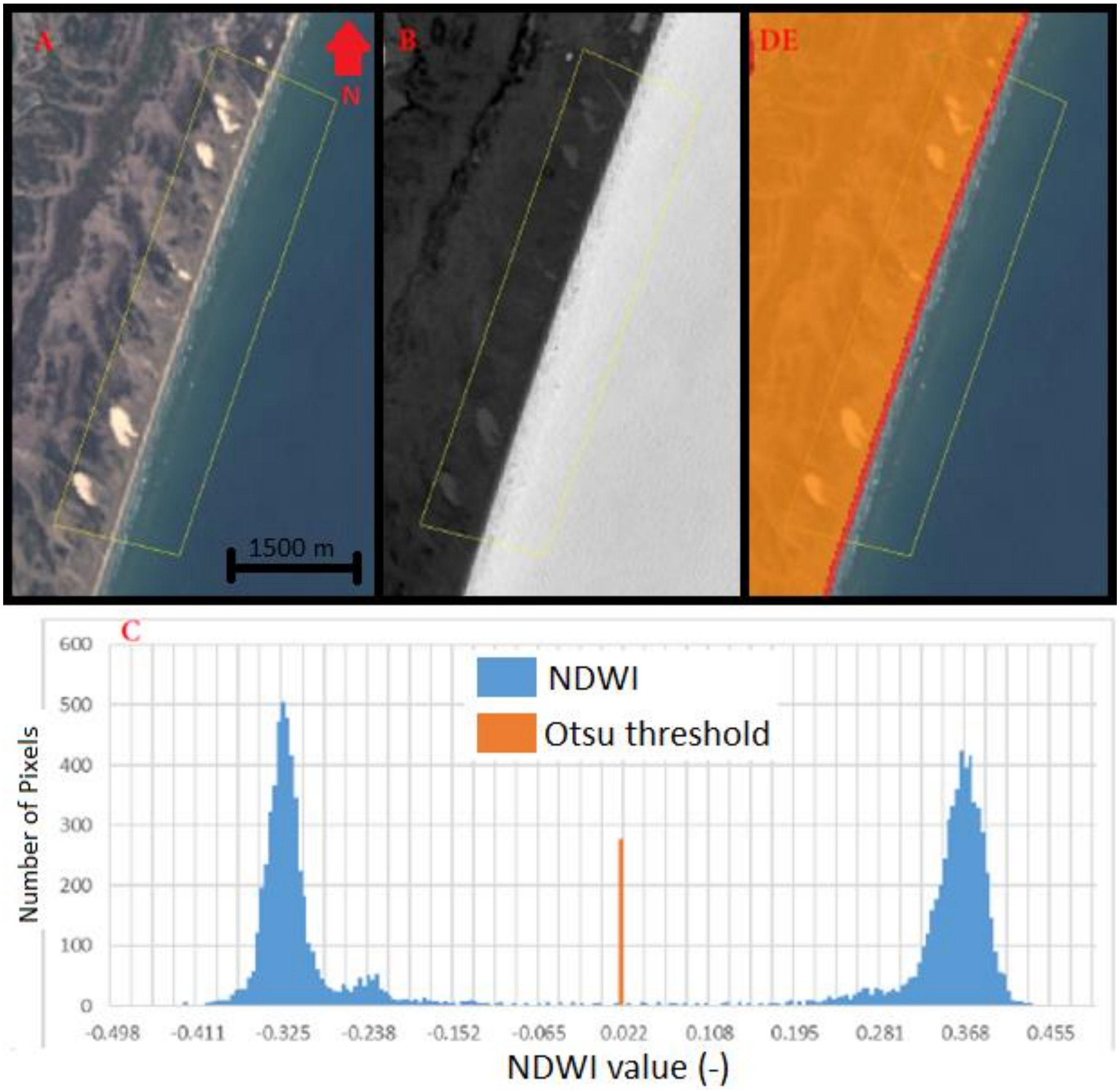

Figure A-4; A) Landsat-8 image at June 3 2018 in true colour, B) the calculated NDWI according to equation 1, C) a frequency distribution of the NDWI values and the corresponding Otsu threshold (0.017), DE) water mask based on the Otsu threshold (red) final water mask using the morphological dilation and erosion (orange). The ROI is indicated by the thin yellow line.

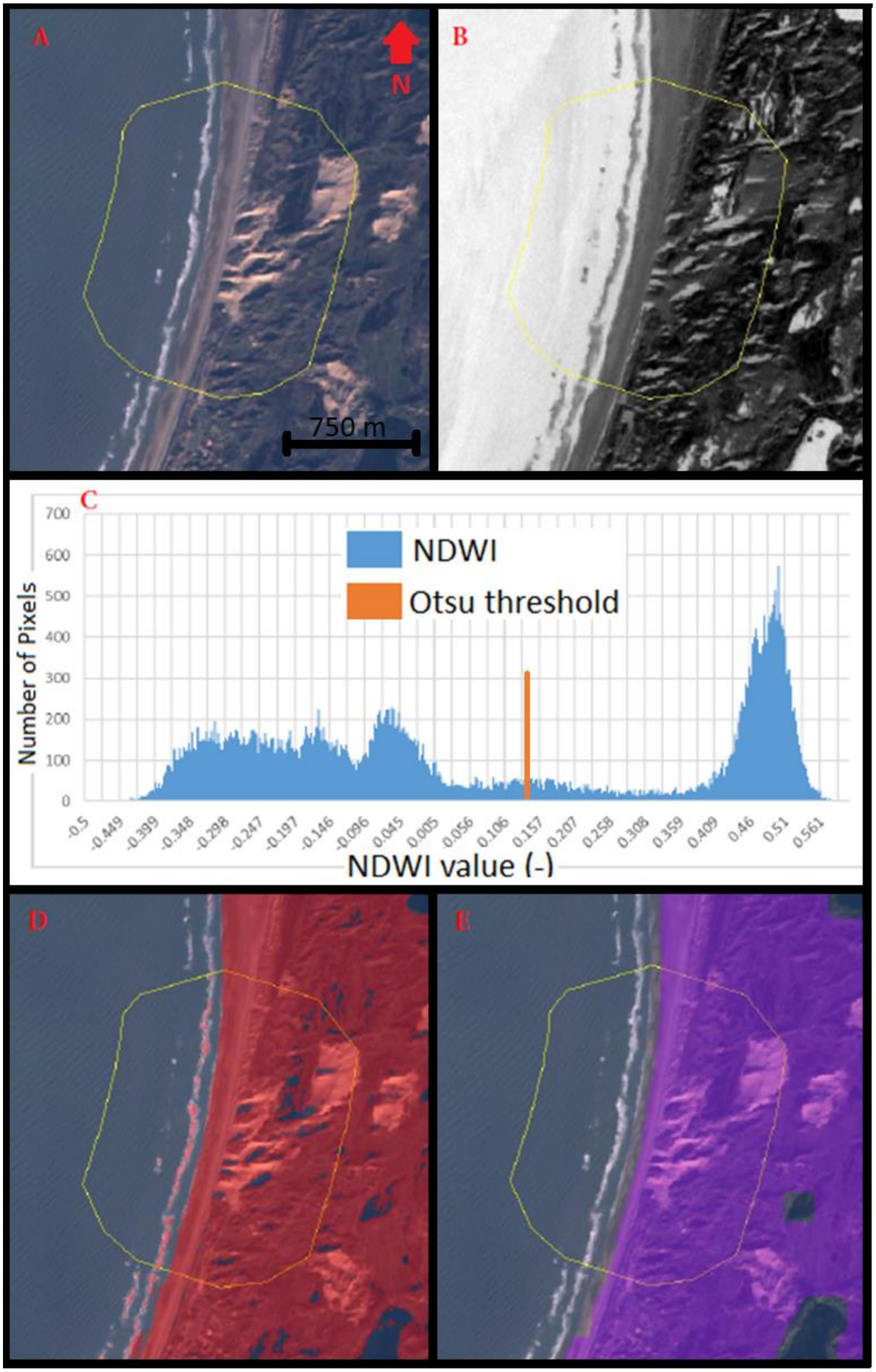

Figure A-5; A) Sentinel-2B image at 21 January 2019 in true colour, B) the calculated NDWI according to equation 1, C) a frequency distribution of the NDWI values and the corresponding Otsu threshold (-0.153), D) water mask based on the Otsu threshold and E) final water mask using the morphological dilation and erosion. The ROI is indicated by the thin yellow line.

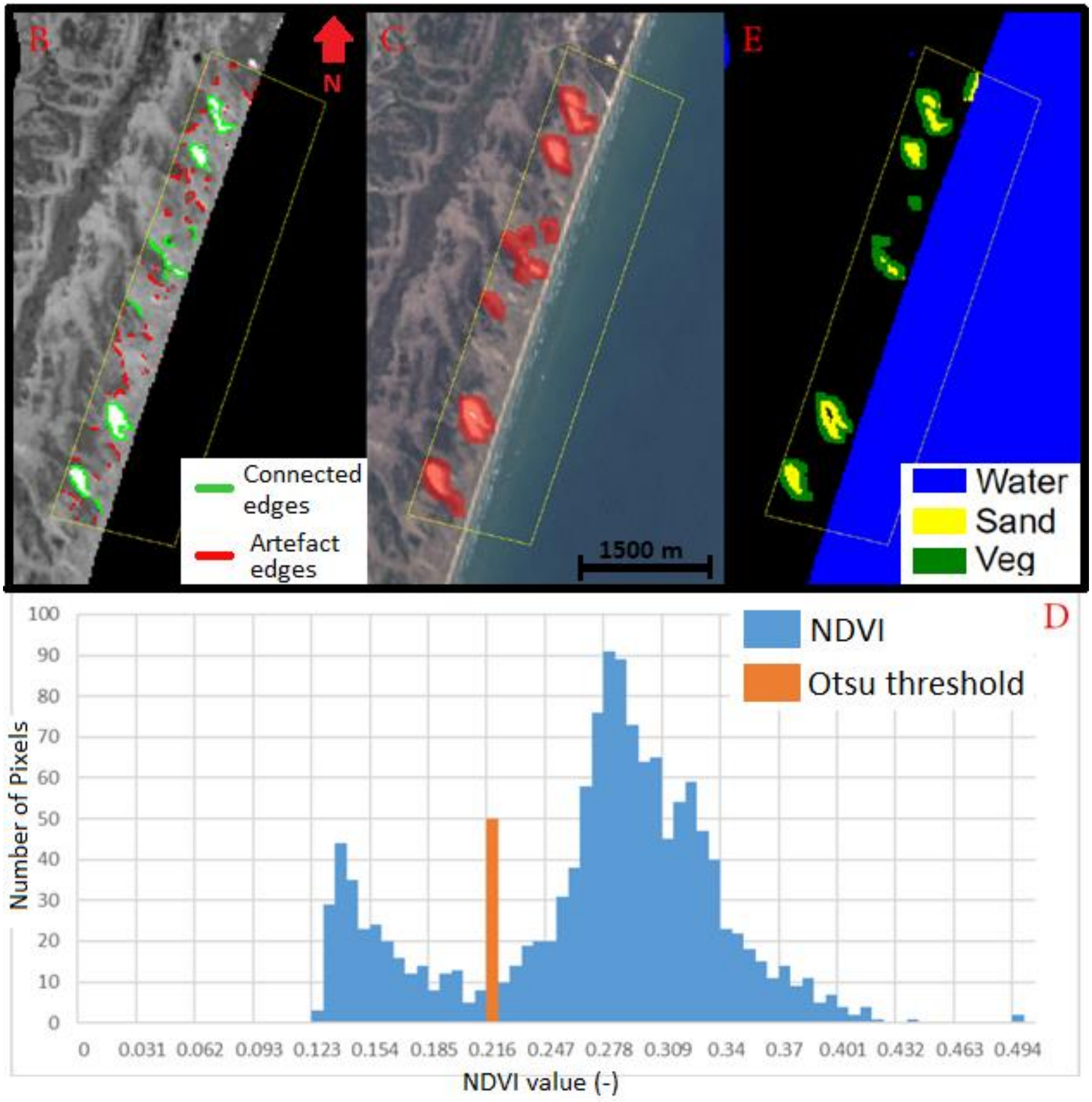

Figure A-6; B) Landsat-8 image at June 3 2018 in grey-scale SWIR2 image with connected Canny edges (>10 pixels) and artefact edges (<10 pixels), C) true colour image with morphological dilation of 60 m around the connected segments of edges in shaded red, D) histogram of NDVI values with the Otsu threshold (0.216), E) preliminary binary map based on the NDVI and NDWI Otsu threshold. The ROI is indicated by the thin yellow line. Note that the order of the letters of the sub-figures correspond to Figure 4-14 for consistency.

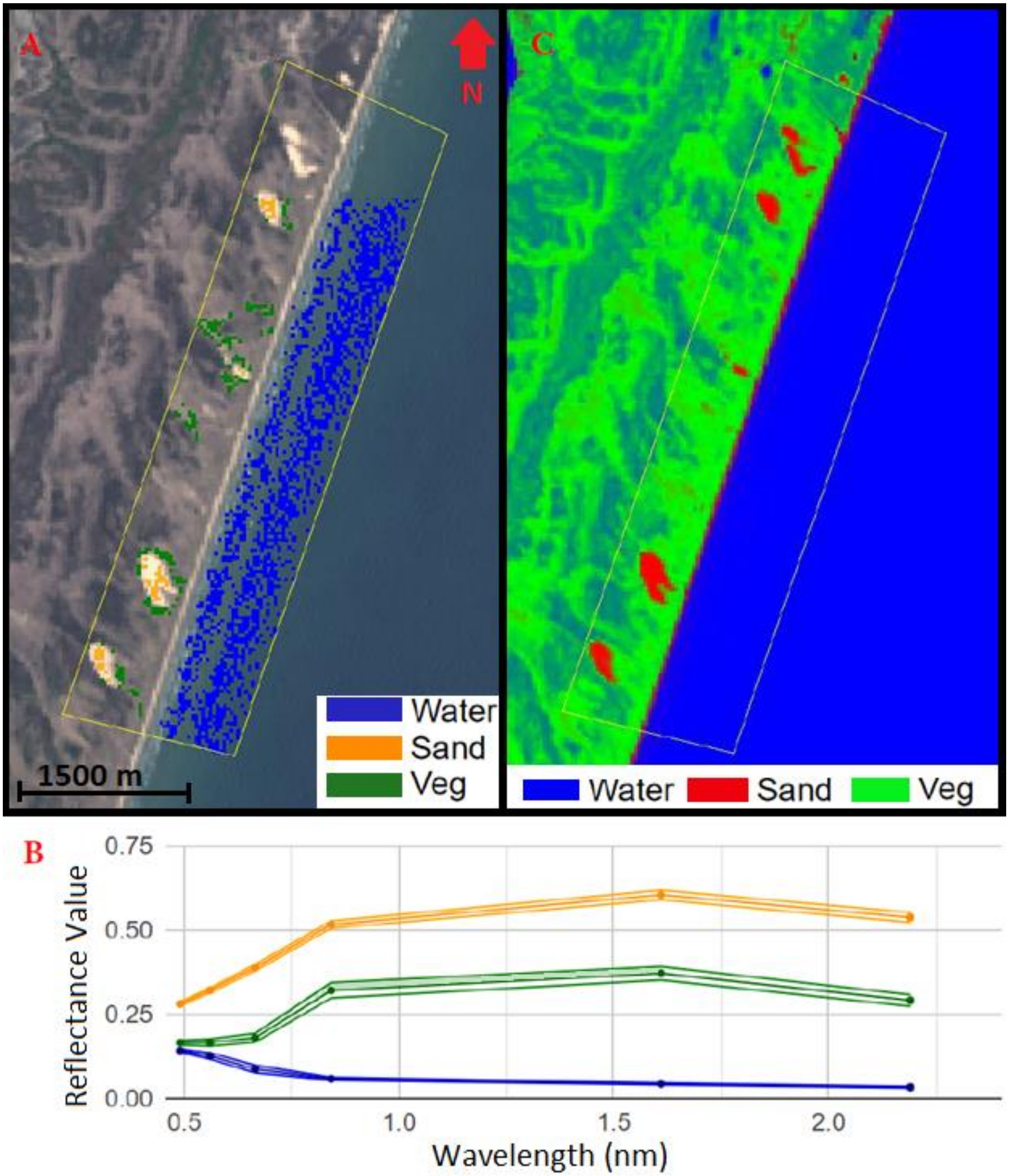

Figure A-7; Landsat-8 image at June 3 2018 for A) in true colour with on the foreground the selected pixels for the image endmembers (IE), B) the spectral response function for each land cover feature, with the central line representing the mean value and the lower and upper line one standard deviation, and C) the fractional abundance map of sand, water and vegetation. Legend in A corresponds to the colours in B.

Figure A-8; Sentinle-2 images of A) Haurvig (2015-09-11) and B) Zuid-Kennemerland (2015-08-05) in true colour. The yellow line represents the ROI for each study site. No edges were detected in image A, while only suppressed, short segments of connected edges were detected in image B (red pixels).

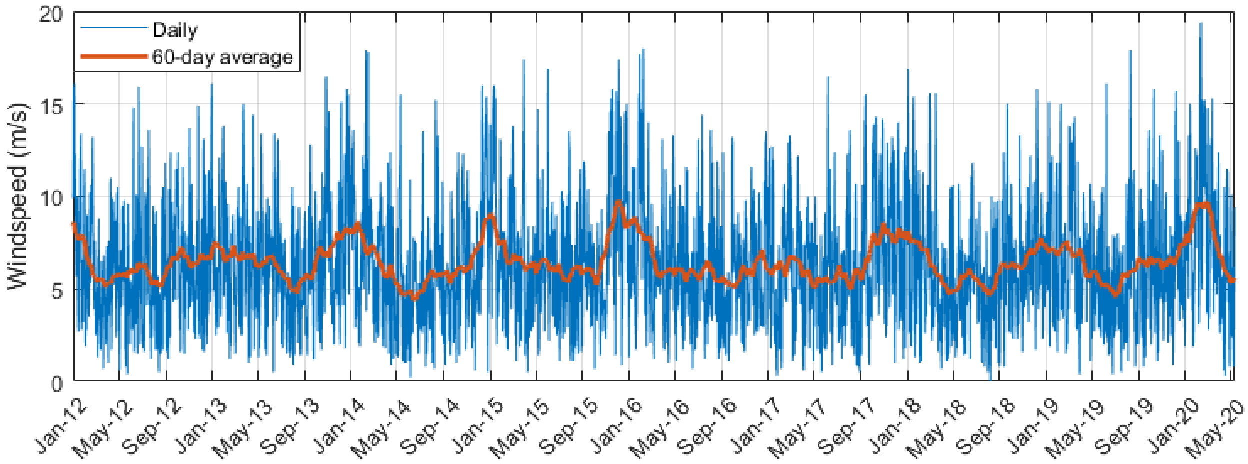

Figure A-9; Daily and 2 monthly averaged wind speed measured at the IJmuiden wind station. Data from the KNMI.

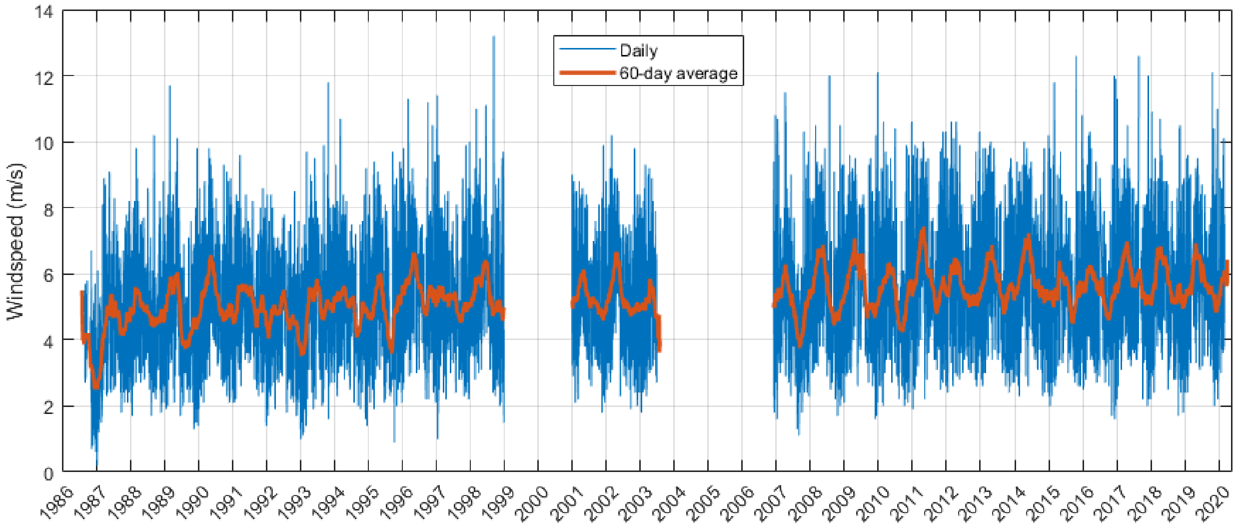

Figure A-10; average daily wind speed measured at the Corpus Cristi N.A.S. airport, about 30km north of the study area. Major data gaps were present between 1999 to 2000 and 2003 to 2007.

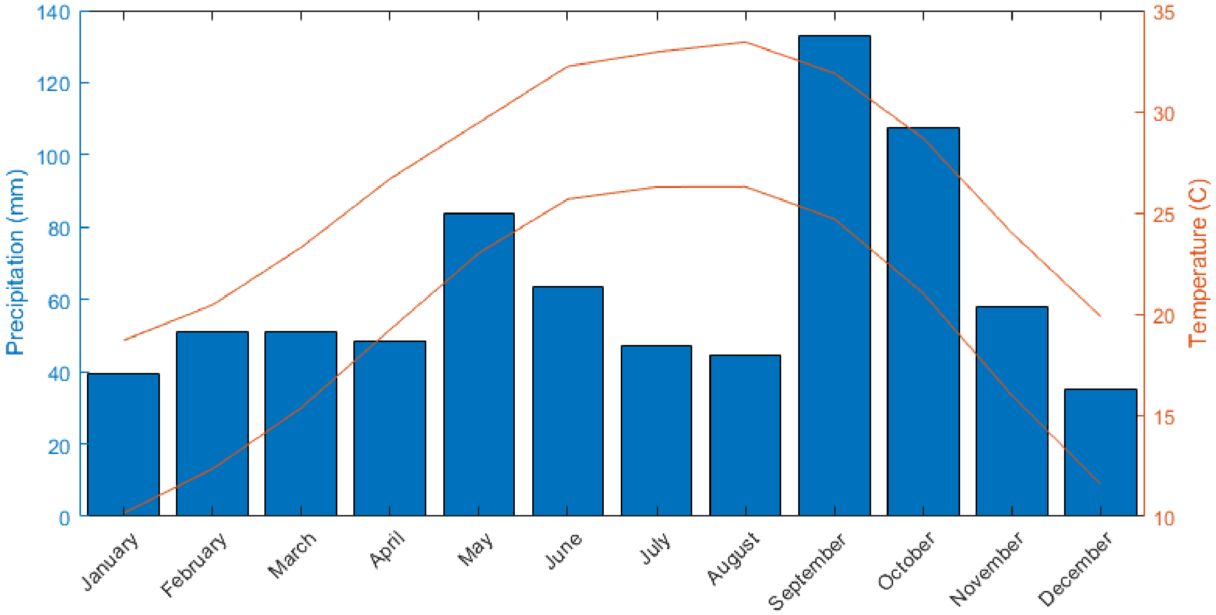

Figure A-11; Monthly summed precipitation and monthly mean minimum and maximum temperature at the Corpus Cristi weather station, data from 1980 till 2020 with a major time gap in the years 1999, 2000 and 2006. Relatively high rainfall averages for May depict rainfall events which occur over a few days (Kocurek et al., 1992). See for the timeseries Figure A-12.

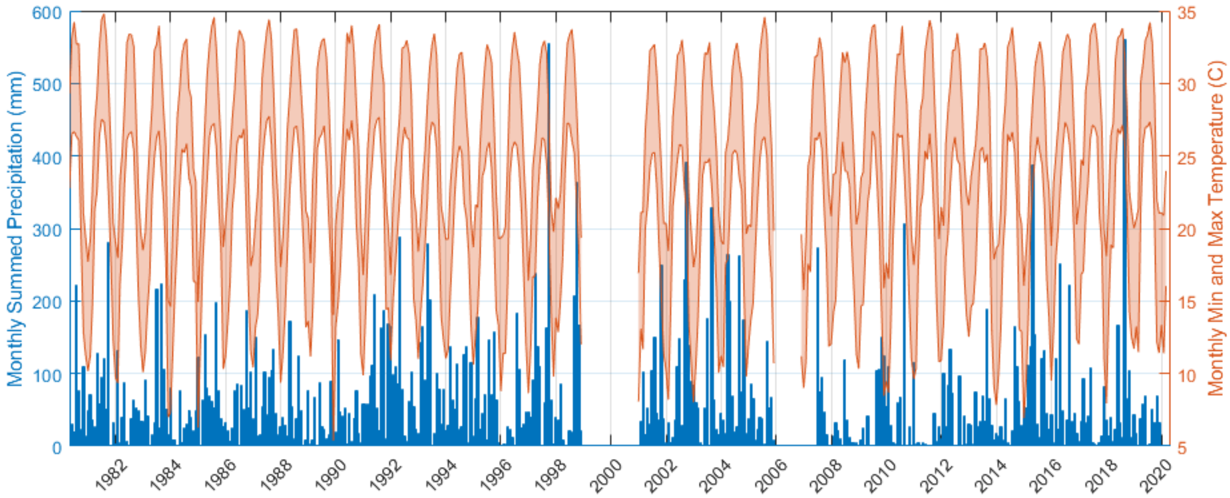

Figure A-12; Summed monthly precipitation and monthly averaged minimum and maximum temperature for Padre Island. Measured at the Corpus Christi N.A.S. airport, about 30km north of the study area. Data from 1980 till 2020 with a major time gap in the years 1999, 2000 and 2006.

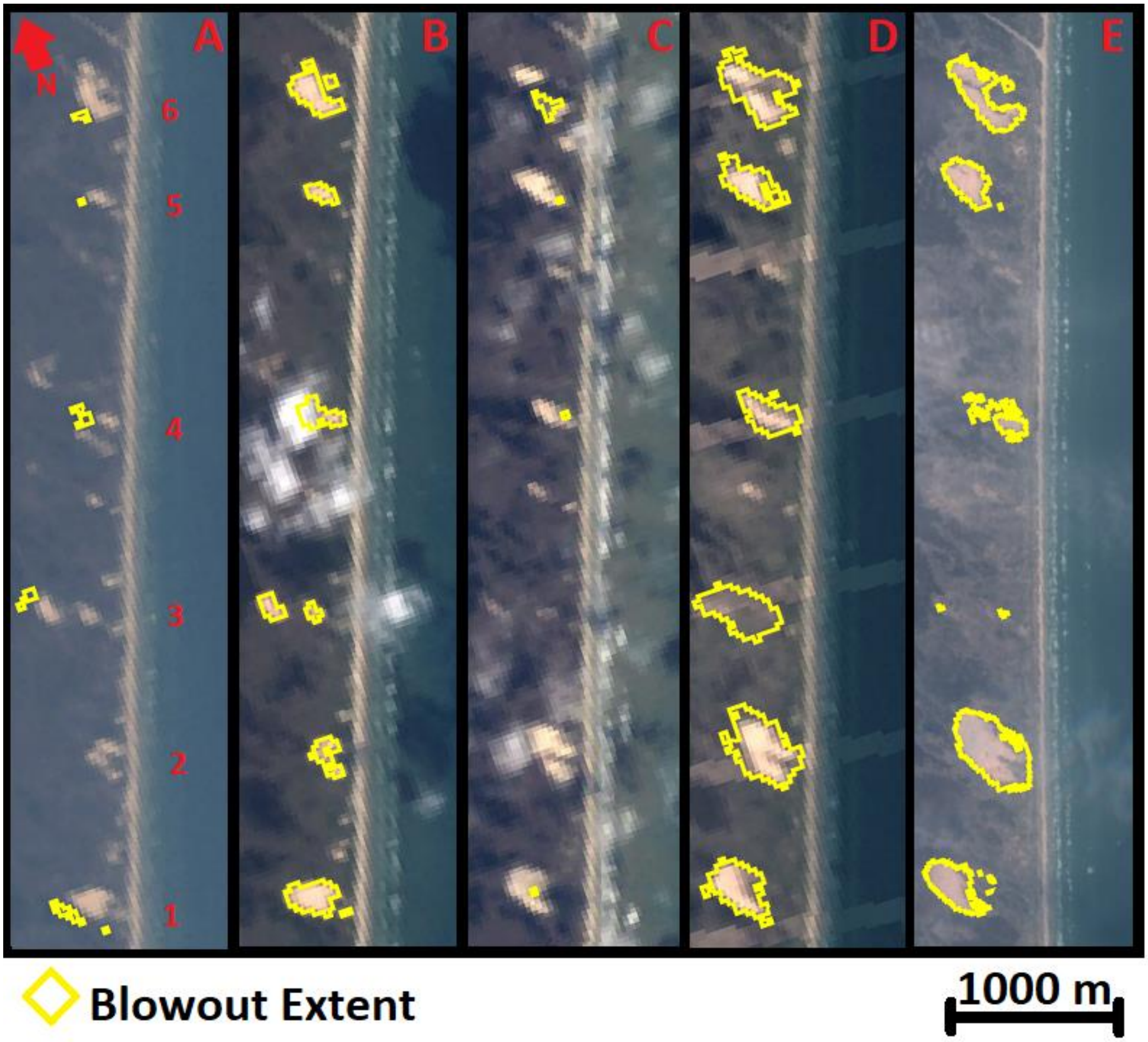

Figure A-13; Five major types of incorrectly estimated Blowout Extents at Padre Island:

- *A) Landsat-5 scene on 11 May 1998: underestimation due to poorly illuminated scene causing endmembers to be detected incorrectly;*
- *B) Landsat-7 scene on 27 September 1999: overestimation of a single blowout (4) by partial cloud cover;*
- *C) Landsat-5 scene on 5 February 2010: underestimation due to incorrect found endmembers caused by cloud cover;*
- *D) Landsat-7 scene on 3 October 2013: overestimation by incorrect estimated endmembers due to the difference vegetation reflectance in the Landsat-7 scene used for filling the Scan-Line-Corrector;*
- *E) Sentinel-2B scene on 17 March 2017: overestimation due to haze in the scene, causing a less clear difference in reflectance of vegetation and sand.*

B. Google Earth Engine links

Note: Links require a registered Google account:

https://developers.google.com/earth-engine/getstarted

B-1

https://code.earthengine.google.com/5d3fc61f97574103e4fcb49b3e3f6042

B-2

https://code.earthengine.google.com/b9090701cc1e06ea52b390441495be6e

B-3

https://code.earthengine.google.com/15582a52be67720de002407a48dc1498

B-4

https://code.earthengine.google.com/01ac5ad72470380e0a2d299a175c7f55

B-5

https://code.earthengine.google.com/fa806f3ffe4aabcd0644308f318dcd5f

B-6

https://code.earthengine.google.com/208f41c72bd0025891096caf01200074

B-7

https://code.earthengine.google.com/b70e18fdd691e5fe7e71fced281c37b9

B-8

https://code.earthengine.google.com/621f0ae172bb2a34010af6d6b78ea082

B-9

https://code.earthengine.google.com/389d36445f1d68877f396161ebfea88f

B-10

https://code.earthengine.google.com/6750a765b4b5d0978daea19e9a2c84a5

B-11

https://code.earthengine.google.com/e5b57594eb6813175547b25c5b28aa11

C. Number of buckets and strength of smoothing

The histogram of the water index (NDWI) and the vegetation index (NDVI) were used to obtain 1) an Otsu threshold and 2) a local maximum of the index-values. This appendix explains first how the histogram bucket width is determined for both processes. From these histograms, smoothed histograms using the Savitzky-Golay (S-G) smoothing (Savitzky and Golay, 1964) are constructed to obtain a local maximum of the index value. Therefore, the second part of this sections explains how the strength of the S-G smoothing is determined.

Determine histogram bucket widths

The standard reduction of a region of an image to a histogram inside the Google Earth Engine (GEE) occurred without proper explanation of the shape of the constructed histogram. Furthermore, the standard shape of the histograms was found to be unsatisfactory for especially low number of input pixels using the standard GEE applications. On the other hand, the number of input pixels varied enormously due to 1) the difference in resolution of the Sentinel-2 and Landsat satellites, and 2) the differences in the region to construct a histogram from due to differences in the Region of Interest (ROI) and number and length of Canny edges detected hindered the use of a constant bucket width for the histograms. Moreover, the range of valid input values from the index band used was variable both spatially (for the different ROIs) and temporally (due to e.g. seasonality in vegetation growth). Subsequently, this section in the appendix elaborates on the construction of the histogram bucket width for the frequency distributions used throughout this research.

To best reflect a dataset in a histogram, the number of buckets need to be adapted to the number of input values (further referred to as input pixels, as that is the data input). The number of buckets can then be scaled equally between the minimal and maximum value to obtain the bucket width. Subsequently, before constructing each histogram, first the number of valid input pixels was calculated. Pixels partly inside the ROI are always taken as 100% weight to overcome fractional presence of pixel within the histograms, meaning that unweighted reducers were used within this analysis. Then, the minimum and maximum index value (either NDVI or NWDI) within the region reduced to a histogram was calculated. These three values, the minimum and maximum input data value and the number of observations are generally used to calculate an appropriate number of buckets for a histogram (Lane et al., 2017). Using the minimum and maximum value, the number of buckets could be translated to the bucket width.

The choices for the number of buckets and bucket width of a histogram are difficult and it is important to note that there has not found any 'best' rule to determine the histogram shape (Lane et al., 2017). On the other hand, many attempts have been made to find a rule for the histogram shape based on the input data. The first to establish a guideline for the histogram shape was Sturge (1926), where the bucket width could be determined through

$$\hat{h} = \frac{[range\ of\ data]}{1 + \log_2 n} \tag{13}$$

where *n* is the number of inputs (Sturges, 1926; Wand, 1997). However, the Sturge' rule has been showed to oversmooth histograms for large number of input data (Scott, 2012). Therefore, other attempts have been made, such as the Rice rule (Lane et al., 2017) defined as

$$\hat{h} = \frac{[range\ of\ data]}{2 \times \sqrt[3]{n}} \tag{14}$$

where similar as in many other attempts the number of buckets is basically determined by $n^{-1/3}$, which has shown to provide almost always a good number of buckets for each situation, although strongly reduces the number of buckets for large input datasets (Wand, 1997). When the number of buckets is relatively low, the histogram may be oversmoothed, removing local maxima. Consequently, to retain sufficient local maxima in the histogram for large number of inputs, the histogram bin width is calculated as

$$\hat{h} = \frac{[range\ of\ data]}{2 \times \sqrt{n}} \tag{15}$$

where the *range of data* in the images mean the lowest and highest index value present (NDWI or NDVI). Multiplying by two made sure there were also sufficient buckets for a relative low number of inputs, such as is done in Rice Rule (Lane et al., 2017), while determining the number of buckets from $n^{-1/2}$ made sure the histogram was not oversmoothed with large input datasets.

Determine strength of the Savitzky-Golay smoothing

The Savitzky-Golay (S-G) smoothing (Savitzky and Golay, 1964) was used throughout this analysis. The S-G smoothing is ideal to reduce noise while maintaining the shape and height of the actual data series (Schafer, 2011). S-G smoothing itself requires the user input of 1) the order of the polynomial fit, and 2) window size (Orfanidis, 1995). The order of the polynomial fit of the S-G smoothing of the histograms was always applied with a linear (first order polynomial) fit, as higher polynomial fits could result in negative values (Orfanidis, 1995), which were impossible in frequency distributions. The window size was the number of points to be used in the estimate of the current data point, which was always an uneven number so an equal number of data points was taken into the calculation of the smoothed data series on either side of the actual data point. In this research, the window size was the number of surrounding buckets to include for the calculation of the smoothened bucket value. Consequently, stronger averaging of the original dataset could be obtained through increasing the window size. However, the previous section of this appendix described the determination of the size of the buckets, which was flexible based on the number of inputs. As the input values were similar throughout the dataset, namely the NDVI and NDWI having a maximum range of [-1, 1], the window size could be linked to a constant range within the index values. Thus, the window size of the S-G smoothing could be chosen such each window was linked to a constant range of the index band. Empirically, it was found that the S-G smoothing did return an adequate averaging of the dataset when the S-G smoothing was applied with a window size operating on a range of approximately 0.02 for both indices, the NDWI and the NDVI. Subsequently, the size of the window was calculated as

$$w = \left\lceil \frac{0.02/_{\hat{h}}}{2} \right\rceil \times 2 - 1 \tag{16}$$

where $\hat{h}$ was the calculated bucket width according to equation (13). Note that if w was lower than 3, w was set at 3, as that is the lowest window size possible in any moving average filter such as the S-G smoothing.

On the other hand, averaging of the original data might also be obtained through multiple sequences of smoothing of the original data. In this sequential process, the first iteration refers to S-G smoothing of the original dataset, while the second iteration refers to the S-G smoothing of the dataset obtained with the first iteration. Subsequently, multiple iterations of S-G smoothing allow for increased averaging of the original dataset with a relative low window size, such that the removal of local maxima is diminished (Chen et al., 2004). Thus, throughout this research, the relative strength of averaging the original data was defined as number of iterations the S-G smoothing was applied.

Consequently, the strength of the smoothing was adapted to the actual number of inputs, as the lower the number of input values, strong smoothing removed the variation within the dataset. In that case, strong smoothing would shift or even eliminate the local maxima. Contrary, weak smoothing of a large number of inputs does not remove high-frequency, which could result in the detection of high-frequency noise instead of the detection of actual local peaks in the dataset. Therefore, the strength of the smoothing was made dependent on the number of input pixels. Although there iss done a lot of analysis on what the statistical optimum is for the strength of the S-G smoothing (Orfanidis, 1995; Chen et al., 2004; Menon and Seelamantula, 2014), it is always based on 1) the local variance within the dataset and, 2) the size of the dataset. As the methodology was aimed at obtaining a near-bimodal deviation of the dataset before constructing a frequency distribution (see section 4.4.1), the local variance within the dataset was assumed to be near equal throughout the datasets, thus can be neglected for determining the strength of the S-G smoothing. Subsequently, the strength of smoothing was only adaptive to the size of the dataset, which in this research was referred to as the number of input pixels. To the best authors' knowledge, no satisfactory information could be found for determining the number of iterations for averaging the dataset with a first order polynomial fit using iterative S-G smoothing. However, as discussed previously, major aim of the strength of smoothing was that it is increased with an increasing size of the dataset. Subsequently, a best fit for the number of iterations was defined as

$$i = \left\lceil \sqrt{\frac{n}{500}} \right\rceil \tag{16}$$

where n was the size of the dataset (i.e. the number of pixels within the geometry considered for the frequency histogram).